Technical Proposal
for

Antiproton—Proton Scattering Experiments with Polarization

($\mathcal{PAX}$ Collaboration)

Jülich, January 15, 2005

Technical Proposal
for

Antiproton–Proton Scattering Experiments with Polarization

($\mathcal{PAX}$ Collaboration)

Abstract

Polarized antiprotons, produced by spin filtering with an internal polarized gas target, provide access to a wealth of single– and double–spin observables, thereby opening a new window to physics uniquely accessible at the HESR. This includes a first measurement of the transversity distribution of the valence quarks in the proton, a test of the predicted opposite sign of the Sivers–function, related to the quark distribution inside a transversely polarized nucleon, in Drell–Yan (DY) as compared to semi–inclusive DIS, and a first measurement of the moduli and the relative phase of the time–like electric and magnetic form factors $G_{E,M}$ of the proton. In polarized and unpolarized $p\bar{p}$ elastic scattering, open questions like the contribution from the odd charge–symmetry Landshoff–mechanism at large $|t|$ and spin–effects in the extraction of the forward scattering amplitude at low $|t|$ can be addressed. The proposed detector consists of a large–angle apparatus optimized for the detection of DY electron pairs and a forward dipole spectrometer with excellent particle identification.

The design and performance of the new components, required for the polarized antiproton program, are outlined. A low–energy Antiproton Polarizer Ring (APR) yields an antiproton beam polarization of $P_{\bar{p}} = 0.3$ to 0.4 after about two beam life times, which is of the order of 5–10 h. By using an internal $H^{\uparrow}$ target and a detector installed in a 3.5 GeV/c Cooler Synchrotron Ring (CSR), the Phase–I experimental $\bar{p}^{\uparrow}p^{\uparrow}$ program could start in 2014, completely independent of the operation of the HESR. In Phase–II, the CSR serves as an injector for the polarized antiprotons into the HESR. A chicane system inside the HESR is proposed to guide the high–energy $\bar{p}^{\uparrow}$ beam to the PAX detector, located inside the CSR straight section. In Phase–II, fixed–target or collider $\bar{p}^{\uparrow}p^{\uparrow}$ experiments over a broad energy range become possible. In the collider mode, polarized protons stored in the CSR up to momenta of 3.5 GeV/c are bombarded head–on with 15 GeV/c polarized antiprotons stored in the HESR. This asymmetric double–polarized antiproton–proton collider is ideally suited to map e.g. the transversity distribution in the proton.

Members of the Collaboration

Alessandria, Italy, Universita′ del Piemonte Orientale ″A. Avogadro″ and INFN

Vincenzo Barone

Beijing, China, School of Physics, Peking University

Bo–Qiang Ma

Bochum, Germany, Institut für Theoretische Physik II, Ruhr Universität Bochum

Klaus Goeke, Andreas Metz, and Peter Schweitzer

Bonn, Germany, Helmholtz–Institut für Strahlen– und Kernphysik, Universität Bonn

Jens Bisplinghoff, Paul–Dieter Eversheim, Frank Hinterberger, and Heiko Rohdjeß

Brookhaven, USA, Collider–Accelerator Department, Brookhaven National Laboratory

Christoph Montag

Brookhaven, USA, RIKEN BNL Research Center, Brookhaven National Laboratory

Werner Vogelsang

Cagliari, Italy, Dipartimento di Fisica, Universita′ di Cagliari and INFN

Umberto D′Alesio and Francesco Murgia

Dublin, Ireland, Department of Mathematics, University of Dublin

Nigel Buttimore

Dubna, Russia, Bogoliubov Laboratory of Theoretical Physics, Joint Institute for Nuclear Research

Anatoly Efremov and Oleg Teryaev

Dubna, Russia, Dzhelepov Laboratory of Nuclear Problems, Joint Institute for Nuclear Research

Sergey Dymov, Natela Kadagidze, Vladimir Komarov, Anatoly Kulikov, Vladimir Kurbatov, Vladimir Leontiev, Gogi Macharashvili, Sergey Merzliakov, Valeri Serdjuk, Sergey Trusov, Yuri Uzikov, Alexander Volkov, and Nikolai Zhuravlev

Dubna, Russia, Laboratory of Particle Physics, Joint Institute for Nuclear Research

Oleg Ivanov, Victor Krivokhizhin, Gleb Meshcheryakov, Alexander Nagaytsev, Vladimir Peshekhonov, Igor Savin, Binur Shaikhatdenov, Oleg Shevchenko, and Gennady Yarygin

Erlangen, Germany, Physikalisches Institut, Universität Erlangen–Nürnberg

Wolfgang Eyrich, Andro Kacharava, Bernhard Krauss, Albert Lehmann, Davide Reggiani, Klaus Rith, Ralf Seidel, Erhard Steffens, Friedrich Stinzing, Phil Tait, and Sergey Yaschenko

Ferrara, Italy, Istituto Nazionale di Fisica Nucleare

Marco Capiluppi, Guiseppe Ciullo, Marco Contalbrigo, Alessandro Drago, Paola Ferretti–Dalpiaz, Paolo Lenisa, Luciano Pappalardo, Giulio Stancari, Michelle Stancari, and Marco Statera

Frascati, Italy, Istituto Nazionale di Fisica Nucleare

Eduard Avetisyan, Nicola Bianchi, Enzo De Sanctis, Pasquale Di Nezza, Alessandra Fantoni, Cynthia Hadjidakis, Delia Hasch, Marco Mirazita, Valeria Muccifora, Federico Ronchetti, and Patrizia Rossi

Gatchina, Russia, Petersburg Nuclear Physics Institute

Sergey Barsov, Stanislav Belostotski, Oleg Grebenyuk, Kirill Grigoriev, Anton Izotov, Anton Jgoun, Peter Kravtsov, Sergey Manaenkov, Maxim Mikirtytchiants, Sergey Mikirtytchiants, Oleg Miklukho, Yuri Naryshkin, Alexander Vassiliev, and Andrey Zhdanov

Gent, Belgium, Department of Subatomic and Radiation Physics, University of Gent

Dirk Ryckbosch

Hefei, China, Department of Modern Physics, University of Science and Technology of China

Yi Jiang, Hai–jiang Lu, Wen–gan Ma, Ji Shen, Yun–xiu Ye, Ze–Jie Yin, and Yong–min Zhang

Jülich, Germany, Forschungszentrum Jülich, Institut für Kernphysik

David Chiladze, Ralf Gebel, Ralf Engels, Olaf Felden, Johann Haidenbauer, Christoph Hanhart, Michael Hartmann, Irakli Keshelashvili, Siegfried Krewald, Andreas Lehrach, Bernd Lorentz, Sigfried Martin, Ulf–G. Meißner, Nikolai Nikolaev, Dieter Prasuhn, Frank Rathmann, Ralf Schleihert, Hellmut Seyfarth, Alexander Sibirtsev, and Hans Ströher

Kosice, Slovakia, Institute of Experimental Physics, Slovak Academy of Sciences and P.J. Safarik University, Faculty of Science

Dusan Bruncko, Jozef Ferencei, Ján Mušinský, and Jozef Urbán

Langenbernsdorf, Germany, Unternehmensberatung und Service–Büro (USB), Gerlinde Schulteis & Partner GbR

Christian Wiedner (formerly at MPI-K Heidelberg)

Lecce, Italy, Dipartimento di Fisica, Universita′ di Lecce and INFN

Claudio Corianó and Marco Guzzi

Madison, USA, University of Wisconsin

Tom Wise

Moscow, Russia, Institute for Theoretical and Experimental Physics

Vadim Baru, Ashot Gasparyan, Vera Grishina, Leonid Kondratyuk, and Alexander Kudriavtsev

Moscow, Russia, Lebedev Physical Institute

Alexander Bagulya, Evgeni Devitsin, Valentin Kozlov, Adel Terkulov, and Mikhail Zavertiaev

Moscow, Russia, Physics Department, Moscow Engineering Physics Institute

Aleksei Bogdanov , Sandibek Nurushev, Vitalii Okorokov, Mikhail Runtzo, and Mikhail Strikhanov

Novosibirsk, Russia, Budker Institute for Nuclear Physics

Yuri Shatunov

Palaiseau, France, Centre de Physique Theorique, Ecole Polytechnique

Bernard Pire

Protvino, Russia, Institute of High Energy Physics

Nikolai Belikov, Boris Chujko, Yuri Kharlov, Vladislav Korotkov, Viktor Medvedev, Anatoli Mysnik, Aleksey Prudkoglyad, Pavel Semenov, Sergey Troshin, and Mikhail Ukhanov

Tbilisi, Georgia, Institute of High Energy Physics and Informatization, Tbilisi State University

Badri Chiladze, Nodar Lomidze, Alexander Machavariani, Mikheil Nioradze, Tariel Sakhelashvili, Mirian Tabidze, and Igor Trekov

Tbilisi, Georgia, Nuclear Physics Department, Tbilisi State University

Leri Kurdadze and George Tsirekidze

Torino, Italy, Dipartimento di Fisica Teorica, Universita di Torino and INFN

Mauro Anselmino, Mariaelena Boglione, and Alexei Prokudin

Uppsala, Sweden, Department of Radiation Sciences, Nuclear Physics Division

Pia Thorngren–Engblom

Virginia, USA, Department of Physics, University of Virginia

Simonetta Liuti

Warsaw, Poland, Soltan Institute for Nuclear Studies

Lech Szymanowski

Yerevan, Armenia, Yerevan Physics Institute

Norayr Akopov, Robert Avagyan, Albert Avetisyan, Zaven Hakopov, Hrachia Marukyan, and Sargis Taroian

Spokespersons:

Paolo Lenisa, E–Mail: lenisa@mail.desy.de
Frank Rathmann, E–Mail: f.rathmann@fz–juelich.de

Contents

Part I
Physics Case

1 Preface

The polarized antiproton–proton interactions at HESR will allow a unique access to a number of new fundamental physics observables, which can be studied neither at other facilities nor at HESR without transverse polarization of protons and/or antiprotons:

- The transversity distribution is the last leading–twist missing piece of the QCD description of the partonic structure of the nucleon. It describes the quark transverse polarization inside a transversely polarized proton [1]. Unlike the more conventional unpolarized quark distribution $q(x, Q^2)$ and the helicity distribution $\Delta q(x, Q^2)$, the transversity $h_1^q(x, Q^2)$ can neither be accessed in deep–inelastic scattering of leptons off nucleons nor can be reconstructed from the knowledge of $q(x, Q^2)$ and $\Delta q(x, Q^2)$. It may contribute to some single–spin observables, but always coupled to other unknown functions. The transversity distribution is directly accessible uniquely via the **double transverse spin asymmetry** A_{TT} in the Drell–Yan production of lepton pairs. The theoretical expectations for A_{TT} in the Drell–Yan process with transversely polarized antiprotons interacting with a transversely polarized proton target or beam at HESR are in the 30–40 per cent range [2, 3]; with the expected antiproton spin–filtering rate and luminosity of HESR the PAX experiment is uniquely suited for the definitive observation of $h_1^q(x, Q^2)$ of the proton for the valence quarks.

- The PAX measurements can also provide completely new insights into the understanding of (transverse) single–spin asymmetries (SSA) which have been observed in proton–proton and proton–antiproton collisions as well as in lepton–nucleon scattering. For instance through charm production ($\bar{p}^{\uparrow}\, p \to D\, X$ or $\bar{p}\, p^{\uparrow} \to D\, X$) it will be possible to disentangle the Sivers [4] and the Collins mechanisms [5]. In general, both effects contribute to the measured SSA (mostly in $p^{\uparrow}\, p \to \pi\, X$ and $\bar{p}^{\uparrow}\, p \to \pi\, X$), but in the case of charm production the Collins mechanism drops out. Moreover, in conjunction with the data on SSA from the HERMES collaboration [6, 7], the PAX measurements of the SSA in Drell–Yan production on transversely polarized protons can for the first time provide a test of the theoretical prediction [8] of the sign–reversal of the Sivers function from semi–inclusive DIS to Drell–Yan processes. Both studies will crucially test and improve our present QCD–description of the intriguing phenomenon of SSA.

- The origin of the unexpected Q^2–dependence of the ratio of the magnetic and electric form factors of the proton, as observed at the Jefferson laboratory [9], can be clarified by a measurement of their relative phase in the time–like region, which discriminates

strongly between the models for the form factor. This phase can be measured via SSA in the annihilation $\bar{p}p^{\uparrow} \to e^+e^-$ on a transversely polarized target [10, 11]. The first ever measurement of this phase at PAX will also contribute to the understanding of the onset of the pQCD asymptotics in the time–like region and will serve as a stringent test of dispersion theory approaches to the relationship between the space–like and time–like form factors [12, 13, 14]. The double–spin asymmetry will fix the relative phase ambiguity and allow independently the $G_E - G_M$ separation, which will serve as a check of the Rosenbluth separation in the time–like region.

- Arguably, in $p\bar{p}$ elastic scattering the hard scattering mechanism can be checked beyond $|t| = \frac{1}{2}(s - 4m_p^2)$ accessible in the t–u–symmetric pp scattering, because in the $p\bar{p}$ case the u–channel exchange contribution can only originate from the strongly suppressed exotic dibaryon exchange. Consequently, in the $p\bar{p}$ case the hard mechanisms [15, 16, 17] can be tested at t almost twice as large as in pp scattering. Even unpolarized large angle $p\bar{p}$ scattering data can shed light on the origin of the intriguing oscillations around the s^{-10} behavior of the 90^0 scattering in the pp channel and put stringent constraints on the much disputed charge conjugation–odd independent-scattering Landshoff mechanism [18, 19, 20, 21]. In general, the interplay of different mechanisms is such that single and double transverse asymmetries in $p\bar{p}$ scattering are expected to be as large as the ones observed in the pp case.

- The charge conjugation property allows direct monitoring of the polarization of antiprotons in HESR and the rate of polarization buildup constitutes a direct measurement of the transverse double spin asymmetry in the $p\bar{p}$ total cross section. This asymmetry has never been measured and its knowledge is crucial for the correct extraction of the real part of the forward $p\bar{p}$ scattering amplitude from Coulomb–nuclear interference. The PAX results on the asymmetry will help to clarify the origin of the discrepancy between the dispersion theory calculations [22] and the experimental extraction [23] of the value of the real part of the forward scattering amplitude usually made assuming the spin independence of forward scattering.

2 Accessing Transversity Distributions

2.1 Spin Observables and Transversity

There are three leading–twist quantities necessary to achieve a full understanding of the nucleon quark structure: the unpolarized quark distribution $q(x, Q^2)$, the helicity distribution $\Delta q(x, Q^2)$ and the transversity distribution $\Delta_T q(x, Q^2)$ [more usually denoted as $h_1^q(x, Q^2)$] [1]. While Δq describes the quark longitudinal polarization inside a longitudinally polarized proton, the transversity describes the quark transverse polarization inside a transversely polarized proton at infinite momentum. h_1^q and Δq are two independent quantities, which might be equal only in the non–relativistic, small Q^2 limit. Moreover, the quark transverse polarization does not mix with the gluon polarization (gluons carry

only longitudinal spin), and thus the QCD evolutions of h_1^q and Δq are quite different. One cannot claim to understand the spin structure of the nucleon until all three leading–twist structure functions have been measured.

Whereas the unpolarized distributions are well known, and more and more information is becoming available on Δq, nothing is known experimentally on the nucleon transversity distribution. From the theoretical side, there exist only a few theoretical models for h_1^q. An upper bound on its magnitude has been derived: this bound holds in the naive parton model, and, if true in QCD at some scale, it is preserved by QCD evolution. Therefore, its verification or disproof would be by itself a very interesting result. The reason why h_1^q, despite its fundamental importance, has never been measured is that it is a chiral–odd function, and consequently it decouples from inclusive deep–inelastic scattering. Since electroweak and strong interactions conserve chirality, h_1^q cannot occur alone, but has to be coupled to a second chiral–odd quantity.

This is possible in polarized Drell–Yan processes, where one measures the product of two transversity distributions, and in semi–inclusive Deep Inelastic Scattering (SIDIS), where one couples h_1^q to a new unknown fragmentation function, the so–called Collins function [5]. Similarly, one could couple h_1^q and the Collins function in transverse single–spin asymmetries (SSA) in inclusive processes like $p^\uparrow\, p \to \pi\, X$.

Both HERMES [7] and COMPASS experiments are now gathering data on spin asymmetries in SIDIS processes, which should yield information on some combination of h_1^q and the Collins function. However, one cannot directly extract information on h_1^q alone: the measured spin asymmetries can originate also from the Sivers function [4] – a spin property of quark distributions, rather than fragmentation – which does not couple to transversity; in addition, higher twist effects might still be sizeable at the modest Q^2 of the two experiments, thus making the interpretation of data less clear. The transverse SSA experimentally observed in $p^\uparrow\, p \to \pi\, X$ and $\bar{p}^\uparrow\, p \to \pi\, X$ processes [24, 25, 26] can be interpreted in terms of transversity and Collins functions; however, also here contributions from the Sivers function are important, or even dominant [27], and these processes could hardly be used to extract information on h_1^q alone.

2.2 Transversity in Drell–Yan Processes at PAX

The most direct way to obtain information on transversity – the last leading–twist missing piece of the QCD nucleon spin structure – is the measurement of the double transverse spin asymmetry A_{TT} in Drell–Yan processes with *both transversely polarized beam and target*:

$$A_{TT} \equiv \frac{d\sigma^{\uparrow\uparrow} - d\sigma^{\uparrow\downarrow}}{d\sigma^{\uparrow\uparrow} + d\sigma^{\uparrow\downarrow}} = \hat{a}_{TT}\, \frac{\sum_q e_q^2\, h_1^q(x_1, M^2)\, h_1^{\bar{q}}(x_2, M^2)}{\sum_q e_q^2\, q(x_1, M^2)\, \bar{q}(x_2, M^2)}\,, \tag{1}$$

where $q = u, \bar{u}, d, \bar{d}, ...$, M is the invariant mass of the lepton pair and $\hat{a}_{TT}$ is the double spin asymmetry of the QED elementary process, $q\bar{q} \to \ell^+\ell^-$,

$$\hat{a}_{TT} = \frac{\sin^2\theta}{1 + \cos^2\theta}\, \cos 2\phi\,, \tag{2}$$

with θ the polar angle of the lepton in the l^+l^- rest frame and ϕ the azimuthal angle with respect to the proton polarization.

The measurement of A_{TT} is planned at RHIC, in Drell–Yan processes with transversely polarized protons (for a review see [28]). In this case one measures the product of two transversity distributions, one for a quark and one for an antiquark (both in a proton). At RHIC energies one expects measurements at $\tau = x_1 x_2 = M^2/s \simeq 10^{-3}$, which mainly lead to the exploration of the sea quark proton content, where polarization is likely to be tiny. Moreover, the QCD evolution of transversity is such that, in the kinematical regions of RHIC data, $h_1^q(x, Q^2)$ is much smaller than the corresponding values of $\Delta q(x, Q^2)$ and $q(x, Q^2)$. All this makes the double spin asymmetry A_{TT} expected at RHIC very small, of the order of a few percents or less [29, 30].

The situation with the PAX measurement of the double transverse spin asymmetry A_{TT} in Drell–Yan processes with *polarized antiprotons and protons*, $\bar{p}^\uparrow p^\uparrow \to \ell^+\ell^- X$, is entirely different. When combining the fixed target and the collider operational modes, the PAX experiment will explore ranges of $s \simeq$ 30–200 GeV^2 and $M^2 \simeq$ 4–100 GeV^2, which are ideal for the measurement of large values of A_{TT}. There are some unique features which strongly suggest to pursue the study of h_1^q in the $\bar{p}p$ channel with PAX:

- In $\bar{p}p$ processes both the quark (from the proton) and the antiquark (from the antiproton) contributions are large. For typical PAX kinematics in the fixed target mode ($s = 30$ or 45 GeV^2, see Sec. 13) one has $\tau = x_1 x_2 = M^2/s \simeq 0.2$ – 0.3, which means that only quarks and antiquarks with large x contribute, that is valence quarks for which h_1^q is expected to be large. Moreover, at such x and M^2 values the QCD evolution does not suppress $h_1^q(x, Q^2)$. $A_{TT}/\hat{a}_{TT}$ is expected to be as large as 30% [2]; this is confirmed by direct calculations using the available models for transversity distributions, some of which predict even larger values, up to 40–45% [3]. Actually, all these models agree in having $|h_1^u| \gg |h_1^d|$ [1], so that Eq. (1) for $\bar{p}p$ processes at PAX essentially becomes,

$$A_{TT} \simeq \hat{a}_{TT} \, \frac{h_1^u(x_1, M^2)\, h_1^u(x_2, M^2)}{u(x_1, M^2)\, u(x_2, M^2)} \,, \tag{3}$$

  where all distribution functions refer to protons ($\bar{q}^{\,\bar{p}} = q^p = q$, *etc.*). A_{TT} allows then a direct access to $|h_1(x)|$.

- When running in the collider mode (see Sec. 14) the energy range covered by PAX increases up to $s \simeq 200$ GeV^2 and $M^2 \simeq 100$ GeV^2, while the value of A_{TT} remains safely above 20%. The (x_1, x_2) kinematical regions covered by the PAX measurements, both in the fixed target and collider mode, are described in Fig. 1, left side. The plots on the right side show the expected values of the asymmetry A_{TT} as a function of Feynman $x_F = x_1 - x_2$, for different values of s and $Q^2 = 16$ GeV^2. The collider experiment plays, for the transversity distribution $h_1(x, M^2)$, the same role polarized inclusive DIS played for the helicity distribution $\Delta q(x, Q^2)$, with a kinematical (x, Q^2) coverage similar to that of the HERMES experiment.

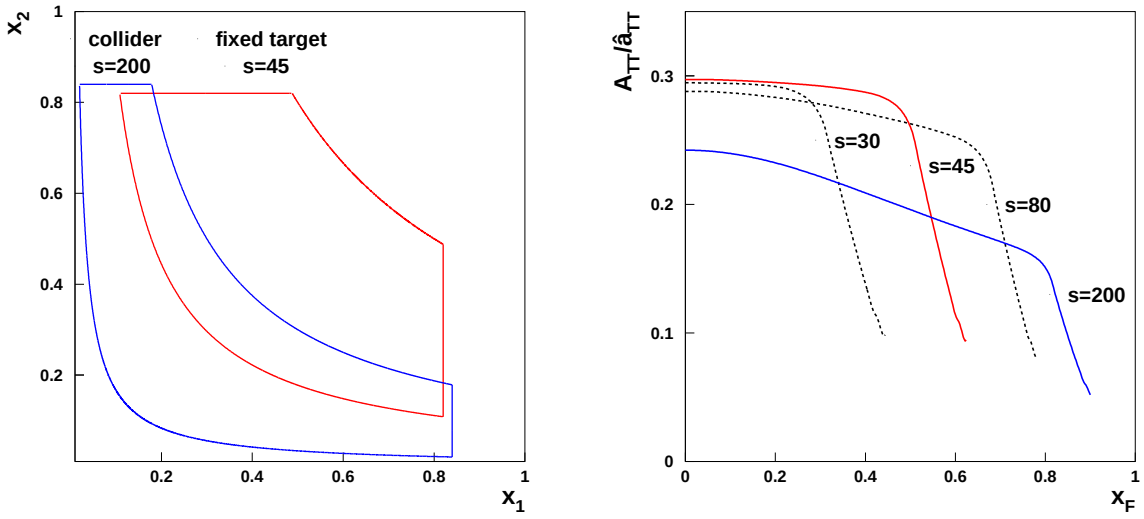

Figure 1: Left: The kinematic region covered by the h_1 measurement at PAX in phase II. In the asymmetric collider scenario (blue) antiprotons of 15 GeV/c impinge on protons of 3.5 GeV/c at c.m. energies of $\sqrt{s} \sim \sqrt{200}$ GeV and $Q^2 > 4$ GeV^2. The fixed target case (red) represents antiprotons of 22 GeV/c colliding with a fixed polarized target ($\sqrt{s} \sim \sqrt{45}$ GeV). Right: The expected asymmetry as a function of Feynman x_F for different values of s and $Q^2 = 16$ GeV^2.

- The counting rates for Drell–Yan processes at PAX are estimated in Sec. 4. We notice here that in the quest for h_1^q one should not confine to the $M > 4$ GeV region, which is usually considered as the "safe" region for the comparison with the pQCD computations, as this cut–off eliminates the background from the $J/\Psi, \Psi'$ production and their subsequent leptonic decay. Also the region $1.5 \lesssim M \lesssim 3$ GeV is free from resonances and can be exploited to access h_1 via Drell–Yan processes [3, 31].

- Even the $J/\Psi, \Psi'$ resonance region at $M \simeq 3$ GeV could be crucial [2]. The cross section for dilepton production increases by almost 2 orders of magnitude going from $M = 4$ to $M = 3$ GeV [32, 33, 34]: this cross section involves unknown quantities related to the $q\bar{q} - J/\Psi$ coupling. However, independently of these unknown quantities, the $q\bar{q} - J/\Psi$ coupling is a vector one, with the same spinor and Lorentz structure as the $q\bar{q} - \gamma^*$ coupling; similarly for the $J/\Psi - e^+e^-$ decay. These unknown quantities cancel in the ratio giving A_{TT}, while the helicity structure remains, so that Eq. (3) still holds in the J/Ψ resonance region [2]. This substantially enhances the sensitivity of the PAX experiment to A_{TT} and the amount of direct information achievable on $h_1^u(x_1, M^2)\, h_1^u(x_2, M^2)$. The theoretical analysis of the NLO corrections to A_{TT} for prompt photon production in hadronic collisions has already been accomplished [35], the full computation of QCD corrections to A_{TT}, relevant to PAX kinematical values

(including the $J/\Psi, \Psi'$ resonance region), is in progress [36].

2.3 Transversity in D–Meson Production at PAX

The double transverse spin asymmetry A_{TT} can be studied also for other processes; in particular, the open charm production, $\bar{p}^{\uparrow}\, p^{\uparrow} \to D\, X$ looks like a very promising channel to extract further information on the transversity distributions. At PAX in collider mode ($\sqrt{s} \simeq \sqrt{210}$ GeV) the production of D mesons with p_T of the order of 2 GeV/c is largely dominated by the $\bar{q}q \to \bar{c}c$ elementary process [37]; then one has (again, all distribution functions refer to protons):

$$A_{TT}^{D} \simeq \frac{\sum_q h_1^q(x_1) \otimes h_1^q(x_2) \otimes \Delta\hat{\sigma} \otimes D(z)}{\sum_q q(x_1) \otimes q(x_2) \otimes \hat{\sigma} \otimes D} \,, \tag{4}$$

which supplies information about the convolution of the transversity distributions with the fragmentation functions $D(z)$ of c quarks or antiquarks into D mesons, which are available in the literature; $\Delta\hat{\sigma} = \hat{\sigma}^{\uparrow\uparrow} - \hat{\sigma}^{\uparrow\downarrow}$ is the known double spin asymmetry for the $\bar{q}q \to \bar{c}c$ elementary process. Eq. (4) holds above the resonance region ($M = \sqrt{x_1 x_2 s} > 4$ GeV); the elementary interaction is a pQCD process, so that the cross section for D–production might even be larger, at the same scale, than the corresponding one for Drell–Yan processes. Notice that, once more, the same channel at RHIC cannot supply information on h_1, as at RHIC energy ($\sqrt{s} = 200$ GeV), the dominant contribution to D production comes from the $gg \to \bar{c}c$ elementary channel, rather than the $\bar{q}q \to \bar{c}c$ one [38].

3 Single Spin Asymmetries and Sivers Function

While the direct access to transversity is the outstanding, unique possibility offered by the PAX proposal concerning the proton spin structure, there are several other spin observables related to partonic correlation functions which should not be forgotten. These might be measurable even before the antiproton polarization is achieved.

The perturbative QCD spin dynamics, with the helicity conserving quark–gluon couplings, is very simple. However, such a simplicity does not always show up in the hadronic spin observables. The observed single spin asymmetries (SSA) are a symptom of this feature. By now it is obvious that the non–perturbative, long–distance QCD physics has many spin properties yet to be explored. A QCD phenomenology of SSA seems to be possible, but more data and new measurements are crucially needed. A new experiment with antiprotons scattered off a polarized proton target, in a new kinematical region, would certainly add valuable information on such spin properties of QCD.

As a first example we consider the transverse SSA

$$A_N = \frac{d\sigma^{\uparrow} - d\sigma^{\downarrow}}{d\sigma^{\uparrow} + d\sigma^{\downarrow}} \,, \tag{5}$$

measured in $p^\uparrow\, p \to \pi\, X$ and $\bar{p}^\uparrow\, p \to \pi\, X$ processes: the SSA at large values of x_F ($x_F \gtrsim 0.4$) and moderate values of p_T ($0.7 < p_T < 2.0$ GeV/c) have been found by several $p^\uparrow\, p$ experiments [24, 25, 26] to be unexpectedly large (up to about 40%), and similar values and trends of A_N have been observed in experiments with center of mass energies ranging from 6.6 up to 200 GeV.

The large effects were unexpected because, within the standard framework of collinear QCD factorization, one has to resort to subleading twist functions in order to obtain non–zero SSA [39, 40]. However, if the factorization approach is extended to not only include longitudinal but also transverse parton momenta, non–vanishing SSA emerge already at leading twist. In such an approach the above mentioned Sivers parton distribution [4] and Collins fragmentation function [5] enter. In order to disentangle both effects the study of SSA for D–meson production ($\bar{p}^\uparrow\, p \to D\, X$ or $\bar{p}\, p^\uparrow \to D\, X$) is very promising. At the PAX collider energy, for a final D with p_T of about 2 GeV/c, the dominant subprocess is $\bar{q}q \to \bar{c}c$ [37], with the subsequent fragmentation of a charmed quark into a charmed meson. In this elementary annihilation process there is no transverse spin transfer and the final c and $\bar{c}$ are not polarized. Therefore, there cannot be any contribution to the SSA from the Collins mechanism. A SSA could only result from the Sivers mechanism, coupled to an unpolarized elementary reaction and fragmentation. A measurement of a SSA in $\bar{p}^\uparrow\, p \to D\, X$ or $\bar{p}\, p^\uparrow \to D\, X$ would then allow a clean access to the quark Sivers function, active in an annihilation channel. This is not the case at RHIC energies, where the leading subprocess turns out to be $gg \to \bar{c}c$, which could lead to information on the gluon Sivers function [38].

The Sivers function (denoted by $f_{1T}^\perp$) attracted quite some interest over the past three years. It belongs to the class of the so–called (naive) time–reversal odd (T–odd) parton distributions, which are in general at the origin of SSA. Therefore, it was believed for about one decade that the Sivers function vanishes because of T–invariance of the strong interaction [5]. However, in 2002 it was shown that $f_{1T}^\perp$ can actually be non–zero [41, 8]. In this context it is crucial that the Wilson line, which ensures color gauge invariance, is taken into account in the operator definition of the Sivers function. The Wilson line encodes initial state interactions in the case of the Drell–Yan process and final state interactions of the struck quark in the case of DIS. The Sivers function, describing the (asymmetric) distribution of quarks in a transversely polarized nucleon [4], contains a rich amount of information on the partonic structure of the nucleon. E.g., it is related to the orbital angular momentum of partons, and the sign of the Sivers asymmetry of a given quark flavor is directly connected with the sign of the corresponding anomalous magnetic moment [42].

It is now important that the Wilson line can be process dependent. This property leads to the very interesting prediction that the Sivers function in Drell–Yan and in semi–inclusive DIS (measured for instance via the transverse SSA $l\, p^\uparrow \to l\, \pi\, X$) should have a reversed sign [8], i.e.,

$$f_{1T}^\perp\Big|_{DY} = -f_{1T}^\perp\Big|_{DIS}\,. \tag{6}$$

In the meantime, the HERMES collaboration has already obtained first results for the

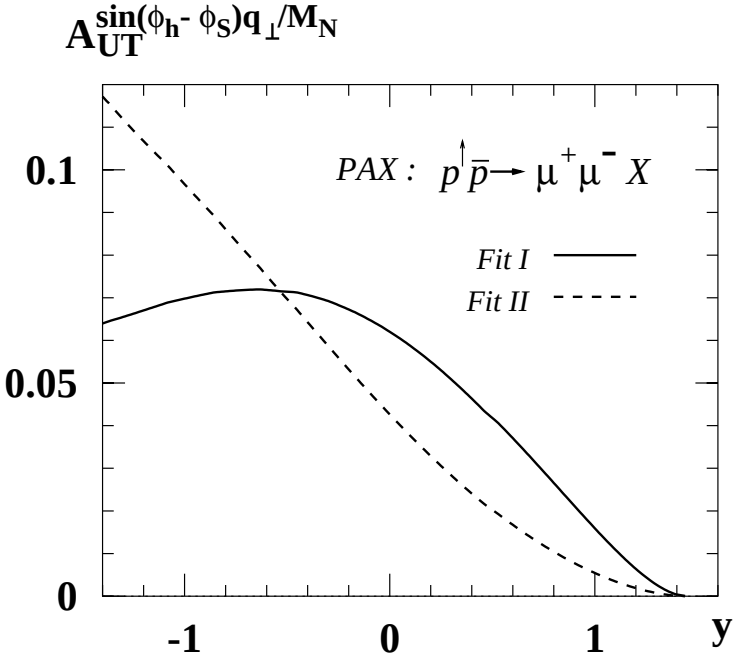

Figure 2: The SSA $A_{UT}^{\sin(\phi_h - \phi_S)q_\perp/M_N}$ in Drell-Yan lepton pair production, $p^\uparrow\bar{p} \to \mu^+\mu^- X$, as function of the rapidity y for typical PAX kinematics ($s = 45\,\mathrm{GeV}^2$, $M^2 = 2.5\,\mathrm{GeV}^2$). The different curves correspond to equally good fits to the HERMES data[7].

Sivers asymmetry in semi–inclusive DIS [7]. Therefore, measuring $f_{1T}^\perp$ in Drell–Yan processes (like $\bar{p}\,p^\uparrow \to l^+\,l^-\,X$ or $\bar{p}^\uparrow\,p \to l^+\,l^-\,X$) at PAX would check the clean–cut prediction in Eq. (6) based on the QCD factorization approach. An experimental check of the sign–reversal would crucially test our present day understanding of T–odd parton distributions and, consequently, of the very nature of SSA within QCD. In passing, we note that, within slightly different contexts, recently several other papers have also stressed the importance of measuring SSA in Drell–Yan processes [43, 44, 45, 46, 47].

On the basis of the recent HERMES data [7] for $f_{1T}^\perp$ a prediction for the corresponding Sivers asymmetry in Drell Yan for PAX (for $p^\uparrow\bar{p} \to \mu^+\mu^- X$) has been reported [48]. The main result of this study is shown in Fig. 2, where the (weighted) asymmetry

$$A_{UT}^{\sin(\phi-\phi_S)\frac{q_T}{M_N}}(y, M^2) = 2\,\frac{\sum_a e_a^2\, x_1 f_{1T}^{\perp(1)a/p}(x_1, M^2)\, x_2 f_1^{\bar{a}/\bar{p}}(x_2, M^2)}{\sum_a e_a^2\, x_1 f_1^{a/p}(x_1, M^2)\, x_2 f_1^{\bar{a}/\bar{p}}(x_2, M^2)} \tag{7}$$

is plotted. The weighting is performed for technical reasons and is done with $\sin(\phi - \phi_S)$ (ϕ and ϕ_S respectively denoting the azimuthal angle of the virtual photon and the target spin vector), and with the transverse momentum $\vec{q}_T$ of the lepton pair. The quantity $f_{1T}^{\perp(1)}$ represents the second moment of the Sivers function with respect to the transverse quark

momentum. In Fig. 2 the asymmetry is displayed as function of the rapidity y of the lepton pair. (Note the relation $x_{1/2} = \sqrt{M^2/s}\, e^{\pm y}$.) On the basis of this study asymmetries of the order $5 - 10\%$ can be expected [48] — an effect which should definitely be measurable at PAX. This would allow one to check the predicted sign–flip of the Sivers function in the valence region, even if the error bars would be large.

In summary, combining information on SSA from $p\,p^\uparrow$ and $\bar{p}^\uparrow\,p$ processes would greatly help in disentangling the Sivers and Collins mechanism. In this context production of charmed mesons (via $\bar{p}^\uparrow\,p \to D\,X$ or $\bar{p}\,p^\uparrow \to D\,X$) can play a crucial role because these asymmetries are not sensitive to the Collins function. We have also emphasized the importance of measuring the Sivers function in Drell–Yan. Through such an experiment, in combination with the already available information on the Sivers function coming from semi–inclusive DIS, a crucial check of our current understanding of the origin of T–odd parton distributions and of SSA within QCD can be achieved in an unprecedented way.

4 Electromagnetic Form Factors of the Proton

The form factors of hadrons as measured both in the space–like and time–like domains provide fundamental information on their structure and internal dynamics. Both the analytic structure and phases of the form factors in the time–like regime are connected by dispersion relations (DR) to the space–like regime [12, 13, 14, 49, 50]. The recent experiments raised two serious issues: firstly, the Fermilab E835 measurements of $|G_M(q^2)|$ of the proton at time–like $q^2 = 11.63$ and 12.43 GeV^2 ([51] and references therein) have shown that $|G_M(q^2)|$ in the time–like region is twice as large as in the space–like region (there are some uncertainties because the direct $G_E - G_M$ separation was not possible due to statistics and acceptance); secondly, the studies of the electron–to–proton polarization transfer in $\overrightarrow{e}^{-}\,p \to e^-\,\overrightarrow{p}$ scattering at Jefferson Laboratory [9] show that the ratio of the Sachs form factors $G_E(q^2)/G_M(q^2)$ is monotonically decreasing with increasing $Q^2 = -q^2$, in strong contradiction with the G_E/G_M scaling assumed in the traditional Rosenbluth separation method, which may in fact not be reliable in the space–like region. Notice that the core of the PAX proposal is precisely the QED electron–to–nucleon polarization transfer mechanism, employed at Jefferson Laboratory.

There is a great theoretical interest in the nucleon time–like form factors. Although the space–like form factors of a stable hadron are real, the time–like form factors have a phase structure reflecting the final–state interactions (FSI) of the outgoing hadrons. Kaidalov et al. argue that the same FSI effects are responsible for the enhancement of $|G_M(q^2)|$ in the time–like region [55]; their evaluation of the enhancement based on the variation of Sudakov effects from the space–like to time–like region is consistent with general requirements from analyticity that FSI effects vanish at large q^2 in the pQCD asymptotics. A recent discussion can be found in Brodsky et al. [11] (see also [14]). The same property of vanishing FSI at large q^2 is shared by the hybrid pQCD–DR description developed by Hammer, Meissner and Drechsel [13] and vector–dominance based models (VDM) [56], which are also able to accommodate the new results from the Jefferson Laboratory. Iachello et al. [57] stress the

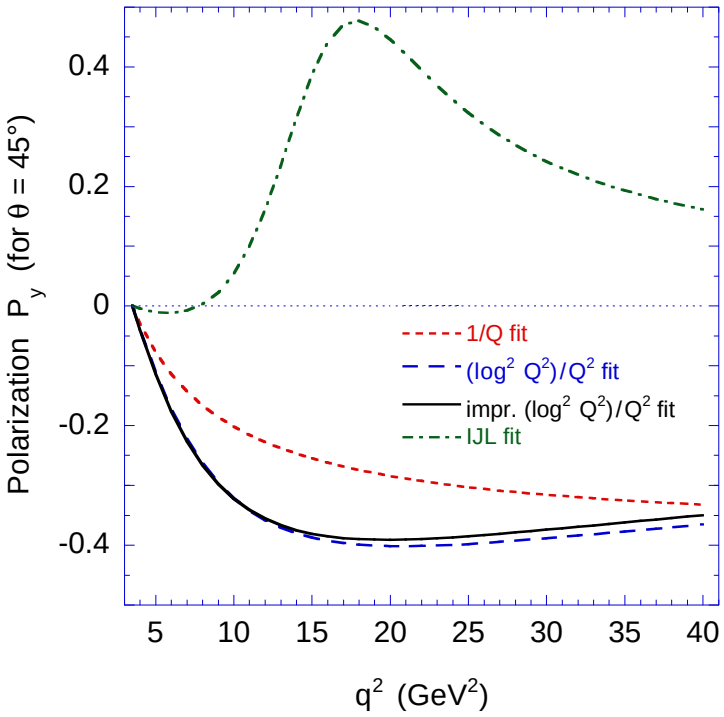

Figure 3: Predicted single–spin asymmetry $\mathcal{A}_y = \mathcal{P}_y$ for $\theta = 45°$ in the time–like region for selected form factor fits: $F_2/F_1 \propto 1/Q$ fit [11], the $(\log^2 Q^2)/Q^2$ fit of Belitsky *et al.* [52]; an improved $(\log^2 Q^2)/Q^2$ fit [53]; and a fit from Iachello *et al.*, [54].

need for a better accuracy measurement of the neutron time–like form factors.

Brodsky et al. make a strong point that the new Jefferson Laboratory results make it critical to carefully identify and separate the time–like G_E and G_M form factors by measuring the center–of–mass angular distribution and the polarization of the proton in $e^+e^- \to p\bar{p}$ or the transverse SSA in polarized $p^\uparrow\bar{p} \to \ell^+\ell^-$ reactions [11]. As noted by Dubnickova, Dubnicka, and Rekalo [10] and by Rock [58], the non–zero phase difference between G_E and G_M entails the normal polarization $\mathcal{P}_y$ of the final state (anti)baryons in $e^-e^+ \to \overrightarrow{p}\bar{p}$ or the transverse SSA $\mathcal{A}_y = \mathcal{P}_y$ in annihilation $p^\uparrow\bar{p} \to e^-e^+$ on transversely polarized protons:

$$\mathcal{A}_y = \frac{\sin 2\theta \, \mathrm{Im} G_E^* G_M}{[(1+\cos^2\theta)|G_M|^2 + \sin^2\theta |G_E|^2/\tau]\sqrt{\tau}} \tag{8}$$

where $\tau \equiv q^2/4m_p^2 > 1$ and θ is the scattering angle.

As emphasized already by Dubnickova et al. [10] the knowledge of the phase difference between the G_E and G_M may strongly constrain the models for the form factors. More recently there have been a number of explanations and theoretically motivated fits of the new data on the proton F_2/F_1 ratio [52, 59, 60, 53]. Each of the models predicts a specific fall–off and phase structure of the form factors from $s \leftrightarrow t$ crossing to the time–like domain.

The predicted single–spin asymmetry is substantial and has a distinct q^2 dependence which strongly discriminates between the analytic forms which fit the proton G_E/G_M data in the space–like region. This is clearly illustrated in Fig. 3. The further illustration of the discrimination power of A_y comes from the analytic and unitary vector–meson dominance (VDM) models developed by Dubnicka et al. [10], see Fig. 4, which indicate a strong model–dependence of P_y and more structure in the threshold region than suggested by large–q^2 parameterizations shown in Fig. 3. Finally, as argued in [61], the experimental observation of near–threshold exclusive Drell–Yan reactions $\bar{p}p \to \gamma^* \pi^o \to e^+ e^- \pi^o$ would give unique, albeit a model-dependent, access to the proton form factors in the unphysical region of $q^2 < 4m_p^2$.

Despite the fundamental implications of the phase for the understanding of the connection between the space–like and time–like form factors, such measurements have never been made. The available data on $|G_M^{(p)}|$ in the time–like region are scarce, as can be seen from Fig. 5.

However, these data suggest the existence of additional structures in the time–like form factor of the proton, especially in the near–threshold region; as Hammer, Meissner and Drechsel emphasized [13] that calls for improvements in the dispersion–theoretical description of form factors. We also recall recent indications for the baryonium–like states from BES in the $J/\Psi \to \gamma \bar{p}p$ decay [63] and from Belle [64, 65], which prompted much theoretical activity in low–energy proton–antiproton interactions ([66] and references therein). The phase structure of the form factors near threshold could be much richer than suggested by high–Q^2 parameterizations with an oversimplified treatment of the impact of the unphysical region.

At larger q^2 the data from E835 [62, 51] and E760 [67] seem to approach the power–law behavior predicted by pQCD. The PAX experiment would measure the relative phase ϕ_{EM} of the form factors from the SSA data with a transversely polarized proton target.

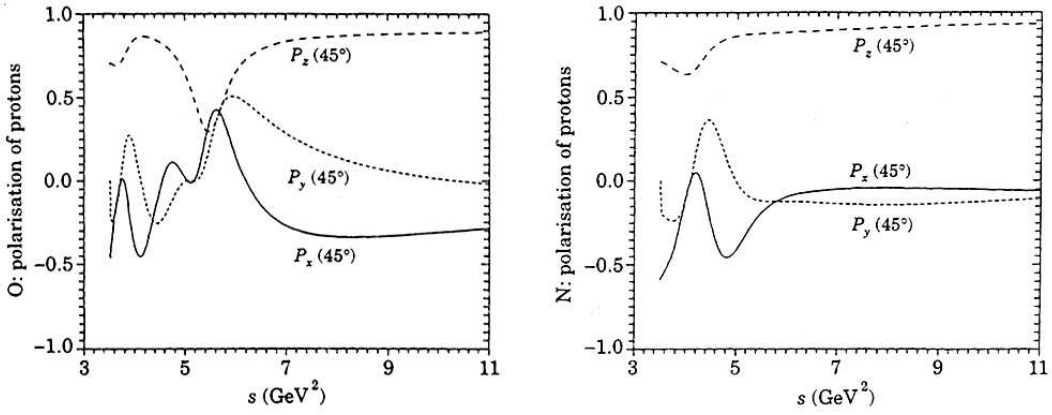

Figure 4: Predicted single–spin asymmetries ($\mathcal{A}_y = \mathcal{P}_y$) for $\theta = 45°$ in the time–like region for two versions (O (old) & N (new)) of the analytic and unitary vector–meson dominance (VDM) models [10]

The modulus of G_E and G_M can be deduced from the angular distribution in an unpolarized measurement for $\bar{p}p \to e^+e^-$ as it can be carried out independently at PANDA as well as at PAX. However, the additional measurement of the transverse double spin asymmetry in $p^\uparrow\bar{p}^\uparrow \to \ell^+\ell^-$, that is feasible at PAX, could further reduce the systematic uncertainties of the Rosenbluth separation. We recall that, as emphasized by Tomasi–Gustaffson and Rekalo [68], the separation of magnetic and electric form factors in the time–like region allows for the most stringent test of the asymptotic regime and QCD predictions. According to Dubnicka et al. [10]

$$\mathcal{A}_{yy} = \frac{\sin^2\theta\,(G_M|^2 - |G_E|^2/\tau)/\mathrm{Im}}{[(1+\cos^2\theta)|\mathrm{G_M}|^2 + \sin^2\theta|\mathrm{G_E}|^2/\tau]}\,. \tag{9}$$

Furthermore, in the fixed–target mode, the polarization of the proton target can readily be changed to the longitudinal direction, and the in–plane longitudinal–transverse double spin asymmetry would allow one [10] to measure $\mathrm{Re}G_E^*G_M$,

$$\mathcal{A}_{xz} = \frac{\sin 2\theta\,\mathrm{Re}G_E^*G_M}{[(1+\cos^2\theta)|G_M|^2 + \sin^2\theta|G_E|^2/\tau]}, \tag{10}$$

which would resolve the remaining $\phi_{EM} - (\pi - \phi_{EM})$ ambiguity from the transverse SSA data. This will put tight constraints on current models of the form factor.

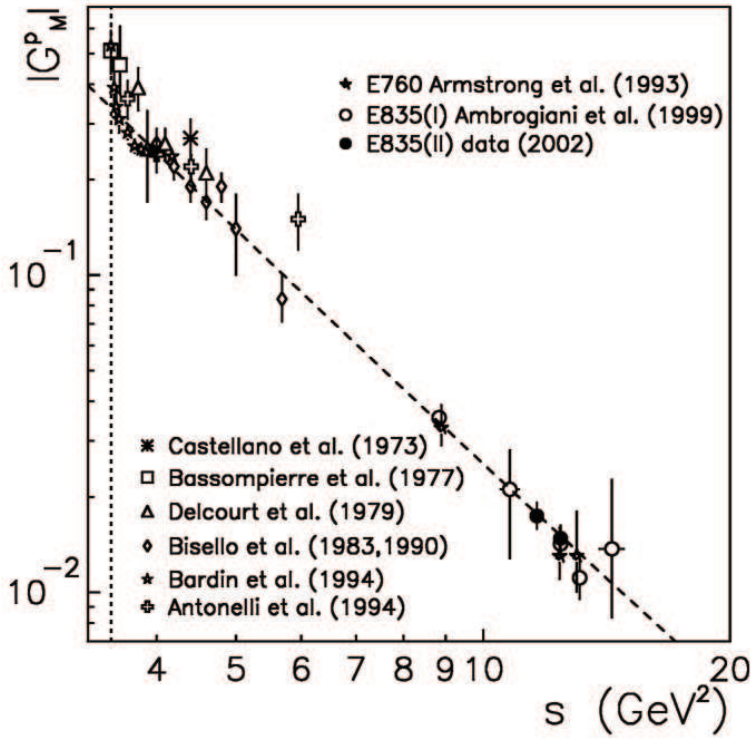

Figure 5: All existing magnetic form factor data of the proton in the time–like region obtained with the hypothesis $|G_M| = |G_E|$ versus $s = q^2$, as compiled in [51]; the summary of the earlier data can be found in [62].

5 Hard Scattering: Polarized and Unpolarized

From the point of view of the theory of elastic and exclusive two–body reactions, the energy range of HESR corresponds to the transition from soft mechanisms to hard scattering with the onset of the power laws for the s, t, u–dependence of the differential cross sections [15, 16] which have generally been successful so far (for a review and further references see [69]). There remains, though, the open and much debated issue of the so–called Landshoff independent scattering–mechanism [18] which gives the odd–charge symmetry contribution to the NN and $\bar{N}N$ amplitudes and may dominate at higher energies. The more recent realization of the importance of the so–called handbag contributions to the amplitudes of exclusive reactions made possible direct calculations of certain two–body annihilation cross sections and double–spin asymmetries in terms of the so–called Generalized Parton Distributions (GPD's) [70, 71, 72]. The PAX experiment at HESR is uniquely poised to address several new aspects of hard exclusive scattering physics:

- The particle identification in the forward spectrometer of PAX would allow the measurement of elastic $p\bar{p}$ scattering in the small to moderately large $|t|$ in the forward hemisphere and, more interestingly, the backward hemisphere at extremely large t not accessible in the $t - u$ symmetric pp scattering.

- The high energy behavior of exotic baryon number, $B = 2$, exchange in the u–channel is interesting by itself. Its measurements in the small to moderately large u region of backward elastic $\bar{p}p$ scattering will be used for the isolation of hard $p\bar{p}$ scattering contribution at large $|u|$.

- After the isolation of the hard–scattering regime the importance of the odd–charge symmetry Landshoff (odderon) mechanism can be tested from the onset of the hard scattering regime in large–angle elastic $\bar{p}p$ scattering as compared to pp scattering.

- The relative importance of odd–charge vs. even–charge symmetric mechanisms for the large transverse double spin asymmetry A_{TT} in polarized $p^{\uparrow}p^{\uparrow}$ as observed at Argonne ZGS and BNL AGS can be clarified by a measurement of A_{TT} in polarized $\bar{p}^{\uparrow}p^{\uparrow}$ elastic scattering at PAX and the comparison with the earlier data from $p^{\uparrow}p^{\uparrow}$ scattering.

- The future implementation of particle identification in the large angle spectrometer of PAX would allow an extension of measurements of elastic scattering and two–body annihilation, $\bar{p}p \to \gamma\gamma, \gamma\pi^0, \pi^+\pi^-, K^+K^-, \Lambda_c\bar{\Lambda}_c, ...$ to large angles $\theta_{cm} \sim 90^o$.

- Exclusive Drell–Yan reactions with a lepton pair in the final state, accompanied by a photon or meson, may also be studied in the framework of the partonic description of baryons. Like in the conventional inclusive DY process, the large mass of the lepton pair sets the resolution scale of the inner structure of the baryon to photon or meson transition processes.

The theoretical background behind the high–t or high–Q^2 ($Q^2 = M^2_{e^+e^-}$) possibilities of PAX can be summarized as follows:

The scaling power law s^{-N}, where $N+2$ is the total number of elementary constituents in the initial and final state, for exclusive two–body hard scattering has been in the focus of high–energy scattering theory ever since the first suggestion in the early 70's of the constituent counting rules by Matveev et al. [15] and Brodsky & Farrar [16] and Brodsky & Hiller [73]. The subsequent hard pQCD approach to the derivation of the constituent counting rules has been developed in late 70's–early 80's and has become known as the Efremov–Radyushkin–Brodsky–Lepage (ERBL) evolution technique ([74, 75], see also Chernyak et al. [76]). Experimentally, the constituent counting rule proves to be fairly successful, from the scattering of hadrons on protons to photoproduction of mesons [77] to reactions involving light nuclei, like the photodisintegration of deuterons studied at Jefferson Lab [78, 79] A good summary of the experimental situation is found in Ref. [80] and reviews by Brodsky and Lepage ([69] and references therein), and is summarized in Table 1, borrowed from the BNL E838 publication [80] .

		Cross section		$n-2$
No.	Interaction	E838	E755	$(\frac{d\sigma}{dt} \sim 1/s^{n-2})$
1	$\pi^+ p \to p\pi^+$	132 ± 10	4.6 ± 0.3	6.7 ± 0.2
2	$\pi^- p \to p\pi^-$	73 ± 5	1.7 ± 0.2	7.5 ± 0.3
3	$K^+ p \to pK^+$	219 ± 30	3.4 ± 1.4	$8.3^{+0.6}_{-1.0}$
4	$K^- p \to pK^-$	18 ± 6	0.9 ± 0.9	≥ 3.9
5	$\pi^+ p \to p\rho^+$	214 ± 30	3.4 ± 0.7	8.3 ± 0.5
6	$\pi^- p \to p\rho^-$	99 ± 13	1.3 ± 0.6	8.7 ± 1.0
7	$\pi^+ p \to \pi^+\Delta^+$	45 ± 10	2.0 ± 0.6	6.2 ± 0.8
8	$\pi^- p \to \pi^+\Delta^-$	24 ± 5	≤ 0.12	≥ 10.1
9	$pp \to pp$	3300 ± 40	48 ± 5	9.1 ± 0.2
10	$\overline{p}p \to p\overline{p}$	75 ± 8	≤ 2.1	≥ 7.5

Table 1: The computation of the experiments N of the scaling power in the AFS BNL experiments E838 ($E_p = 5.9$ GeV/c) and E755 ($E_p = 9.9$ GeV/c). The constituent counting predicts $N = 8$ for reactions 1 - 8 and $N = 10$ for reactions 9 and 10. (Table from Ref. [80]).

The scale for the onset of the genuine pQCD asymptotics can only be deduced from the experiment, on the theoretical side the new finding is the importance of the so–called handbag mechanism in the sub–asymptotic energy range [81, 82]. As argued by P. Kroll et al., the handbag mechanism prediction for the sub–asymptotic s–dependence of the

large–angle elastic pp and $p\bar{p}$ cross–section [17] ,

$$\frac{d\sigma}{dt} \propto \frac{1}{s^2 t^8} \propto \frac{f(\theta)}{s^{10}} \tag{11}$$

is similar to that of the constituent quark counting rules of Brodsky et al. [16].

There remains, though, an open and hot issue of the so–called Landshoff independent scattering–mechanism [18], which predicts $d\sigma/dt \propto 1/t^8 \propto f_L(\theta)/s^8$ and, despite the Sudakov suppression, may dominate at very large s. According to Ralston and Pire [19] certain evidence for the relevance of the Landshoff mechanism in the HESR energy range comes from the experimentally observed oscillatory s–dependence of $R_1 = s^{10} d\sigma/dt$, shown in Fig. 6. Here the solid curve is the theoretical expectation [19] based on the interference of the Brodsky–Farrar and Landshoff mechanisms. The Ralston–Pire mechanism has been

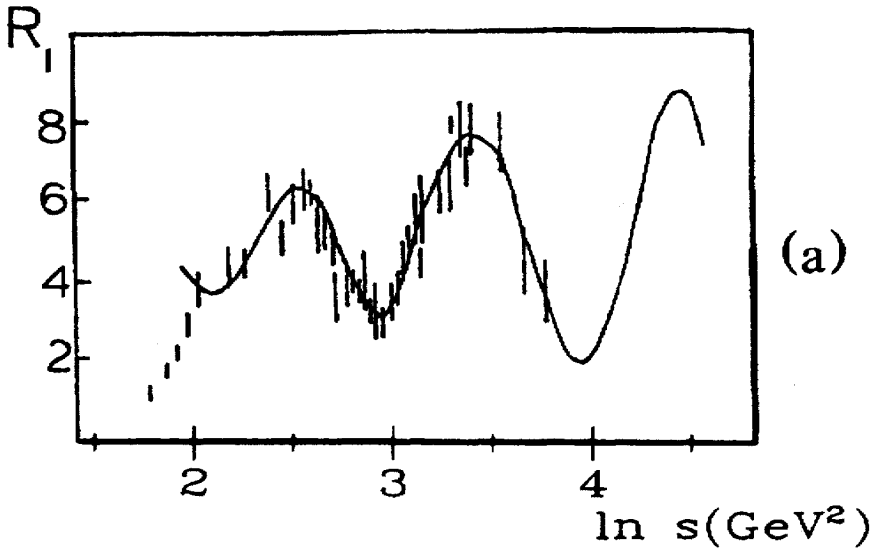

Figure 6: The energy dependence of $R_1 = s^{10} d\sigma_{pp}/dt|_{90^o}$ for the high energy pp elastic scattering at 90^o c.m. angle compared to the model calculation [19] from the interference of the Brodsky–Farrar and Landshoff mechanisms.

corroborated to a certain extent by the experimental finding at BNL of the wash–up of oscillations in the quasielastic scattering of protons on protons bound in nuclei ([83] and references therein).

To the lowest order in pQCD the Landshoff amplitude corresponds to the charge conjugation–odd (odderon) exchange and alters the sign from the pp to the $p\bar{p}$ case. If the Brodsky–Farrar and/or it's handbag counterpart were crossing–even, then the Ralston–Pire scenario for the oscillations would predict the inversion of the sign of oscillation in R_1 from the pp to the $p\bar{p}$ case. Because the first oscillation in Fig. 6 takes place at $s < 20$ GeV^2, this suggests that $\bar{p}p$ elastic scattering at HESR is ideally suited for testing the oscillation scenarios. Although true in general, this expectation needs a qualification on

the crossing from the proton–proton to the antiproton–proton channel. A natural origin for the constituent counting rules is offered by the quark interchange mechanism (QIM) which predicts $d\sigma_{el}(pp) \gg d\sigma_{el}(\bar{p}p)$ in accord with the experimental data from BNL E838 shown in Fig. 7.

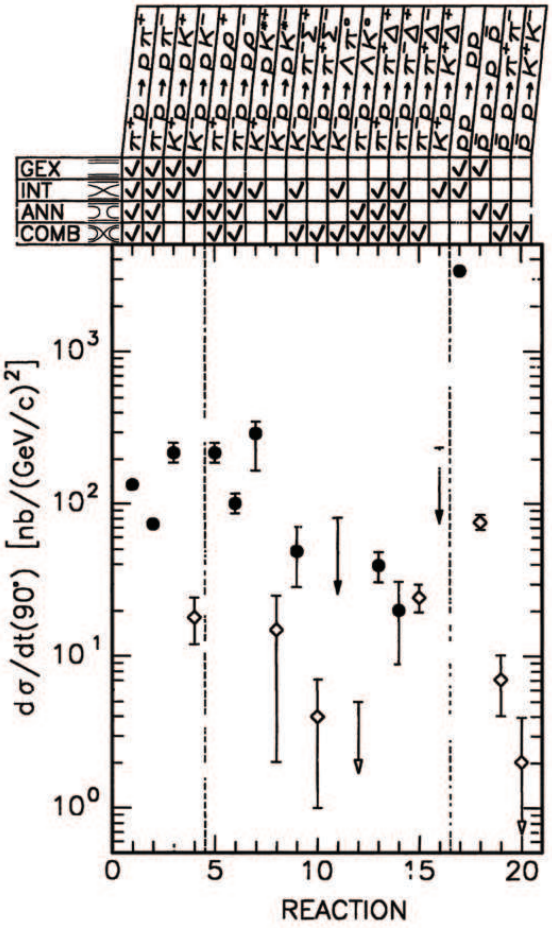

Figure 7: Differential cross sections for the 16 meson–baryon and 4 baryon–baryon reactions measured in the BNL AFS experiment E838 [80]. The four possible quark–gluon diagrams which contribute to each of the 20 reactions are given in the chart at the top of the figure. The experimental data for those reactions which have a contribution from quark interchange mechanism (INT) are shown by the solid black points.

Either the contribution from the independent scattering mechanism is small or at $E_p = 5.9$ GeV in E838 the cancellation of the QIM and the Landshoff amplitudes is accidentally strong in which case the energy dependence of $d\sigma_{el}(\bar{p}p)$ could prove exceptionally non–smooth. On the theoretical side, as early as in 1974, Nielsen and Neal suggested the version of an independent scattering mechanism which allows for a substantial crossing–even component [84]. The Kopeliovich–Zakharov pQCD decameron (four–gluon) exchange realization [85] of the Rossi–Veneziano [86] baryon–junction, much discussed recently in

view of the enhanced yield of baryons in nuclear collisions at RHIC [87], also is a multiple–scattering mechanism. The decameron amplitude decreases at large $|t|$ as slowly as the Landshoff amplitude and contributes only to the $p\bar{p}$ scattering.

The point that polarization observables are sensitive to mechanisms for the scaling behavior is conspicuous. As an example we cite the very recent experimental finding of the onset of pQCD constituent counting scaling [73] in photodisintegration of the deuteron starting from the proton transverse momentum p_T above about 1.1 GeV [78]. On the other hand, the experimentally observed non-vanishing polarization transfer from photons to protons indicates that the observed scaling behavior is not a result of perturbative QCD [88].

Now we recall that very large double transverse asymmetries have been observed in hard proton–proton scattering ([89] and references therein). The HESR data with polarized antiprotons at PAX will complement the AGS–ZGS data in a comparable energy range. In 1974 Nielsen et al. argued [84] that within the independent scattering models the change from the dominance by 1×1 parton–parton scattering to the 2×2 and 3×3 scattering leads in a natural way to the oscillatory (and rising with t) behavior of polarization effects. Within this approach Nielsen et al. [90] reproduce the gross features of the ZGS data [89] although they underpredict A_{TT} at largest t. Within the QCD motivated approach, initiated in Ref. [91], the helicity properties of different hard scattering mechanisms have been studied by Ramsey and Sivers [20]. These authors tried to extract the normalization of the Landshoff amplitude from the combined analysis of pp and $p\bar{p}$ elastic scattering and argued it must be small to induce the oscillations or contribute substantially to the double spin asymmetry A_{TT}. This leaves open the origin of oscillations in R_1 but leads to the conclusion that the double spin asymmetry A_{TT} in $p^{\uparrow}\bar{p}^{\uparrow}$ at PAX and $p^{\uparrow}p^{\uparrow}$ as observed at AGS–ZGS must be of comparable magnitude. The comparison of A_{TT} in the two reactions will also help to constrain the Landshoff amplitude. More recently, Dutta and Gao [21] revisited the Ralston–Pire scenario with allowance for the helicity–non–conserving pp scattering amplitudes (for the early discussion of helicity–non–conservation associated with the Landshoff mechanism, see Ref. [92]). They found good fits to the oscillatory behavior of R_1 and the energy dependence of A_{TT} in pp scattering at 90^o starting from $s \gtrsim 8$ GeV^2. The extension of predictions from the models by Nielsen et al. and Dutta et al. to the crossing antiproton-proton channel is not yet unique, though. Brodsky and Teramond make a point that opening of the $|uuduudc\bar{c}\rangle$ channel at the open charm threshold would give rise to a broad structure in the $J = L = S = 1$ proton-proton partial wave [93]. Such a threshold structure would have a negative parity and affect $p^{\uparrow}p^{\uparrow}$ scattering for parallel spins normal to the scattering plane. The threshold structure also imitates the "oscillatory" energy dependence at fixed angle and the model is able to reproduce the gross features of the s and t dependence of A_{NN}. Arguably, in the $\bar{p}p$ channel the charm threshold is at much lower energy and the charm cross section will be much larger, and the Brodsky-Teramond mechanism would predict A_{NN} quite distinct from that in pp channel. Still, around the second charm threshold, $\bar{p}p \to \bar{p}p\bar{c}c$, the A_{NN} for $\bar{p}p$ may repeat the behavior exhibited in pp scattering.

Finally, the double–spin transverse-longitudinal asymmetry A_{TL} is readily accessible in the fixed-target mode with the longitudinal polarization of the target. Its potential must not be overlooked and needs further theoretical scrutiny.

The differential cross section measured in the BNL E838 experiment is shown in Fig. 7. The expected $d\sigma/dt \propto s^{-10}$ behavior suggests that in the fixed-target Cooler Synchrotron Ring (CSR) stage (Phase-I) the counting rates will allow measurements of elastic $p\bar{p}$ scattering, both polarized and unpolarized, over the whole range of angles. In the fixed-target HESR stage the measurement of unpolarized scattering can be extended to energies beyond those of the E838 experiment. The expected counting rates will also allow the first measurement of the double–spin observables.

In the comparison of observables for the pp and $\bar{p}p$ elastic scattering one would encounter manageable complications with the Pauli principle constraints in the identical particle pp scattering, by which the spin amplitudes for pp scattering have the t–u–(anti)symmetric form $M(\theta) \pm M(\pi - \theta) = M(t) \pm M(u)$ ([94] and references therein). Regarding the amplitude structure, the $\bar{p}p$ case is somewhat simpler and offers even more possibilities for the investigation of hard scattering. Indeed, for the hard scattering to be at work, in the general case one demands that both $|t|$ and $|u|$ are simultaneously large, $|t| \sim |u| \sim \frac{1}{2}(s - 4m_p^2)$. Here we notice an important distinction between the t–u asymmetric $\bar{p}p$ from the t–u symmetric identical particle pp elastic scattering. In the t–u symmetric case the accessible values of t are bound from above by $|t| \leq |t_{max}| = \frac{1}{2}(s - 4m_p^2)$. In the $p\bar{p}$ case the backward scattering corresponds to the strongly suppressed exotic baryon number two, $B = 2$, exchange in the u–channel (for a discussion of the suppression of exotic exchanges see Refs. [95, 96] and references therein). Consequently, the hard scattering mechanism may dominate well beyond $\theta_{\rm cm} = 90^o$ of $p\bar{p}$ elastic scattering. Because of the unambiguous p and $\bar{p}$ separation in the forward spectrometer, the PAX will for the first time explore the transition from soft exotic $B = 2$ exchange at $u \sim 0$ to the hard scattering at larger $|u|$: for 15 GeV stored $\bar{p}$'s the $p - \bar{p}$ separation is possible up to $|u| \leq 4$ GeV^2, while $|u| \leq 8$ GeV^2 is accessible at 22 GeV. Although still $|u| \ll s$, these values of $|u|$ are sufficiently large to suppress the u–channel exotic $B = 2$ exchange, which allow the dominance of hard mechanisms, which thus become accessible at values of $|t| = s - 4m_p^2 - |u|$ almost twice as large than in pp scattering at the same value of s. The investigation of the energy dependence of exotic $B = 2$ exchange in the small–u region is interesting by itself in order to better understand the related reactions, like the πD backward elastic scattering.

Although not all annihilation reactions are readily accessible with the present detector configuration, they are extremely interesting from the theoretical standpoint. Within the modern handbag diagram description, they probe such fundamental QCD observables as the Generalized Parton Distributions (GPD's), introduced by Ji and Radyushkin [70, 71]. These GPD's generalize the conventional parton-model description of DIS to a broad class of exclusive and few–body reactions and describe off–forward parton distributions for polarized as well as unpolarized quarks; the Ferrara Manifesto, formulated at the recent Conference on the QCD Structure of the Nucleon (QCD–N'02), lists the determination of GPD's as the major physics goal of future experiments in the electroweak physics sector [72]. The QCD evolution of GPD's is a combination of the conventional QCD evolution

for DIS parton densities and the ERBL evolution for the quark distribution amplitudes, GPD's share with the DIS parton densities and the ERBL hard–scattering amplitudes the hard factorization theorems: the one and the same set of GPD's at an appropriate hard scale enters the calculation of amplitudes for a broad variety of exclusive reactions.

There has been much progress in calculating the electromagnetic form factors of the nucleon and of the hard Compton scattering amplitudes in terms of the off–forward extension of the conventional parton densities [81, 82, 97, 98], Deeply Virtual Compton Scattering is being studied at all electron accelerators [99, 100] with the purpose to extract the specific GPD which would allow one to determine the fraction of the proton's spin carried by the orbital angular momentum of partons (the Ji sum rule [70]).

More recently, the technique of GPD's has been extended by P. Kroll and collaborators [101] to the differential cross sections and spin dependence of annihilation reactions. Here the hard scale needed for the applicability of the GPD technique is provided by $|t|$. The theory has been remarkably successful in the simplest case of $B\bar{B} \to \gamma\gamma$ with two point–like photons (the inverse reactions $\gamma\gamma \to p\bar{p}$, $\Lambda\bar{\Lambda}$, and $\Sigma\bar{\Sigma}$ have been studied experimentally by the CLEO [102] and VENUS [103] collaborations). A steady progress is being made by the DESY–Regensburg–Wuppertal group in extending these techniques to the $p\bar{p} \to \gamma\pi^0$ with a non–point–like π^0 in the final state [104], a further generalization to the two–meson final states is expected in the near future. As far as the theory of spin dependence of hard scattering is concerned the theoretical predictions are robust for the longitudinal double spin asymmetries, and thus their experimental confirmation will be of great theoretical interest. To make such observables accessible experimentally the spin of antiprotons in the HESR must be rotated by Siberian Snakes. In addition, the technique of GPD's should allow one to relate the transverse asymmetries to the Generalized structure function h_1^q (see above) but such a relationship has yet to be worked out.

A slightly different application of QCD factorization technique has been suggested recently by Pire and Szymanowski [105]. They propose to study the exclusive Drell-Yan annihilation reaction $p\bar{p} \to \gamma^*\gamma \to e^+e^-\gamma$. Like in the inclusive DY process, the required hard scale is provided by the large invariant mass of the lepton pair. Then one can study such reactions in the forward region which increases the observed cross section. The scaling of the cross section at fixed Q^2/s is then a signal of the applicability of perturbative QCD techniques. New observables, called proton to photon transition distribution amplitudes (TDA's), may then be measured which should shed light on the structure of the baryon wave functions. Polarization experiments are needed to separate the different TDA's. The same theoretical framework can also be applied to other reactions involving mesons in the final state, like $p\bar{p} \to \gamma^*\pi$ or $p\bar{p} \to \gamma^*\rho$ [106] (the former reaction has already been discussed in Sect. 4 as a window to the time-like form factors of the proton in the unphysical region). Crossing relates these reactions to backward deep electroproduction which may be accessed at electron accelerators.

6 Polarized Antiproton–Proton Soft Scattering

6.1 Low–t Physics

For energies above the resonance region elastic scattering is dominated by small momentum transfers and therefore total elastic cross sections are basically sensitive to the small t region only.

Dispersion theory (DT) is based on a generally accepted hypothesis that scattering amplitudes are analytic in the whole Mandelstam plane up to singularities derived from unitarity and particle/bound state poles. This, in combination with unitarity and crossing symmetry, allows extracting of e.g. the real part of the forward elastic scattering amplitude from knowledge of the corresponding total cross sections. The major unknown in this context is the unphysical region: a left hand cut that starts at the two pion production threshold and extends up to the $\bar{N}N$ threshold, where one is bound to theoretical models for the discontinuity; the extrapolation to asymptotic energies is considered to be well understood [107] and does not effect the DT predictions in the HESR energy range.

Under certain assumptions, the real part of the forward scattering amplitude can be extracted from the elastic differential cross section measured in the Coulomb-nuclear interference (CNI) region ([108] and references therein). The most recent DT analysis [22] reproduces the gross features of the available data, see Fig. 8; still, the experiment suggests more structure at low energies (which may be related to the near-threshold structure in the electromagnetic form factor shown in Fig. 5) and there is a systematic departure of the theoretical prediction from the experiment in the region between 1 and 10 GeV/c. In particular the latest precise results from Fermilab E760 Collaboration [23] collected in the 3.7 to 6.2 GeV/c region are in strong disagreement with DT. There are two explanations possible for this discrepancy. First one might doubt the theoretical understanding of the amplitude in the unphysical region. In this sense the DT analysis is a strong tool to explore the unphysical region. Since the discrepancy of the data to the result of the DT analysis occurs in a quite confined region, only a very pronounced structure in the unphysical region could be the origin. Such a structure can be an additional pole related to a $\bar{p}p$ bound state[1], discussed in Refs. [109, 110, 111, 112]. The appearance of a pole in the unphysical region might cause a turnover of the real part of the forward scattering amplitude to small values at momenta above 600 MeV/c [113, 114]. Indications of such states were seen recently at BES in the $J/\Psi \to \gamma\bar{p}p$ decay [63] and Belle [64, 65] and attracted much theoretical attention ([66] and references therein).

However, there is a second possible reason for the discrepancy of the DT result and the data, namely that not all assumptions in the analysis of CNI hold, the strongest one being a negligible spin dependence in the nuclear interference region [115]. A sizable spin dependence of the nuclear amplitude can well change the analysis used in Ref. [23]; such a sensitivity to a possible spin dependence has been discussed earlier [116]. The quantities to be measured are $\Delta\sigma_T = \sigma(\uparrow\downarrow) - \sigma(\uparrow\uparrow)$ and $\Delta\sigma_L = \sigma(\rightleftarrows) - \sigma(\rightrightarrows)$: their knowledge will

[1]Notice that already the present analysis of Ref. [22] contains one pole.

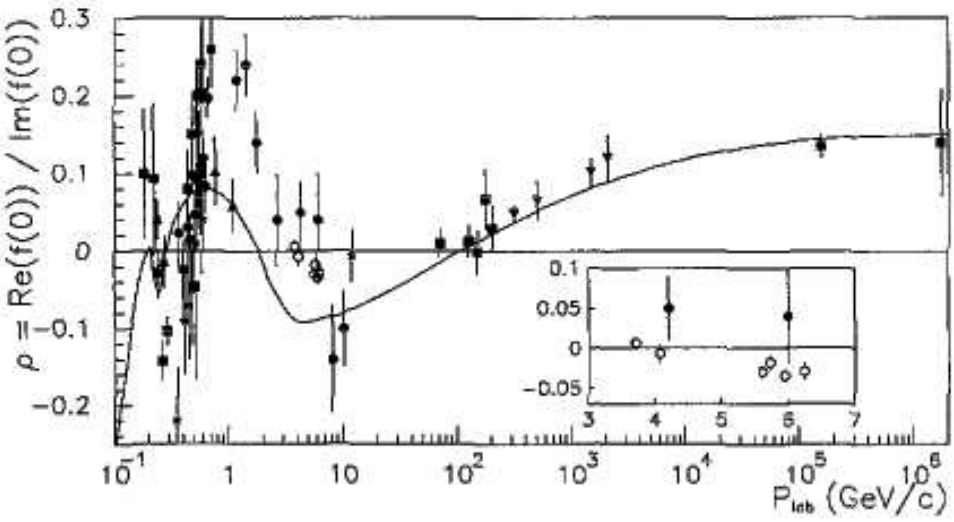

Figure 8: The compilation of the experimental data on the ratio of the real to imaginary part of the $\bar{p}p$ forward scattering amplitude (from E760 publication [23]). The insert shows on a larger scale the E760 results. The solid line shows the predictions from the dispersion relation calculation by P. Kroll et al. [22].

eliminate the model–dependent extraction of the real part of the $p\bar{p}$ scattering amplitude [117]. Please note that a sizable value of $\Delta\sigma_T$ or $\Delta\sigma_L$ at high energies is an interesting phenomenon in itself since it contradicts the generally believed picture that spin effects die out with increasing energy (see also previous section).

Thus, a measurement of $\Delta\sigma_{L/T}$ in the energy region accessible at HESR not only allows one to investigate spin effects of the $\bar{p}p$ interaction at reasonably high energies but also to pin down the scattering amplitude in the unphysical region to deepen our understanding of possible $\bar{p}p$ bound states. Especially a determination of $\Delta\sigma_T$ can be done in a straightforward way as outlined in the next section. The low-t physics program is ideally suited for the Phase–I with the polarized fixed target at CSR, and can further be extended to Phase–II.

6.2 Total Cross Section Measurement

The unpolarized total cross section $\sigma_{0,\mathrm{tot}}$ has been measured at several laboratories over the complete HESR momentum range; however, the spin dependent total cross section is comprised of three parts [118]

$$\sigma_{\mathrm{tot}} = \sigma_{0,\mathrm{tot}} + \sigma_{1,\mathrm{tot}}\vec{P}\cdot\vec{Q} + \sigma_{2,\mathrm{tot}}(\vec{P}\cdot\hat{k})(\vec{Q}\cdot\hat{k}). \tag{12}$$

where $\vec{P}, \vec{Q}$ are the beam and target polarizations and $\hat{k}$ the unit vector along the beam momentum. Note that the spin–dependent contributions $\sigma_{1,2}$ are completely unexplored over the full HESR energy range. Only one measurement at much higher energies from

E704 at 200 GeV/c [119] has been reported using polarized antiprotons from parity–non–conserving $\bar{\Lambda}$–decays.

With the PAX detector the transverse cross section difference $\Delta\sigma_T = -2\sigma_{1,\mathrm{tot}}$ can be accessed by two methods:

(1) from the rate of polarization buildup for a transversely polarized target when only a single hyperfine state is used. The contribution from the electrons is known from theory and can be subtracted. However, the difference of the time constants for polarization buildup with hyperfine states 1 *or* 2 (cf. Fig. 11) injected into the target, would give direct access to $\Delta\sigma_T$, whereas the contribution from the electrons could be extracted from the average.

(2) from the difference in beam lifetime for a target polarization parallel or antiparallel to the beam. A sensitive beam–current transformer (BCT) can measure beam lifetimes of the antiproton beam after polarization and ramping to the desired energy. An accuracy at the 10^{-4} level has been achieved by the TRIC experiment at COSY using this method. Access to $\Delta\sigma_T$ by this technique is limited to beam momenta where losses are dominated by the nuclear cross section, e.g. above a few GeV/c – the precise limit will be determined by the acceptance of the HESR.

Both methods require knowledge of the total polarized target thickness exposed to the beam. With a calibrated hydrogen source fed into the storage cell, the target density can be determined to 2–3% as shown by the HERMES [120] and FILTEX [121] experiments.

In principle, $\Delta\sigma_L = -2(\sigma_{1,\mathrm{tot}} + \sigma_{2,\mathrm{tot}})$ can be measured by the same method; however, a Siberian snake would be needed in the ring to allow for a stable longitudinal polarization at the interaction point.

6.3 Proton–Antiproton Interaction

The main body of $\bar{N}N$ scattering data has been measured at LEAR (see [122] for a recent review) and comprises mainly cross section and analyzing power data, as well as a few data points on depolarization and polarization transfer. These data have been interpreted by phenomenological or meson–exchange potentials by exploiting the G–parity rule, linking the $\bar{N}N$ and the NN systems.

At the HESR the spin correlation parameters A_{NN}, A_{SS}, and A_{SL} can be accessed for the first time by PAX which would add genuine new information on the spin dependence of the interaction and help to pin down parameters of phenomenological $\bar{N}N$ models. This part of the program will start with the polarized fixed-target experiments with polarized antiprotons in CSR (Phase–I) and can be extended to Phase–II.

Besides, available data on the analyzing power from LEAR will be used for polarimetry to obtain information on the target and beam polarization, independent from the polarimeter foreseen for the polarized target (cf. Sec. 11).

Part II
Polarized Antiprotons at FAIR

7 Overview

A viable practical scheme which allows us to reach a polarization of the stored antiprotons at HESR–FAIR of $\simeq 0.3$ has been worked out and published in Ref. [123]. The basic approach to polarizing and storing antiprotons at HESR–FAIR is based on solid QED calculations of the spin transfer from electrons to antiprotons [124, 125], which is being routinely used at Jefferson Laboratory for the electromagnetic form factor separation [126], and which has been tested and confirmed experimentally in the FILTEX experiment [121].

The PAX Letter–of–Intent was submitted on January 15, 2004. The physics program of PAX has been reviewed by the QCD Program Advisory Committee (PAC) on May 14–16, 2004 [127]. The proposal by the ASSIA collaboration [128] to utilize a polarized solid target and to bombard it with a 45 GeV unpolarized antiproton beam extracted from the synchrotron SIS100 has been rejected by the GSI management. Such measurements would not allow one to determine $h_1^q(x, Q^2)$, because in single spin measurements $h_1^q(x, Q^2)$ appears always coupled to another unknown fragmentation function. Following the QCD–PAC report and the recommendation of the Chairman of the committee on Scientific and Technological Issues (STI) and the FAIR project coordinator [127], the PAX collaboration has optimized the technique to achieve a sizable antiproton polarization and is presenting here an updated proposal for experiments at GSI with polarized antiprotons [123]. From various working group meetings of the PAX collaboration, presented in part in 2004 at several workshops and conferences [127], we conclude:

- Polarization buildup in the HESR ring, operated at the lowest possible energy, as discussed in PAX LoI, does not allow one to achieve the optimum degree of polarization in the antiproton beam. The goal of achieving the highest possible polarization of antiprotons and optimization of the figure of merit dictates that one polarizes antiprotons in a dedicated low–energy ring (APR). The transfer of polarized low–energy antiprotons into the HESR ring requires pre–acceleration to about 1.5 GeV/c in a dedicated booster ring (CSR). Simultaneously, the incorporation of this booster ring into the HESR complex opens up, quite naturally, the possibility of building an asymmetric antiproton–proton collider.

The PAX collaboration proposes an approach that is composed of two phases. During these the major milestones of the project can be tested and optimized before the final goal is approached: **An asymmetric proton–antiproton collider**, in which polarized protons with momenta of about 3.5 GeV/c collide with polarized antiprotons with momenta up to 15 GeV/c. These circulate in the HESR, which has already been approved and will serve the PANDA experiment. In the following, we will briefly describe the overall machine setup of the APR, CSR, and HESR complex, schematically depicted in Fig. 9. The main

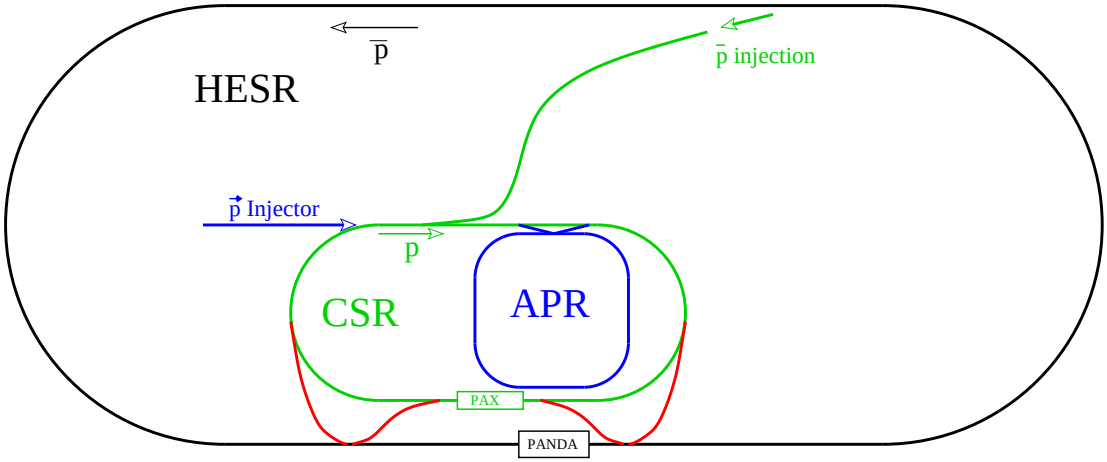

Figure 9: The proposed accelerator set–up at the HESR (black), with the equipment used by the PAX collaboration in Phase–I: CSR (green), APR, beam transfer lines and polarized proton injector (all blue). In Phase–II, by adding two transfer lines (red), an asymmetric collider is set up. It should be noted that, in this phase, also fixed target operation at PAX is possible. (The figure is drawn to scale.)

features of the accelerator setup are:

1. An Antiproton Polarizer Ring (APR) built inside the HESR area with the crucial goal of polarizing antiprotons at kinetic energies around ≈ 50 MeV ($p \approx 300$ MeV/c), to be accelerated and injected into the other rings.

2. A second Cooler Synchrotron Ring (CSR, COSY–like) in which protons or antiprotons can be stored with a momentum up to 3.5 GeV/c. This ring shall have a straight section, where a PAX detector could be installed, running parallel to the experimental straight section of HESR.

3. By deflection of the HESR beam into the straight section of the CSR, both the collider or the fixed–target mode become feasible.

It is worthwhile to stress that, through the employment of the CSR, effectively a second interaction point is formed with minimum interference with PANDA. The proposed solution opens the possibility to run two different experiments at the same time. In order to avoid unnecessary spin precession, all rings, ARP, CSR and HESR, should be at the same level such that no vertical deflection is required when injecting from one ring into the other.

In Sec. III, we discuss the staging of the physics program, which should be pursued in two phases.

8 Antiproton Polarizer Ring

For more than two decades, physicists have tried to produce beams of polarized antiprotons [129]. Conventional methods like atomic beam sources (ABS), appropriate for the production of polarized protons and heavy ions cannot be applied, since antiprotons annihilate with matter. Polarized antiprotons have been produced from the decay in flight of $\bar{\Lambda}$ hyperons at Fermilab. The achieved intensities with antiproton polarizations $P > 0.35$ never exceeded $1.5 \cdot 10^5$ s^{-1} [130]. Scattering of antiprotons off a liquid hydrogen target could yield polarizations of $P \approx 0.2$, with beam intensities of up to $2 \cdot 10^3$ s^{-1} [131]. Unfortunately, both approaches do not allow efficient accumulation in a storage ring, which would greatly enhance the luminosity. Spin splitting using the Stern–Gerlach separation of the given magnetic substates in a stored antiproton beam was proposed in 1985 [132]. Although the theoretical understanding has much improved since then [133], spin splitting using a stored beam has yet to be observed experimentally.

8.1 The Polarizing Process $\bar{p} + \vec{e} \rightarrow \vec{\bar{p}} + e$

In 1992 an experiment at the Test Storage Ring (TSR) at MPI Heidelberg showed that an initially unpolarized stored 23 MeV proton beam can be polarized by spin–dependent interaction with a polarized hydrogen gas target [121, 134, 135]. In the presence of polarized protons of magnetic quantum number $m = \frac{1}{2}$ in the target, beam protons with $m = \frac{1}{2}$ are scattered less often, than those with $m = -\frac{1}{2}$, which eventually caused the stored beam to acquire a polarization parallel to the proton spin of the hydrogen atoms during spin filtering.

In an analysis by Meyer three different mechanisms were identified, that add up to the measured result [124]. One of these mechanisms is spin transfer from the polarized electrons of the hydrogen gas target to the circulating protons. Horowitz and Meyer derived the spin transfer cross section $p + \vec{e} \rightarrow \vec{p} + e$ (using $c = \hbar = 1$) [125],

$$\sigma_{e_{||}} = -\frac{4\pi\alpha^2(1+a)m_e}{p^2 m_p} \cdot C_0^2 \cdot \frac{v}{2\alpha} \cdot \sin\left(\frac{2\alpha}{v}\ln(2pa_0)\right) , \tag{13}$$

where α is the fine–structure constant, $a = \frac{g-2}{2} = 1.793$ is the anomalous magnetic moment of the proton, m_e and m_p are the rest mass of electron and proton, p is the momentum in the CM system, $a_0 = 52900$ fm is the Bohr radius and $C_0^2 = 2\pi\eta/[\exp(2\pi\eta) - 1]$ is the square of the Coulomb wave function at the origin. The Coulomb parameter η is given by $\eta = -z\alpha/v$ (for antiprotons, η is positive). z is the beam charge number and v the relative velocity of particle and projectile. In Fig. 10 the spin transfer cross section $\sigma_{e_{||}}$ of antiprotons scattered from longitudinally polarized electrons is plotted versus the beam kinetic energy T.

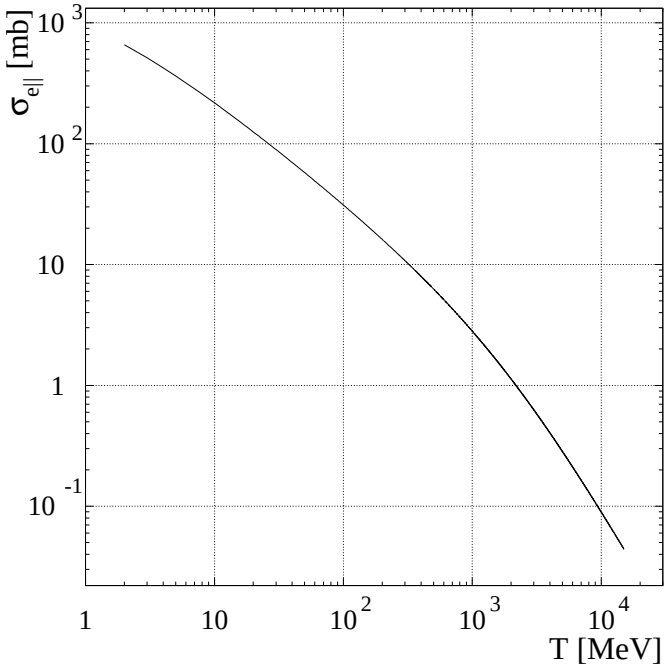

Figure 10: Spin transfer cross section $\sigma_{e_{||}}$ of antiprotons scattered from longitudinally polarized electrons ($\bar{p} + \vec{e} \rightarrow \vec{\bar{p}} + e$) as a function of the kinetic energy of the antiprotons.

8.2 Design Consideration for the APR

In the following we evaluate a concept for a dedicated antiproton polarizer ring (APR). Antiprotons would be polarized by the spin–dependent interaction in an electron–polarized hydrogen gas target. This spin–transfer process is *calculable*, whereas, due to the absence of polarized antiproton beams in the past, a measurement of the spin–dependent $\bar{p}p$ interaction is still lacking, and only theoretical models exist [136]. The polarized antiprotons would be subsequently transferred to the HESR for measurements (Fig. 9).

Both the APR and the HESR should be operated as synchrotrons with beam cooling to counteract emittance growth. In both rings the beam polarization should be preserved during acceleration without loss [137]. The longitudinal spin–transfer cross section is twice as large as the transverse one [124], $\sigma_{e_\parallel} = 2 \cdot \sigma_{e_\perp}$, the stable spin direction of the beam at the location of the polarizing target should therefore be longitudinal as well, which requires a Siberian snake in a straight section opposite the polarizing target [138].

8.2.1 Polarizer Target

A hydrogen gas target of suitable substate population represents a dense target of quasi–free electrons of high polarization and areal density. Such a target can be produced by

injection of two hyperfine states with magnetic quantum numbers $|m_J = +\frac{1}{2}, m_I = +\frac{1}{2}\rangle$ and $|+\frac{1}{2}, -\frac{1}{2}\rangle$ into a strong longitudinal magnetic holding field of about $B_{||} = 300$ mT (Fig. 11). The maximum electron and nuclear target polarizations in such a field are

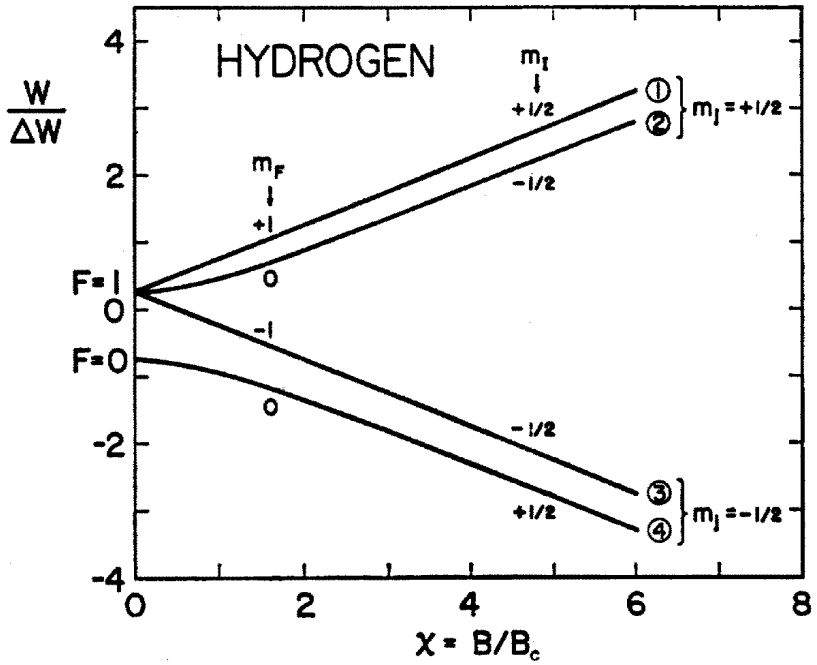

Figure 11: Breit–Rabi diagram of hydrogen atoms in units of $\Delta W = h \times 1420.4$ MHz [139]. The magnetic field is given in units of $\chi = B/B_c$. The critical field for the ground state of hydrogen is $B_c = 50.7$ mT.

$Q_e = 0.5 \cdot (1 + \chi/\sqrt{1+\chi^2}) = 0.993$ and $Q_z = 0.5 \cdot (1 - \chi/\sqrt{1+\chi^2}) = 0.007$ [139], where $\chi = B_{||}/B_c$ and $B_c = 50.7$ mT. Polarized atomic beam sources presently produce a flux of hydrogen atoms of about $q = 1.2 \cdot 10^{17}$ atoms/s in two hyperfine states [140]. Our model calculation for the polarization buildup assumes a moderate improvement of 20%, i.e. a flow of $q = 1.5 \cdot 10^{17}$ atoms/s.

8.2.2 Beam Lifetime in the APR

The beam lifetime in the APR can be expressed as function of the Coulomb–loss cross section $\Delta\sigma_C$ and the total hadronic $\bar{p}p$ cross section $\sigma_{\rm tot}$,

$$\tau_{\rm APR} = \frac{1}{(\Delta\sigma_C + \sigma_{\rm tot}) \cdot d_t \cdot f_{\rm APR}} \,. \tag{14}$$

The density d_t of a storage cell target depends on the flow of atoms q into the feeding tube of the cell, its length along the beam $L_{\rm beam}$, and the total conductance $C_{\rm tot}$ of the storage cell $d_t = \frac{1}{2}\frac{L_{\rm beam} \cdot q}{C_{\rm tot}}$ [141]. The conductance of a cylindrical tube $C_\circ$ for a gas of

circumference of APR	$L_{\rm APR}$	150 m
β–function at target	β	0.2 m
radius of vacuum chamber	r	5 cm
gap height of magnets	$2\,g$	14 cm
ABS flow into feeding tube	q	$1.5 \cdot 10^{17}$ atoms/s
storage cell length	$L_{\rm beam}$	40 cm
feeding tube diameter	$d_{\rm feed}$	1 cm
feeding tube length	$L_{\rm feed}$	15 cm
longitudinal holding field	$B_{\vert\vert}$	300 mT
electron polarization	Q_e	0.9
cell temperature	T	100 K

Table 2: Parameters of the APR and the polarizing target section.

mass M in the regime of molecular flow (mean free path large compared to the dimensions of the tube) as function of its length L, diameter d, and temperature T, is given by $C_\circ = 3.8 \cdot \sqrt{\frac{T}{M}} \cdot \frac{d^3}{L+\frac{4}{3}\cdot d}$. The total conductance $C_{\rm tot}$ of the storage cell is given by $C_{\rm tot} = C_\circ^{\rm feed} + 2 \cdot C_\circ^{\rm beam}$, where $C_\circ^{\rm feed}$ denotes the conductance of the feeding tube and $C_\circ^{\rm beam}$ the conductance of one half of the beam tube. The diameter of the beam tube of the storage cell should match the ring acceptance angle $\Psi_{\rm acc}$ at the target, $d_{\rm beam} = 2 \cdot \Psi_{\rm acc} \cdot \beta$, where for the β–function at the target, we use $\beta = \frac{1}{2}\, L_{\rm beam}$. One can express the target density in terms of the ring acceptance, $d_t \equiv d_t(\Psi_{\rm acc})$, where the other parameters used in the calculation are listed in Table 2.

The Coulomb–loss cross section $\Delta\sigma_C$ (using $c = \hbar = 1$) can be derived analytically in terms of the square of the total energy s by integration of the Rutherford cross section, taking into account that only those particles are lost that undergo scattering at angles larger than $\Psi_{\rm acc}$,

$$\Delta\sigma_C(\Psi_{\rm acc}) = 4\pi\alpha^2 \frac{(s-2m_{\bar p}^2)^2\, 4m_{\bar p}^2}{s^2(s-4m_{\bar p}^2)^2} \left(\frac{1}{\Psi_{\rm acc}^2} - \frac{s}{4m_{\bar p}^2}\right) . \tag{15}$$

The total hadronic cross section is parameterized using a function inversely proportional to the Lorentz parameter $\beta_{\rm lab}$. Based on the $\bar p p$ data [142] the parameterization $\sigma_{\rm tot} = \frac{75.5}{\beta_{\rm lab}}$ (mb) yields a description of $\sigma_{\rm tot}$ with $\approx 15\%$ accuracy up to $T \approx 1000$ MeV. The APR revolution frequency is given by

$$f_{\rm APR} = \frac{\beta_{\rm lab} \cdot c}{L_{\rm APR}} . \tag{16}$$

The resulting beam lifetime in the APR as function of the kinetic energy T is depicted in Fig. 12 for different acceptance angles $\Psi_{\rm acc}$.

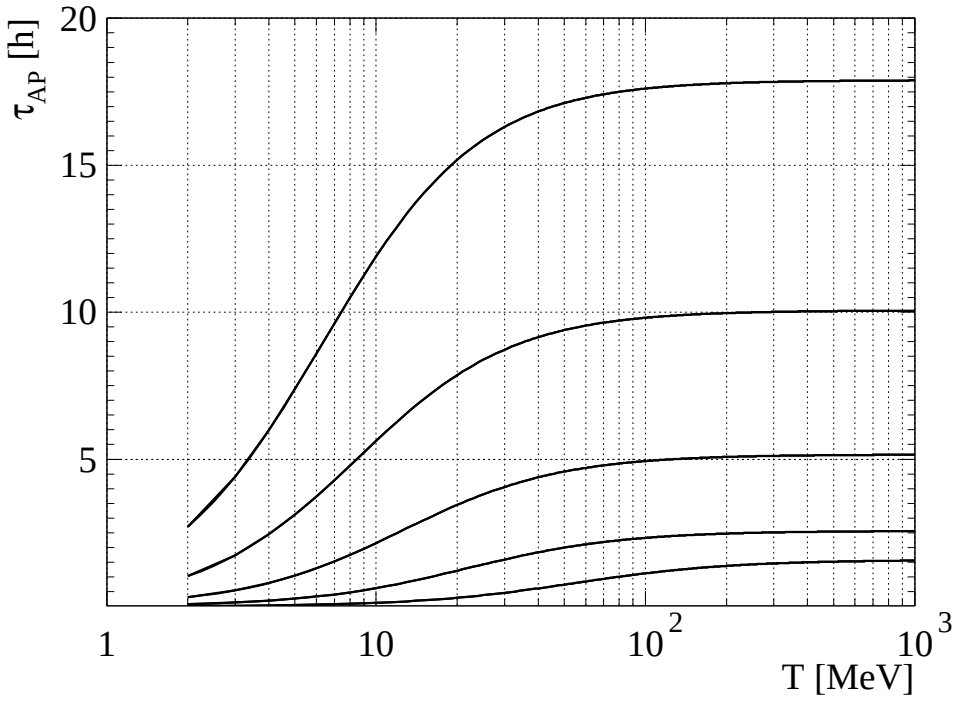

Figure 12: Beam lifetime in the APR as function of kinetic energy T. From top to bottom the lines denote $\Psi_{\mathrm{acc}} = 50$, 40, 30, 20, and 10 mrad.

8.3 Polarization Buildup

The buildup of polarization due to the spin–dependent $\bar{p}e$ interaction in the target [Eq. (13)] as function of time t is described by

$$P(t) = \tanh\left(\frac{t}{\tau_p}\right) \text{ , where } \tau_p = \frac{1}{\sigma_{e_\parallel}\, d_t\, f_{\mathrm{APR}}\, Q_e} \tag{17}$$

denotes the polarization buildup time. The time dependence of the beam intensity is described by

$$I(t) = I_0 \cdot \exp\left(-\frac{t}{\tau_{\mathrm{APR}}}\right) \cdot \cosh\left(\frac{t}{\tau_p}\right) , \tag{18}$$

where $I_0 = N_{\bar{p}}^{\mathrm{APR}} \cdot f_{\mathrm{APR}}$. The quality of the polarized antiproton beam can be expressed in terms of the figure of merit [143]

$$\mathrm{FOM}(t) = P(t)^2 \cdot I(t) \, . \tag{19}$$

The optimum interaction time t_{opt}, where $\mathrm{FOM}(t)$ reaches the maximum, is given by $\frac{\mathrm{d}}{\mathrm{d}t}\mathrm{FOM}(t) = 0$. For the situation discussed here, $t_{\mathrm{opt}} = 2 \cdot \tau_{\mathrm{APR}}$ constitutes a good approximation that deviates from the true values by at most 3%. The magnitude of the antiproton

beam polarization $P(t_{\rm opt})$ based on electron spin transfer [Eq. (17)] is depicted in Fig. 13 as function of beam energy T for different acceptance angles $\Psi_{\rm acc}$.

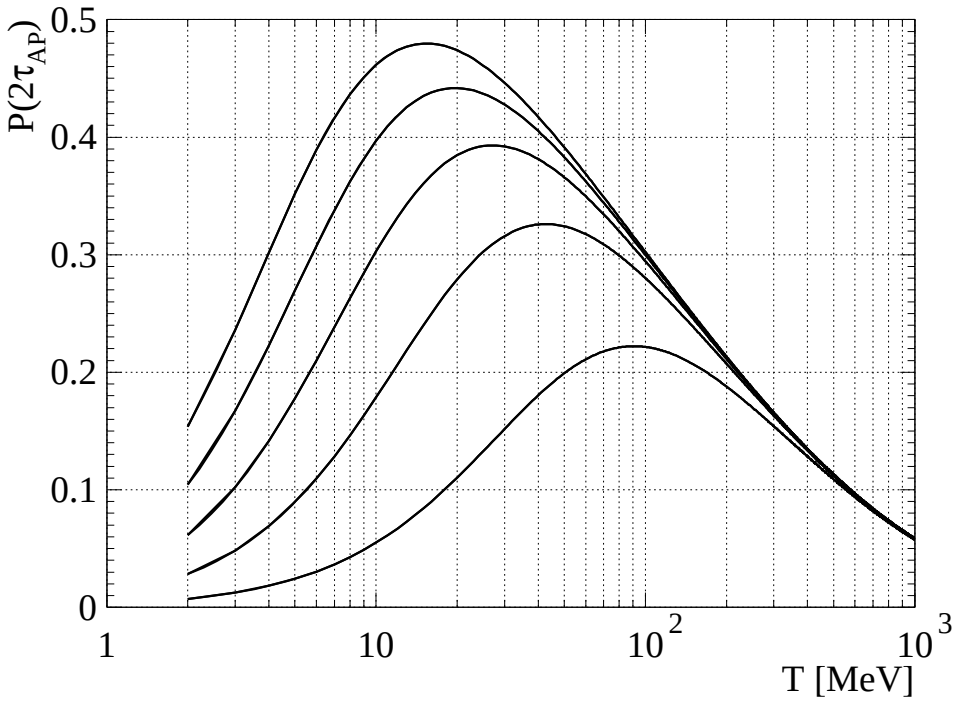

Figure 13: Antiproton beam polarization $P(2\cdot\tau_{\rm APR})$ [Eq. (17)] as function of beam energy for different acceptance angles $\Psi_{\rm acc}$. (Lines are organized as in Fig. 12.)

8.3.1 Space–Charge Limitations

The number of antiprotons stored in the APR may be limited by space–charge effects. With an antiproton production rate of $R = 10^7\ \bar{p}/s$, the number of antiprotons available at the beginning of the filtering procedure corresponds to

$$N_{\bar{p}}^{\rm APR}(t=0) = R \cdot 2 \cdot \tau_{\rm APR}\ . \tag{20}$$

The individual particle limit in the APR is given by [144]

$$N_{\rm ind.} = 2\,\pi\,\varepsilon\,\beta_{\rm lab}^2\,\gamma_{\rm lab}^3\,(r_p\,F)^{-1}\,\Delta Q\ , \tag{21}$$

where $\varepsilon = \Psi_{\rm acc}^2 \cdot \beta$ denotes the vertical and horizontal beam emittance, $\beta_{\rm lab}$ and $\gamma_{\rm lab}$ are the Lorentz parameters, $r_p = 1.5347 \cdot 10^{-18}$ m is the classical proton radius, and $\Delta Q = 0.01$ is the allowed incoherent tune spread. The form factor F for a circular vacuum chamber [144] is given by $F = 1 + \left(a_y \cdot \frac{a_x + a_y}{r^2}\right) \cdot \varepsilon_2 \cdot (\gamma_{\rm lab}^2 - 1) \cdot \frac{r^2}{g^2}$, where the mean semi–minor horizontal (x) and vertical (y) beam axes $a_{x,y} = \sqrt{\varepsilon \cdot \beta_{x,y}}$ are calculated from the mean horizontal

and vertical β–functions $\beta_{x,y} = L_{\mathrm{APR}} \cdot (2\pi\nu)^{-1}$ for a betatron–tune $\nu = 3.6$. For a circular vacuum chamber and straight magnet pole pieces the image force coefficient $\varepsilon_2 = 0.411$. The parameter r denotes the radius of the vacuum chamber and g half of the height of the magnet gaps (Table 2). In Fig. 14 the individual particle limit is plotted for the different acceptance angles.

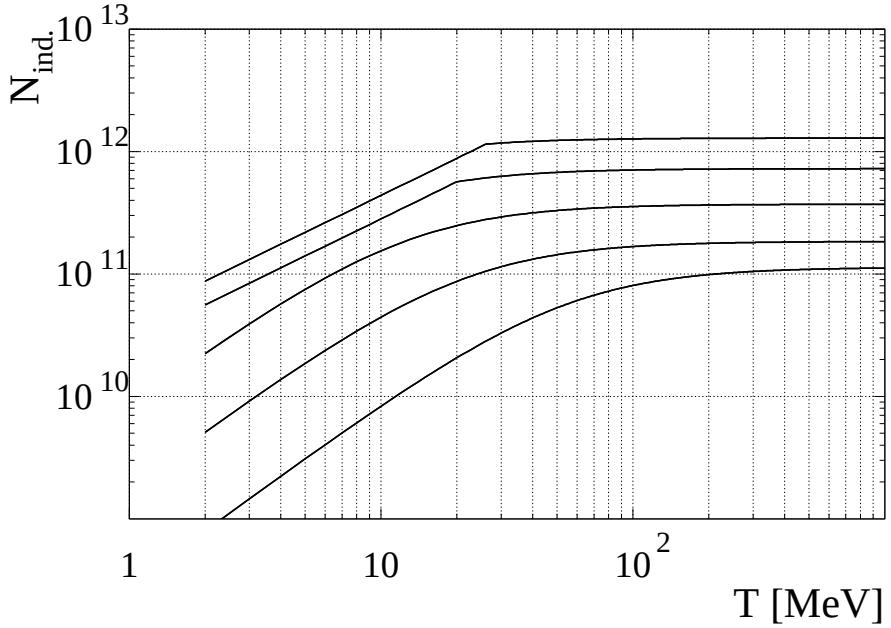

Figure 14: Individual particle limit $N_{\mathrm{ind.}}$ for the five different ring acceptance angles Ψ_{acc} (50 – 10 mrad) as function of beam energy. (Lines are organized as in Fig. 12.)

8.3.2 Optimum Beam Energies for the Polarization Buildup

The optimum beam energies for different acceptance angles at which the polarization buildup works best, however, cannot be obtained from the maxima in Fig. 13. In order to find these energies, one has to evaluate at which beam energies the FOM [Eq. (19)], depicted in Fig. 15, reaches a maximum. The optimum beam energies for polarization buildup in the APR are listed in Table 3. The limitations due to space–charge, $N_{\bar{p}}^{\mathrm{APR}} > N_{\mathrm{ind.}}$ [Eqs. (20, 21)], are visible as kinks in Fig. 15 for the acceptance angles $\Psi_{\mathrm{acc}} = 40$ and 50 mrad, however, the optimum energies are not affected by space–charge.

8.3.3 Polarized Targets containing only Electrons

Spin filtering in a *pure* electron target greatly reduces the beam losses, because σ_{tot} disappears and Coulomb scattering angles in $\bar{p}e$ collisions do not exceed Ψ_{acc} of any stor-

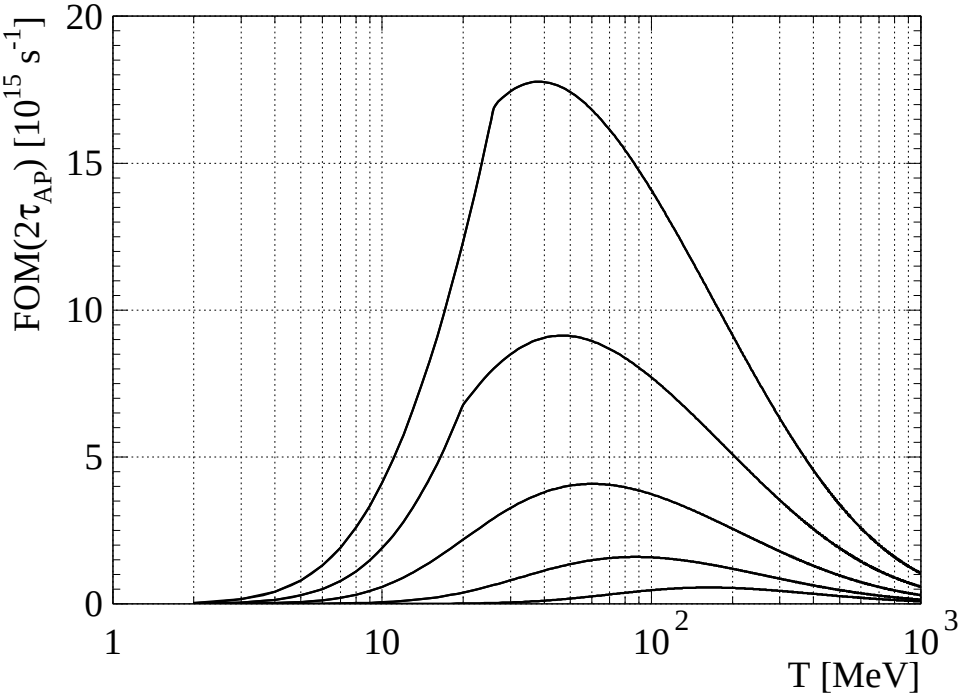

Figure 15: Figure of Merit for the polarized antiproton beam for filtering times $t = 2 \cdot \tau_{\mathrm{APR}}$ as function of beam energy. The parameters associated with the maxima are summarized in Table 3. (Lines are organized as in Fig. 12.)

age ring. With stationary electrons stored in a Penning trap, areal densities of about 10^{12} electrons/cm^2 may be reached in the future [145]. A typical electron cooler operated at 10 kV with polarized electrons of intensity ≈ 1 mA ($I_e \approx 6.2 \cdot 10^{15}$ electrons/s) [146], $A = 1$ cm^2 cross section, and $l = 5$ m length reaches $d_t = I_e \cdot l \cdot (\beta_{\mathrm{lab}}\, c\, A)^{-1} = 5.2 \cdot 10^8$ electrons/cm^2, which is six orders of magnitude short of the electron densities achievable with a neutral hydrogen gas target. For a pure electron target the spin transfer cross section is $\sigma_{e_{||}} = 670$ mb (at $T = 6.2$ MeV) [125], about a factor 15 larger than the cross sections associated to the optimum energies using a gas target (Table 3). One can therefore conclude that with present day technologies, both above discussed alternatives are no match for spin filtering using a polarized gas target.

8.4 Luminosity Estimate for a Fixed Target in the HESR

In order to estimate the luminosities, we use the parameters of the HESR ($L_{\mathrm{HESR}} = 440$ m). After spin filtering in the APR for $t_{\mathrm{opt}} = 2 \cdot \tau_{\mathrm{APR}}$, the number of polarized antiprotons transfered to HESR is $N_{\bar{p}}^{\mathrm{APR}}(t = 0)/e^2$ [Eq. (20)]. The beam lifetime in the HESR at $T = 15$ GeV for an internal polarized hydrogen gas target of $d_t = 7 \cdot 10^{14}$ cm^{-2} is about $\tau_{\mathrm{HESR}} = 12$ h [Eqs. (14, 16)], where the target parameters from Table 2 were used, a cell

$\Psi_{\rm acc}$ (mrad)	T (MeV)	$\tau_{\rm APR}$ (h)	$P(2\,\tau_{\rm APR})$
10	167	1.2	0.19
20	88	2.2	0.29
30	61	4.6	0.35
40	47	9.2	0.39
50	39	16.7	0.42

Table 3: Kinetic beam energies where the polarized antiproton beam in the APR reaches the maximum FOM for different acceptance angles.

diameter $d_{\rm beam} = 0.8$ cm, and $\sigma_{\rm tot} = 50$ mb. Subsequent transfers from the APR to the HESR can be employed to accumulate antiprotons. Eventually, since $\tau_{\rm HESR}$ is finite, the average number of antiprotons reaches equilibrium, $\overline{N_{\bar{p}}^{\rm HESR}} = R/e^2 \cdot \tau_{\rm HESR} = 5.6 \cdot 10^{10}$, independent of $\tau_{\rm APR}$. An average luminosity of $\bar{\mathcal{L}} = R/(e^2 \cdot \sigma_{\rm tot}) = 2.7 \cdot 10^{31}$ cm^{-2}s^{-1} can be achieved, with antiproton beam polarizations depending on the APR acceptance angle $\Psi_{\rm acc}$ (Table 3).

To summarize, we have shown that with a dedicated large acceptance antiproton polarizer ring ($\Psi_{\rm acc} = 10$ to 50 mrad), beam polarizations of $P = 0.2$ to 0.4 could be reached. The energies at which the polarization buildup works best range from $T = 40$ to 170 MeV. In equilibrium, the average luminosity for double–polarization experiments in an experimental storage ring (e.g. HESR) after subsequent transfers from the APR could reach $\bar{\mathcal{L}} = 2.7 \cdot 10^{31}$ cm^{-2}s^{-1}.

8.5 Technical Realization of the APR

Antiprotons are conveniently polarized at an energy of ≈ 50 MeV ($\beta_c = 0.28$) with an adequate gas target [141]. A storage ring is ideal to efficiently achieve a high degree of beam polarization due to the repeated beam traversal of the target. The beam degradation, the geometrical blow–up, and the subsequent smearing of the beam energy needs to be corrected by phase–space cooling, preferably by electron cooling. The shaking of the beam [147], leading to unwanted instabilities caused by positive ions accumulated around the beam, can be eliminated by a suitable RF cavity. Since the antiprotons should be longitudinally polarized, the ring has to contain a Siberian snake [138]. Finally efficient systems for injection and extraction of the antiproton beam have to be provided in the ring as well. The consequences of these insertions are at first, sufficient space in the ring and secondly, various specifications of the antiproton beam at the positions of these insertions, i.e. constraints on the ion–optical parameters. Obviously, for a high antiproton polarization, the divergence of the beam at the polarizer target should be large. The antiproton beam will be injected by stacking in phase space. The extraction will be done by bunch–to–bunch transfer. In the empty ring, the antiproton beam lifetime should be a several tens of hours, which sets also the requirements for the vacuum system.

The antiproton polarizer, discussed here, would provide highly polarized antiproton

beams of unprecedented quality. In particular the implementation of this option at the Facility for Antiproton and Ion Research would open new and unique research opportunities for spin–physics experiments in $\bar{p}p$ interactions at the HESR and CSR.

8.5.1 Constraints

Following the known requests, we describe here a design for such a ring. Four straight sections are required for the following insertions:

1. Injection and extraction of the antiproton beam, for which free space of 4 m is foreseen.
2. For the gas target a low β–section is required in order to obtain a small beam spot and a large angular divergence, in this straight section a free space of 1 m is provided.
3. The opposite straight section should be reserved for the Siberian snake to longitudinally align the antiproton spin.
4. For electron cooling, in the straight section opposite to the injection straight, a free space of 4 m is reserved.
5. A small RF cavity may be provided in any section.

Various ion optical conditions have to be met in the four straight sections:

A) In the target, e-cooler, and the Siberian snake sections the beam cross section has to be circular and the beams phase space ellipse has to be upright.

B) In all straight sections the dispersion should be zero.

C) The antiproton beam in the e-cooling section should be parallel and its cross section should be variable in order to match the size of the electron beam.

D) The radius of the beam spot at the target should be ≈ 10 mm.

The present APR is designed for antiprotons of 40 MeV, corresponding to a momentum of $p = 276$ MeV/c and a magnetic rigidity of $B\rho = 0.924$ Tm. Finally a large acceptance of the APR is required. We have anticipated an acceptance of the ring of

$$\epsilon_{x,y} = 500\,\pi\text{mm mrad}\,, \tag{22}$$

sufficient to accommodate a flux of at least 10^{11} $\bar{p}$/s.

To provide longitudinal polarized beam at the position of the storage cell, an integrated field strength of roughly 1.2 Tm is required in the opposite straight section of the APR (1.15 (1.04) Tm for 50 (40) MeV). Two scenarios are possible in combination with the solenoids of the electron cooler. The electron cooler is located in a different straight section than

the snake. In this case correcting solenoids should be utilized to compensate for spin motion in the main solenoid of the cooling system. One could also apply the electron cooler solenoids as a snake. The integrated field of a conventional electron cooler, like the one in use at COSY is about 0.15 T with an effective length of 2m. Together with two compensation solenoids, this would provide a half–snake at APR energies. An additional solenoid of 0.6 Tm would then be sufficient to achieve the required integrated field. All solenoids would have to be in the same straight section, opposite to the storage cell. Only the additional solenoid would have to be rampable. For beam extraction and transfer, the beam should be vertically polarized. Therefore the snake has to be either adiabatically turned off (first solution) or ramped to opposite field strength (second solution) in order to compensate for the cooler solenoids. In both cases, depolarizing resonances can be crossed during ramping, since the spin tune moves from half integer for a full snake to $\gamma G = 1.88$. If the fractional betatron tune in the APR is chosen to be larger than 0.83 or smaller than 0.17, no first order resonances are crossed. If this should not be possible, the ramping speed of the snake has to be chosen in such a way as to minimize polarization losses during spin resonance crossing.

8.5.2 Layout of the APR Lattice

The optical condition A, outlined above, leads to the utilization of symmetric quadrupole triplets. Thus for the arcs of the APR ring design, where the beam is bent by 90 degrees, the following structure has been chosen:

$$\text{Triplet } 1 - \text{Bend}(45^\circ) - \text{Triplet } 2 - \text{Bend}(45^\circ) - \text{Triplet } 1 \tag{23}$$

In detail, denoting with F and D the focusing and defocusing strengths of the quadrupoles, the 2 triplets are realized by:

$$\text{Triplet } 1 = \text{D} - \text{F} - \text{D} \text{ and Triplet } 2 = \text{F} - \text{D} - \text{F} \tag{24}$$

For each of the four straight sections two triplets are foreseen to meet the ion–optical conditions mentioned above. For three straight sections two quadrupole doublets are needed in addition to provide the requested beam sizes and divergences, e.g. the low β–section around the gas target. The ion–optical imaging through each arc is telescopic, or more accurately, it constitutes a (-1)– telescope. In Fig. 16 a floor plan of the suggested APR is shown, which could be realized within a floor space of 30×30 m^2. The main parameters of the ring lattice are contained in Table 4. The important specifications for the dipole and quadrupole magnets are listed in Table 5 for the case of realizing the magnets conventionally by water–cooled electromagnets. In sec. 8.5.5 an economic solution based on permanent magnets is discussed.

8.5.3 Features of the APR Design

For the layout of the APR, the computer code WinAgile [148] has been used. In the following, we discuss the most important optical transfer functions. From the β–functions

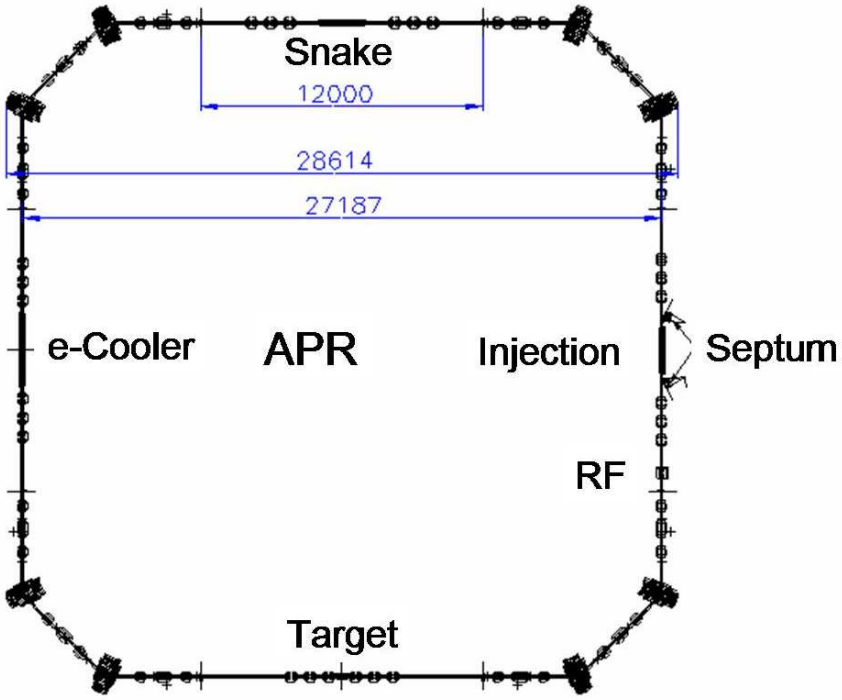

Figure 16: Floor plan of the APR lattice.

$\beta_{x,y}$, the radius of the corresponding beam size (r_x, r_y) is readily obtained from the relation

$$(r_x, r_y) = \sqrt{\beta_{x,y} \cdot \epsilon_{x,y}} \,, \tag{25}$$

where $\epsilon_{x,y}$ denote the horizontal and vertical phase space, respectively.

In Fig. 17 the radius of the beam spot is shown for one of the four arcs of the present APR design. The large phase space of the beam leads to large sizes of the gaps and diameters of the dipole magnets and quadrupoles, as listed in Table 5. The beam envelopes in the target section are shown in Fig 18, where a spot size of $r = 10$ mm is required together with an angular divergence of 50 mrad. The phase space ellipse of the beam here is upright $(\alpha_{x,y} = 0)$.

In Fig. 19, the β–functions for the straight section provided for the electron cooling solenoid. Here $\beta_x = \beta_y = 5$ m. Depending on the cross section of the electron beam $\beta_{x,y}$ can be adjusted to values between 1 and 10 m. For the last section with Siberian snake and RF cavity, a wide variety of optical conditions may be realized with the foreseen quadrupoles. The same applies to the injection/ejection section.

8.5.4 Discussion of the APR Design

The APR lattice design presented here provides telescopic imaging through each of the 4 arcs of the ring. The quadrupole arrangements in the straight sections enable tuning

Periodicity	P	4	
Circumference	C	100.2	m
Floor area	F	30×30	m^2
Magnetic rigidity	$B\rho$	0.924	Tm
γ		1.043	
β	v/c	0.283	
Beam emittance	$\epsilon_{x,y}$	500	π mm mrad
Number of particles		10^{11}	
Number of straight sections		4	
Length of straight sections	$l_{\text{s.s.}}$	12	m
Number of arcs		4	
Length of arcs	l_a	13.05	m
Number of 45° dipole magnets		8	
Number of quadrupoles		72	
Length of electron cooler solenoid	$L_{\text{sol.}}$	3.2	m
Cavity length	L_{RF}	0.4	m
Injection	Septum—Kicker		
Extraction	Kicker—Septum		
Cavity type	Finemet		

Table 4: Main parameters of the APR lattice.

of the beam within a wide choice of optical conditions. Plausible assumptions about the dimensions of the insertions have been made. The design of these insertions depends on the final lattice, and can be easily modified.

8.5.5 Realization of the APR based on Permanent Magnets

An important aspect concerning the realization of the APR concerns the employed conventional electromagnets (dipoles and quadrupoles). Since all APR magnets are set to a specific magnetic field or field gradient, the use of permanent magnets is an advisable alternative. For magnetic quadrupoles, the optical quality achieved so far with permanent magnetic material is excellent. Their great advantage would be:

1. Compactness of the quadrupoles,
2. savings in operational and investment costs, and
3. simple installation (neither power nor cooling water required).

Dipole magnets			Quadrupole magnets		
8			72		
bending angle	45	deg.	aperture diameter	135.1/143.3	mm
edge angle	22.5	deg.	effective length	25/50	cm
arc length	0.725	m	gradient	$1.33 - 1.62$	T/m
gap height	143	mm	pole tip field	$0.19 - 0.22$	T
magnetic field	1	T	weight	220/440	kg
weight	7000	kg			

Table 5: Specifications of the electrically powered dipole and quadrupole magnets for the APR. Aperture diameter, effective length, and weight are given for the singlet and triplet quadrupole magnets.

A preliminary estimate for replacing the 72 conventional quadrupoles in this APR design with permanent ones leads to length reductions from 25 (50) cm to 10 (12) cm for the 2 families with a corresponding weight reduction from 220 (440) to 11 (31) kg. The reduced weight would also have profound implications for the support structure, alignment etc. The permanent quadrupole magnets would save operational power costs of 150 kW and the investment for water cooling. The design of dipoles with a specific bending strength employing permanent magnetic material is complicated, since they consist of an arrangement of circular slabs with appropriate spacing. A suitable design is under preparation and commercially available from the company UGS [149], which also offers the permanent magnet quadrupoles. Although details are not available at present, size and weight reductions for the dipoles are similar. The operation of the conventional dipoles would require a total power of 309 kW.

The antiproton polarizer, discussed here, would provide highly polarized antiproton beams of unprecedented quality. In particular the implementation of this option at the Facility for Antiproton and Ion Research would open new and unique research opportunities for spin–physics experiments in $\bar{p}p$ interactions at the HESR.

9 Cooler Synchrotron Ring CSR

The CSR has to accelerate polarized protons and antiprotons to momenta between 600 MeV/c and 3.65 GeV/c and is expected to be very similar to COSY [150]. A polarized ion source to provide a vector polarized proton beam is needed which is accelerated to about 50MeV before injection into the CSR [151, 152]. The polarization is determined by measuring the asymmetry of pC scattering from a carbon fiber target [153]. Additional polarimeters have to be installed after the LINAC to optimize the transition units in the polarized source for a high degree of polarization.

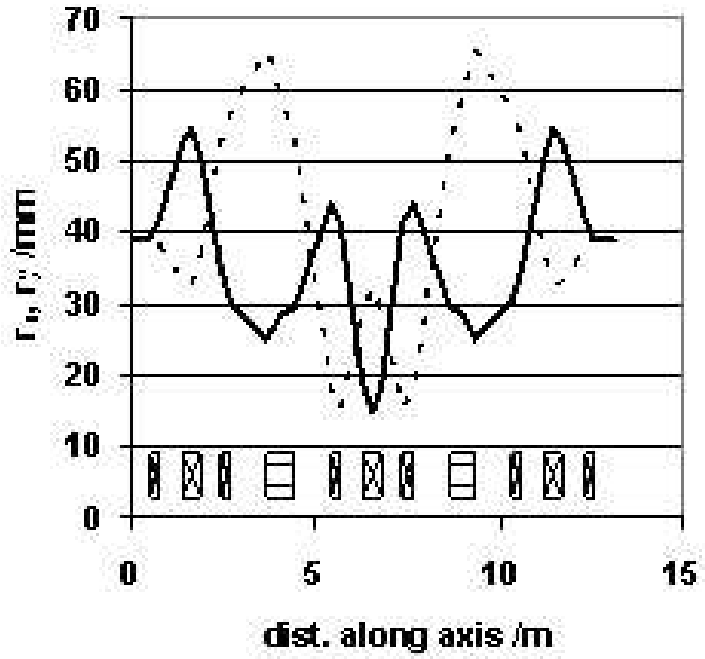

Figure 17: Beam radius (r_x, r_y) along one arc of the APR lattice (r_x – solid; r_y – dashed).

9.1 Injector LINAC for 50 MeV Polarized Protons

Low energy superconducting protons LINACs have been discussed recently as an optimum solution in terms of justifiable resources and available space. A layout for such a linac was worked out and proposed as a new injector for the COSY together with advanced ion sources and two interchangeable rf–quadrupole (RFQ). It was designed to deliver both polarized and unpolarized pulsed H^-/D^- beams at a kinetic energy of 50MeV with a maximum repetition rate of 2Hz. The pulse length was limited to 500 ms and the beam current to 2 mA (peak). This compact design leads to a total LINAC length of less than 20 m. For producing the short pulses of high–intensity polarized H^-/D^- beams, a CIPIOS–type ion source like the one used at IUCF (Bloomington, Indiana) is suitable [154].

It should be noted that after the termination of the HERA program in 2007, the DESY proton LINAC might be available, which would also be a perfect CSR injector.

9.2 Acceleration of Polarized Proton and Antiproton Beam

In a strong–focusing synchrotron like the CSR two different types of strong depolarizing resonances are excited, namely imperfection resonances caused by magnetic field errors and misalignments of the magnets, and intrinsic resonances excited by horizontal fields due to the vertical focusing. In the momentum range of CSR, five imperfection resonances have to be crossed. Vertical correction dipoles or a weak partial snake of a few percentage can

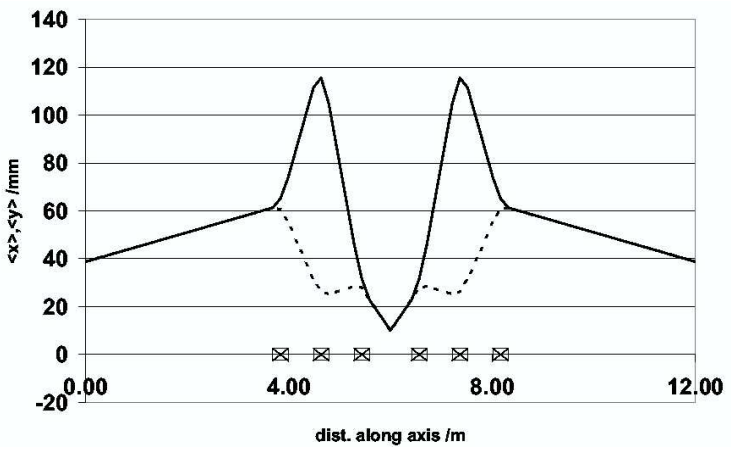

Figure 18: Beam radius (r_x, r_y) around the gas target (r_x – solid line, r_y – dashed).

be utilized to overcome all imperfection resonances by exciting adiabatic spin flips without polarization losses. The number of intrinsic resonances depends on the superperiodicity of the lattice. In principle a typical magnetic structure of a synchrotron ring in this energy range allows to adjust superperiodicities of $P = 2$ or even 6 like in COSY. However, due to symmetry–breaking modification of the interaction region and strong magnetic fields of detector magnets and the electron cooling system, a superperiodicity of $P = 1$ is expected, leading to about ten intrinsic resonances. A tune–jump system consisting of fast quadrupoles has especially been developed to handle intrinsic resonances at COSY and will also be suitable for the CSR.

9.2.1 Imperfection Resonances

The imperfection resonances for polarized protons and antiprotons are listed in Table 9.2.1. They are crossed during acceleration, if the number of spin precessions per revolution of the particles in the ring is an integer ($\gamma G = k$, k: integer). The resonance strength depends on the vertical closed orbit deviation. A solenoid with low magnetic field acting as a

γG	E_{kin} (MeV)	P (MeV/c)
2	108.4	463.8
3	631.8	1258.7
4	1155.1	1871.2
5	1678.5	2442.6
6	2201.8	2996.4

Table 6: Proton beam energies and momenta at which imperfection resonances occur in the CSR.

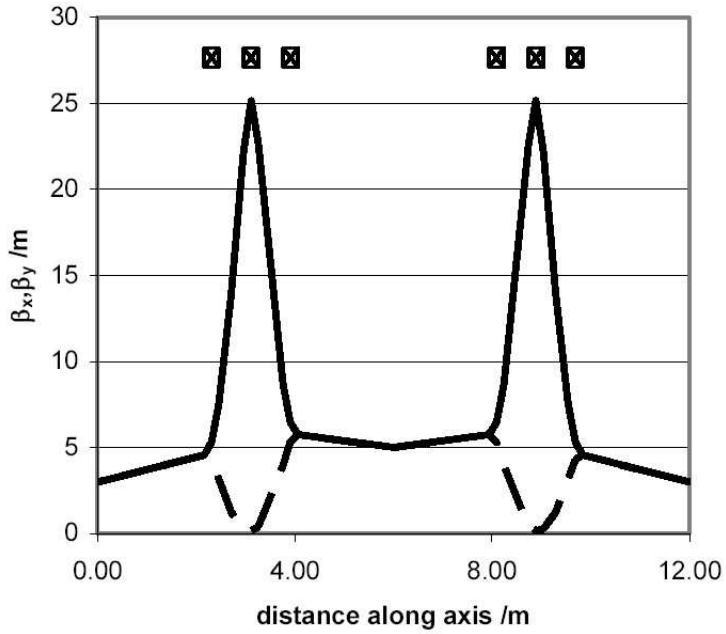

Figure 19: β–functions in the electron cooler section (β_x – solid line, β_y – dashed).

weak partial snake or vertical correction dipoles can be utilized in the CSR to preserve the polarization by exciting adiabatic spin flips. Both methods are successfully utilized in COSY and have to capability to overcome all imperfection resonances in the momentum range of the CSR.

9.2.2 Intrinsic Resonances

The number of intrinsic resonances depends on the superperiodicity P of the lattice, which is given by the number of identical periods in the accelerator. CSR will be a synchrotron with a racetrack design consisting of two 180° arc sections connected by straight sections. One straight section will be modified to allow interactions with the circulation beam in the HESR. In this case the superperiodicity of the ring will be one.

If the straight sections are tuned as telescopes with 1:1 imaging, giving a 2π betatron phase advance, one then obtains for the resonance condition $\gamma G = k \cdot P \pm (Q_y - 2)$, where k is an integer and Q_y is the vertical betatron tune. The corresponding intrinsic resonances in the momentum range of the CSR are listed in Table 9.2.2 for different superperiodicities P and a vertical betatron tune of $Q_y = 3.61$.

Intrinsic resonances in the CSR can be compensated by fast tune jumps with a similar system like in COSY. Due to symmetry–breaking installations like detector magnets and the arrangements for the interaction zone, the superperiodicity of the lattice is reduced to one, leading to ten intrinsic resonances. It has been proved that the tune–jump system of COSY can handle all ten intrinsic resonances in this momentum range. Therefore the same

P	γG	E_{kin} (MeV)	P (MeV/c)
1,2	$6 - Q_y$	312.4	826.9
1	$-1 + Q_y$	427.5	992.4
1	$7 - Q_y$	835.6	1505.3
1,2	$0 + Q_y$	950.7	1639.3
1,2,6	$8 - Q_y$	1358.8	2096.5
1	$1 + Q_y$	1473.9	2222.0
1	$9 - Q_y$	1882.0	2659.4
1,2	$2 + Q_y$	1997.1	2781.2
1,2	$10 - Q_y$	2405.2	3208.9
1	$3 + Q_y$	2520.3	3328.6

Table 7: Beam energy and momenta at which intrinsic resonances occur in the CSR for a working point $Q_y = 3.61$, and superperiodicities of $P = 1$, 2, and 6.

system is proposed for the CSR. Polarization measurements during acceleration confirm that the proposed concept allows the acceleration of a vertically polarized proton beam with polarization losses of only a few percent up to the maximum momentum of COSY. Therefore it is the ideal system for the CSR, which has very similar beam parameters.

10 PAX Requirements on the HESR Design

10.1 Introduction

For the Phase–II experimental program, polarized antiprotons stored in the HESR with energies up to 14.1 GeV are required. The APR–CSR system will provide antiprotons of up to 2.5 GeV. Therefore, polarized antiprotons have to be accelerated up to the highest HESR energies.

Instead of employing SIS 100 for acceleration, it appears to be much more economic to perform acceleration directly within the HESR. An efficient accumulation of polarized antiprotons in HESR, however, requires that at each cycle the remaining stack of polarized antiprotons is decelerated down to the injection energy and, after injection of additional antiprotons, is accelerated back to high energies.

Compared with the present HESR design [155], the following additional features are required:

- Acceleration using an rf–cavity,
- Slow ramping of the ring magnets,

- Stable spin during ramping and flat top by means of Siberian snakes,
- Spin manipulation of stored protons and antiprotons by means of rf–dipoles and solenoids,
- Injection of polarized antiprotons from CSR into the HESR, and
- Guiding the high–energy HESR beam to the PAX experiment in the CSR straight section by means of a chicane system.

10.2 Polarization Preservation

Acceleration and storage of polarized proton and antiproton beams in medium and high energy circular accelerator is complicated by numerous depolarizing spin resonances. In the following we discuss possible scenarios to accelerate and store polarized beams in the HESR.

The spin motion in an external electromagnetic field is governed by the so–called Thomas–BMT equation[156], leading to a spin tune of $\nu_{sp} = \gamma G$. [2] In a strong–focusing ring like the HESR imperfection and intrinsic spin resonances can depolarize the beam.

10.2.1 Depolarizing Resonances

In total 25 imperfection resonances ranging from $\gamma G = 4$ to 28, and 50 intrinsic resonances from $\gamma G = 16 - Q_y$ to $16 + Q_y$ for a vertical betatron tune of about $Q_y = 12.2$ have to be crossed during acceleration. The corresponding imperfection and intrinsic resonances in the momentum range of the HESR for a vertical working point of $Q_y = 12.14$ and superperiodicity $P = 1$ are listed in Table 8 The strength of the resonances depends on the orbit excursions for imperfection resonances and focusing structure of the lattice and beam emittance for intrinsic resonances and is ranging from 10^{-2} to 10^{-6} for the expected beam parameter. Due to coupling introduced by the 15 Tm solenoid of the Electron Cooler also strong coupling spin resonances are excited. The large number of resonances to be overcome in the HESR makes it very hard to apply techniques of individual manipulation of single spin resonances [157, 158, 159]. Siberian snakes seem to be to only option to guarantee a setup with low polarization losses during acceleration.

10.2.2 Siberian Snake with Combined Fields

In the HESR momentum range it is difficult use a RHIC–type [160] helical dipole snake due to large orbit excursions as shown in the upper left plot of Fig. 20. A solenoidal field would require a pretty high integrated field strength of roughly 60 Tm. Therefore a magnet system with a combination of both field types was investigated, consisting of four RHIC–type helical dipole magnets with a maximum field of 2.5 T and a 15 Tm solenoid (see upper

[2] G is the anomalous magnetic moment of the particle and $\gamma = E/m$ the Lorentz factor. The G–factor is quoted as 1.792847337(29) for protons, 1.800(8) for antiprotons [142].

$\gamma G = ...$	$\gamma G = ... \pm Q_y$	E_{kin} (GeV)	P (GeV/c)
	16-	1.082	1.789
4		1.155	1.871
	-8+	1.228	1.953
	17-	1.605	2.364
5		1.678	2.443
	-7+	1.752	2.521
	18-	2.129	2.920
6		2.202	2.997
	-6+	2.275	3.073
	19-	2.652	3.465
7		2.725	3.541
	-5+	2.798	3.617
	20-	3.175	4.005
8		3.248	4.080
...	...	...	...
	15+	13.265	14.172
	40-	13.642	14.550
28		13.715	14.624
	16+	13.789	14.697

Table 8: Beam energy and momenta at which imperfection and intrinsic resonances occur in the HESR for a working point of $Q_y = 12.14$.

right plot in the same Figure). To provide a full spin flip in the whole momentum range the snake magnets have to be ramped according to the values given in the lower left plot, where s is the solenoid and $d1, d2$ are the two helical dipole field values. The resulting spin motion at 15 GeV/c is shown in the lower right plot. This magnet system provides a full spin flip in the whole momentum range by keeping the maximum closed orbit excursion below 5 cm. Spin rotation induced by the DC Cooler solenoid at any possible field level can be compensated by the rampable 15 Tm snake solenoid, if snake and Cooler are installed in the same straight section.

10.2.3 Siberian Snake with Solenoidal Fields

The second proposed scheme contains four solenoids grouped on either side of the Cooler (see upper sketch of Fig. 21) with the same total integrated field strength of 15 Tm like the Cooler solenoid. From injection up to about 7.5 GeV/c all five solenoids will provide a full

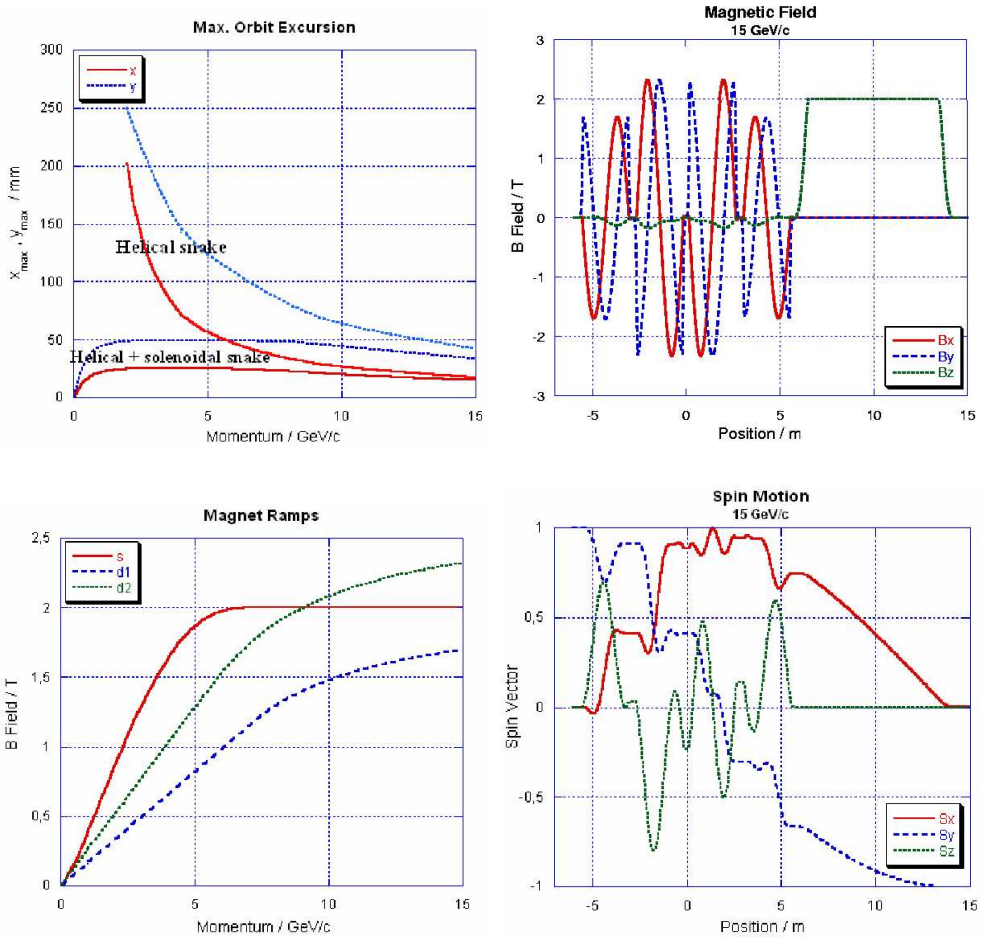

Figure 20: Layout of a full Siberian snake with combined helical dipole and solenoidal magnetic fields.

snake. At higher momenta they will work as partial snake with about 50% partial snake at top momentum. To compensate for coupling, two groups of four quadrupole magnets are needed with rotation angles up to 8.6, 6.3, 4.3 and 4.3 degree. The rotation angles of the quadrupoles have to be adjusted for different solenoid fields and beam momenta. The whole magnet insertion provides a betatron phase advance of π and 2π in the two transverse planes and has a total length of 56 m. To preserve polarization at first order spin resonances, the fractional part of the betatron tune has to be kept close to integer in the range $0.75 < Q_{frac} < 0.25$. This scheme does not excite orbit excursion and compensates for transverse phase space coupling. Applying higher integrated solenoidal field strength, it could also serve as a full Siberian snake.

The most serious drawback of a combined field scheme is large orbit excursion in the snake, which could be a major restriction for the beam quality in the HESR. Furthermore

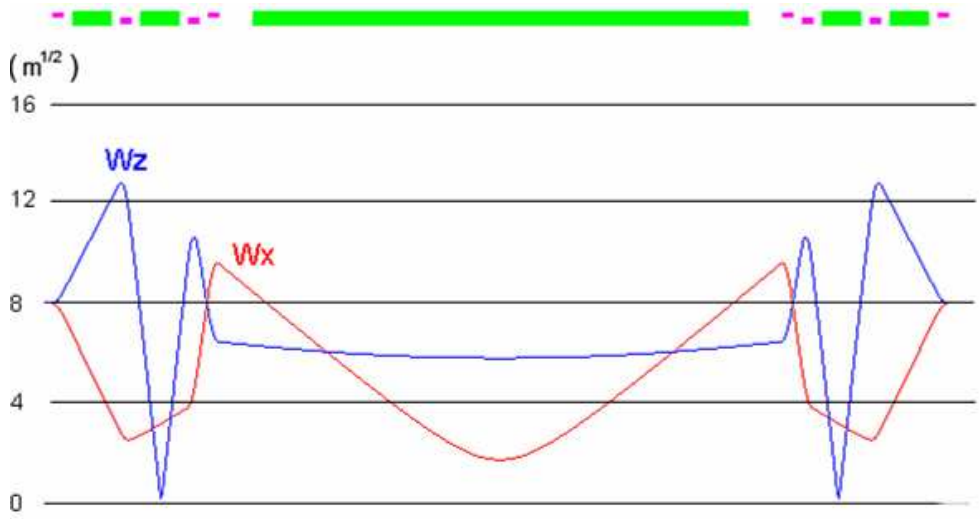

Figure 21: Layout of a Siberian snake with solenoidal fields (top) and optical functions (bottom).

rampability of the super–conducting snake magnets remains to be solved. Good field quality of the superconducting ring magnets is essential to apply a partial Siberian snake in order to keep the strength of higher–order spin resonances small combined with high flexibility of the lattice allowing for betatron tunes close to integer. A decision for one of the proposed schemes should be taken after intense particle and spin tracking including field errors and technical layout of the snake magnets.

10.3 Spin Manipulation of Polarized Protons and Antiprotons

Many polarized scattering experiments require frequent spin–direction reversals (spin–flips) during storage of the polarized beam to reduce their systematic errors. For maximum luminosity it is necessary to reverse the spins of the already stored antiprotons during the accumulation process, as was done in many IUCF experiments. Spin resonances induced by either an rf–solenoid or rf–dipole are well proven techniques to produce spin–flips in a controlled way. Spin flipping and spin manipulation of a stored beam was first studied in the IUCF Cooler Ring at 270 MeV [161]. In 2002, the SPIN@COSY collaboration was founded to continue these unique polarized beam studies in the GeV–regime at COSY [162]. Remarkably high measured proton spin–flip efficiencies of $99.92 \pm 0.04\%$ were achieved by ramping the frequency of a strong ferrite–core water–cooled RF dipole through an rf–induced spin resonance at 2.1GeV/c [163]. The weak energy dependence of the spin–resonance strength induced by transversal rf fields indicates that only a slightly stronger rf dipole should allow efficient spin–flips of polarized antiprotons up to the maximum energy of the HESR.

10.4 Interaction Region Design for the Asymmetric Collider

To maximize luminosity, both the proton and the antiproton beam need to be focused to small spot sizes at the interaction point (IP) of the facility. Both beams also have to be separated close to the IP into their respective storage rings. Though a crossing angle would greatly simplify the interaction region design, luminosity loss due to the relatively long bunches makes it less desirable. We have therefore designed an interaction region for head–on collisions, where beams are magnetically separated, taking advantage of the unequal beam energies.

Due to the hourglass effect, the finite bunch length of some 30 cm results in a minimum reasonable β–function at the IP of $\beta^* = 0.3\,\mathrm{m}$. With normalized emittances of $\epsilon_{p,n} = 1.7\pi\,\mu\mathrm{m}$ after cooling for the proton beam and $\epsilon_{\bar{p},n} = 20\pi\,\mu\mathrm{m}$ for the antiproton beam and the requirement of equal beam sizes of both beams at the interaction point to avoid emittance blow–up of the larger beam due to the beam–beam effect, resulting β–functions at the IP are $\beta_p^* = 0.3\,\mathrm{m}$ for the proton beam and $\beta_{\overline{p}}^* = 1.0\,\mathrm{m}$ for the antiproton beam. Table 9 lists the design parameters of the interaction region.

bunch length σ_s	0.3 m
proton normalized emittance $\epsilon_{p.n}$	$1.7\pi\,\mu$m
antiproton normalized emittance $\epsilon_{\overline{p}.n}$	$20\pi\,\mu$m
proton β^*	0.3 m
antiproton β^*	1.0 m

Table 9: Parameter table.

With equal emittances in both transverse planes, the best beam–beam performance is obtained with round beams at the IP. The required equal β–functions in both planes are provided by low–β quadrupole triplets near the interaction point. The quadrupoles for the low–energy proton beam are actually common to both beams; an additional vertical dipole field separates the two beams by deflecting the low–energy proton beam to a larger angle than the high–energy antiprotons. This field configuration is achieved by realization of those magnets as superconducting quadrupoles with additional dipole windings.

The low–β triplet quadrupoles in the antiproton ring are designed as normal–conducting septum quadrupoles to minimize the required beam separation at the location of the first magnet. This configuration is schematically shown in Figure 22.

Focusing for both beams is provided by quadrupole triplets. The shared superconducting low–β magnets for the low–energy proton beam have peak fields of about 1.5 T for a beam pipe radius sufficient to provide a minimum aperture of 12σ for both beams, where σ denotes the transverse rms beam size. Figure 23 shows the proton low–functions around the IP. The normal–conducting septum quadrupoles for the high–energy antiproton beam have a peak field below 1.0 T for a minimum aperture of 12σ. The resulting β–functions are depicted in Figure 24. The septum itself is assumed to have a thickness of 5 mm in the horizontal mid–plane of the magnet. This is achieved by a triangular cut–out on the out-

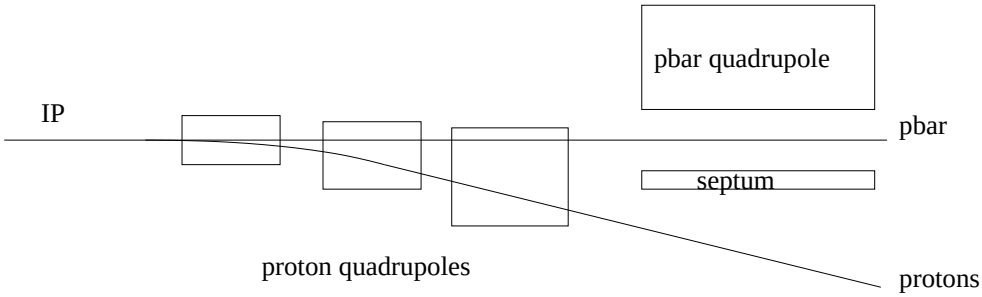

Figure 22: Schematic drawing of the interaction region configuration (top view).

side of the septum plate, which can be tolerated in terms of saturation since the magnetic field on the septum plate in the horizontal mid–plane of the magnet vanishes. Taking into account the wall thickness of the two beam pipes at the septum, the required separation of the two beams there is approximately

$$d = 12\sigma_p + 12\sigma_{\overline{p}} + 10\,\mathrm{mm} \quad (26)$$
$$= 67\,\mathrm{mm}. \quad (27)$$

This is achieved by a dipole field of 0.14 T over the total length of the superconducting quadrupoles.

With the parameters given in Table 9, the resulting beam–beam parameter

$$\xi = \frac{r_p}{4\pi\sigma^2} \cdot \frac{\beta^*}{\gamma} \cdot N \quad (28)$$

can be calculated. Here, r_p denotes the classical proton radius, γ the Lorentz factor of the beam under consideration, and N the number of protons (antiprotons) per bunch. For $N = 1.0{\cdot}10^{11}$ protons and antiprotons, the resulting beam–beam tune shift is $\xi_p = 6.25{\cdot}10^{-3}$ for the proton beam and $\xi_{\overline{p}} = 7.5 \cdot 10^{-3}$ for the antiproton beam, which seems to be realistically achievable, based on experience at existing hadron colliders.

10.4.1 Luminosity Estimate for the Asymmetric Collider

The resulting luminosity for a single proton bunch colliding with three antiproton bunches of equal intensity of $N_p = N_{\overline{p}} = 1.0 \cdot 10^{11}$ particles yields

$$\mathcal{L} = \frac{N_p N_{\overline{p}} f_c}{4\pi\sigma} \quad (29)$$
$$= 1 \cdot 10^{30}\,\mathrm{cm}^{-2}\mathrm{sec}^{-1}, \quad (30)$$

where f_c denotes the bunch crossing frequency.

It should be emphasized here that in order to maximize luminosity the circumference ratio of the two storage rings needs to be reflected in the number of bunches circulating in each ring; hence the number of antiproton bunches needs to three times larger than the number of proton bunches.

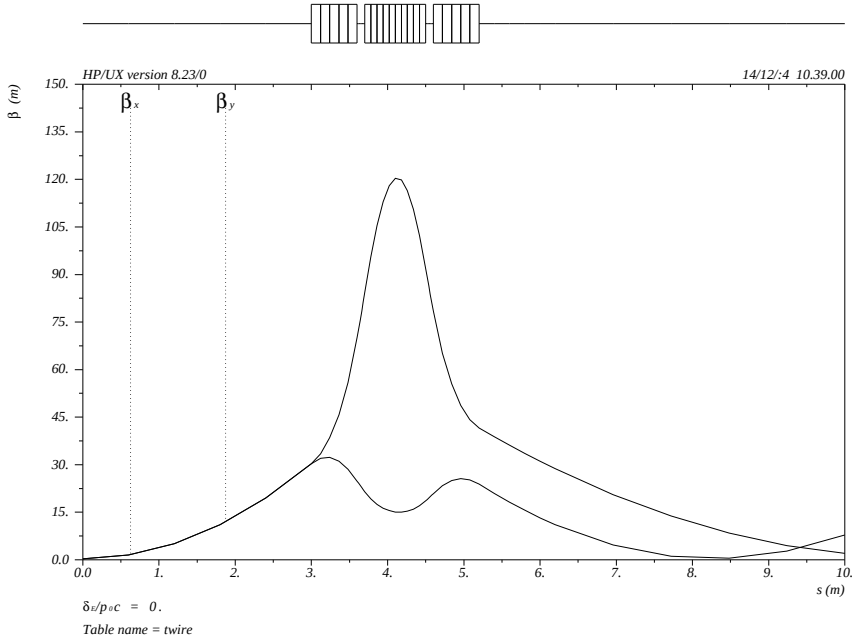

Figure 23: Proton low–β lattice (one side only). Focusing is provided by a superconducting quadrupole triplet, starting at a distance of 3.0 m from the interaction point. The first and third magnet of the triplet are horizontally focusing, while the center quadrupole focuses in the vertical plane.

10.4.2 Intensity dependent Limitations

Due to the high bunch charge of $N = 1.0 \cdot 10^{11}$ particles per bunch in conjunction with low beam energies, intensity dependent effects need to be studied carefully. Here we list some estimates of high intensity effects that are to be expected at the proposed facility.

10.4.2.1 Touschek Lifetime Single scattering of particles within the same bunch leads to momentum transfer from the transverse into the longitudinal plane, where particles get lost if their longitudinal momentum exceeds the momentum acceptance of the machine. The resulting Touschek lifetime is expressed as [164]

$$\tau^{-1}_{\text{Touschek}} = \frac{N r_p^2 c}{8\pi\sigma_x\sigma_z\sigma_s} \cdot \frac{\left(\frac{\Delta p}{p}\right)^{-1}}{\gamma^2} \cdot D(\xi). \tag{31}$$

Here, r_p denotes the classical proton radius, while c is the velocity of light. The function $D(\xi) \approx 0.3$ for realistic parameter ranges [164]. Assuming a momentum acceptance of $\Delta p/p = 0.01$ and using average values of $\sigma_x = \sigma_y = 3.5\,\text{mm}$ and $\sigma_s = 0.3\,\text{m}$ for the

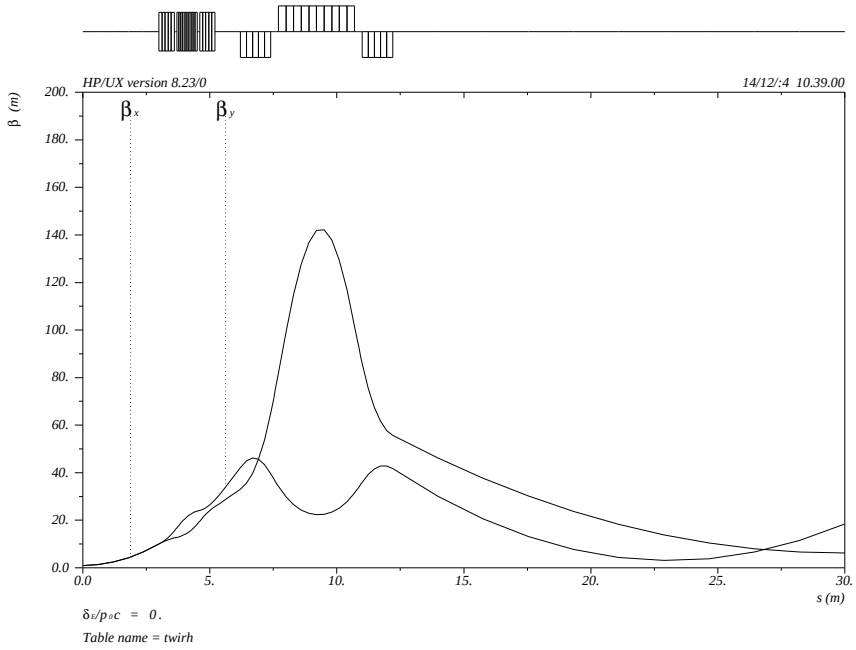

Figure 24: Antiproton β–functions around the IP (one side only). Focusing is provided by a normal–conducting septum quadrupole triplet. The superconducting proton low–β triplet on the left has only little effect on the antiproton optics due to the higher beam rigidity.

transverse and longitudinal rms beam sizes, respectively, this yields a Touschek lifetime exceeding a year. This effect is therefore of no concern for the facility.

10.4.2.2 Intrabeam Scattering Multiple scattering of particles within the same bunch, also called intrabeam scattering, leads to emittance growth in all three dimensions. Growth rates are calculated as [164]

$$\frac{1}{T_p} = \left\langle A\frac{\sigma_h^2}{\sigma_p^2} f(a,b,q) \right\rangle, \tag{32}$$

$$\frac{1}{T_x} = \left\langle A\left[f\left(\frac{1}{a},\frac{b}{a},\frac{q}{a}\right) + \frac{D_x\sigma_h^2}{\sigma_{x\beta}^2} f(a,b,q)\right]\right\rangle, \tag{33}$$

$$\frac{1}{T_y} = \left\langle A\left[f\left(\frac{1}{b},\frac{a}{b},\frac{q}{b}\right) + \frac{D_y\sigma_h^2}{\sigma_{y\beta}^2} f(a,b,q)\right]\right\rangle, \tag{34}$$

with

$$A = \frac{r_p^2 cN}{64\pi^2\beta^3\gamma^4\epsilon_x\epsilon_y\sigma_s\sigma_p}, \tag{35}$$

$$\frac{1}{\sigma_h^2} = \frac{1}{\sigma_p^2} + \frac{D_x^2}{\sigma_{x\beta}^2} + \frac{D_y^2}{\sigma_{y\beta}^2}, \tag{36}$$

$$a = \frac{\sigma_h \beta_x}{\gamma \sigma_{x\beta}}, \tag{37}$$

$$b = \frac{\sigma_h \beta_y}{\gamma \sigma_{y\beta}}, \tag{38}$$

$$q = \sigma_h \beta \sqrt{\frac{2d}{r_p}}. \tag{39}$$

ϵ_x and ϵ_y denote the horizontal and vertical emittance, respectively, while d is the smaller of the horizontal and vertical rms beam sizes.

Using the beam emittances given in Table 9, $\sigma_p = 1.0 \cdot 10^{-3}$, and average β–functions $\beta_x = \beta_y = 30\,\mathrm{m}$, the value of the function $f(a, b, q)$ can be obtained from Ref. [164] as $f(a, b, q) \approx -100$. This yields a longitudinal emittance growth rate of

$$T_p^{-1} \approx 10^{-3}\,\mathrm{sec}^{-1}, \tag{40}$$

and results of similar magnitude for the transverse rates T_x^{-1} and T_y^{-1}, which is comparable to the design cooling times. This is a major concern for the proposed facility and requires a thorough investigation, taking into account the actual accelerator lattices.

11 Polarimetry

The beam and target polarization will be determined by the following scheme: First the target polarization using an unpolarized antiproton beam is established by either one of two methods:

(1) with reference to a suitable sampling polarimeter of the Breit–Rabi [165] or Lamb–shift [166] type, which spin–analyzes a small fraction of atomic hydrogen extracted from the target cell.

(2) elastic proton–antiproton scattering data at low energies (500–800 MeV) where analyzing power data from PS172 [167] are available. Scattering data of lower precision extend up to 2.5 GeV [168].

This allows one to calibrate a suitable detector asymmetry, derived from elastic scattering, in terms of an effective analyzing power. Since target and beam analyzing power in $\bar{p}p$ scattering are identical, the polarization of the beam can now be measured with an unpolarized target (e.g. by injecting unpolarized hydrogen gas into the cell). When subsequent fills of the HESR are made with different beam energies, it is straightforward to establish polarization standards at any energy within the HESR range by exploiting the fact, that the target polarization is constant with time – or monitored by the sampling polarimeter – and independent of energy [169].

Part III
Staging of Experiments

The PAX collaboration proposes an approach that is composed of different stages. During these the major milestones of the project can be tested and optimized before the final goal is approached: a polarized proton–antiproton asymmetric collider, in which about 3.5 GeV/c polarized protons will collide head–on with polarized antiprotons with momenta up to 15 GeV/c.

12 Preparatory Phase

12.1 Accelerator: Design and Construction of the Antiproton Polarizer Ring

Tuning and commissioning of the APR will require a beam of polarized protons. Such a beam and a hall including infrastructure are readily available at COSY–Jülich. This makes Institut für Kernphysik of the Forschungszentrum Jülich the ideally suited site for the design, construction and testing of the APR.

12.2 Physics in the Preparatory Phase

The calculation of the polarization transfer employed to polarize the antiprotons is text book QED physics [170]. The polarization transfer technique is at the core of an extensive physics program at JLAB dedicated to experiments on the separation of the charge and magnetic form factors of the proton [126]. The existence of the effect has been verified in the FILTEX experiment at TSR–Heidelberg in 1992 with a 23 MeV proton beam. For antiprotons the optimal energy is around 50 MeV (see Sec. 8.3). We don't consider necessary a further demonstration of the validity of this fundamental QED derivation and, unless specifically requested by the QCD–PAC, we would not embark on such endeavor. Instead, we would very much prefer to concentrate on the design, construction, commissioning and direct proof with the APR that protons can be polarized to a high degree with a design energy of 50 MeV. If however, the QCD–PAC will ask us for a pre–APR test, this can be carried out at COSY.

- A verification of $\sigma_{EM_\perp}$ at 40, 70 and 100 MeV is possible using the polarized internal target at the ANKE interaction point.

  The measurement can be performed by injecting pure states $|\,1\,\rangle$ or $|\,3\,\rangle$ in a weak transverse target guide field (10 G). In this situation the electron target polarization Q_e is equal to the proton target polarization Q_p and Q_p can be measured by pp elastic scattering by using the ANKE spectator detector system [171].

12.3 Development of Polarized Sources

The polarization mechanism relies on an efficient, high–intensity source for polarized hydrogen atoms. In the PAX collaboration, most of the world–expertise on polarized sources is already present (Erlangen, Ferrara, Gatchina, Jülich, Madison). A program for the development of a new generation of high–intensity atomic beam sources has been already started in Ferrara and it will be pursued and extended during the preparatory phase of the PAX experiment.

13 Phase–I

13.1 Accelerator: Transfer of APR and CSR to FAIR

APR and CSR will be placed inside the HESR. The straight sections of CSR and HESR are parallel, whereby an additional IP, independent of the PANDA IP, is formed.

13.2 Physics in Phase–I

A beam of unpolarized or polarized antiprotons with momentum up to 3.5 GeV/c in the CSR ring, colliding on a polarized hydrogen target in the PAX detector will be available. This phase is independent of the HESR performance. This first phase, at moderately high–energy, will allow for the first time the measurement of the time–like proton form factors in single and double polarized reactions from close to threshold up to 3.5 GeV/c. It will be possible to determine several (single and double) spin asymmetries in the elastic $p\bar{p} \to p\bar{p}$ process. By detecting back scattered antiprotons one can also explore hard scattering regions of large t: in the proton–proton scattering reaching the same region of t requires a twice higher energy. This would allow us to carry out the measurements of form factors with a fixed polarized hydrogen target bombarded by antiprotons orbiting in the CSR momenta of 3.5 GeV/c. The CSR would be fed with antiprotons from the APR.

14 Phase–II

14.1 Accelerator: HESR modifications to collider mode or to polarized internal target.

A chicane for CSR and HESR has to be built to bring the proton beam of the CSR and the antiproton beam of the HESR to a collision point at the PAX IP.

14.2 Physics in Phase–II

This phase will allow the first ever direct measurement of the quark transversity distribution h_1, by measuring the double transverse spin asymmetry A_{TT} in Drell–Yan processes $p^{\uparrow}\bar{p}^{\uparrow} \to$

e^+e^-X as a function of Bjorken x and Q^2 ($= M^2$). Two possible scenarios might be foreseen to perform the measurement.

(a) A beam of polarized antiprotons from 1.5 GeV/c up to 15 GeV/c circulating in the HESR, colliding on a beam of polarized protons of 3.5 GeV/c circulating in the CSR. This scenario requires to demonstrate that a suitable luminosity is reachable. Deflection of the HESR beam to the PAX detector in the CSR is necessary (see Fig. 9). By properly varying the energy of the two colliding beams, this setup would allow a measurement of the transversity distribution h_1 in the valence region of $0.1 < x < 0.8$ with corresponding Q^2 in the range $4 < Q^2 < 100$ GeV^2 (see Fig. 1). A_{TT} is predicted to be larger than 0.2 in the full kinematic range, see Fig. 1, and the cross section is large enough to get $\sim$ 2000 events per day at a luminosity of $5 \cdot 10^{30}$ cm^{-2}s^{-1}. Such an experiment can be considered, for h_1, the analogous of polarized DIS for the helicity distribution Δq; the kinematical coverage in (x, Q^2) will be similar to that of the HERMES experiment.

(b) Should the requested luminosity for the collider not be reachable, a fixed target experiment can be performed. A beam of 22 GeV/c (15 GeV/c) polarized antiprotons circulating in the HESR, can be used to collide on a polarized internal hydrogen target. Also this scenario requires the deflection of the HESR beam to the PAX detector in the CSR (see Fig. 9). A theoretical discussion of the significance of the measurement of A_{TT} for a 15 GeV/c beam impinging on a fixed target is given is Refs. [2] and [3] and the recent review paper [11]. This measurement will explore the valence region of $0.3 < x < 0.8$ with corresponding $4 < Q^2 < 16$ GeV^2, see Fig. 1. In this region A_{TT} is predicted to be large (of the order of 0.3, or more) and the expected number of events can be of the order of 2000 per day.

Part IV
Detector

15 Requirements and Design Considerations

Since a definite choice has not been made yet on the accelerator configuration (fixed target or collider), it might be premature at this stage to define the detector details. Still some general considerations can be anticipated. What we present here is just meant as a conceptual detector design suitable for the PAX physics program. Possible alternative scenarios will be discussed at the end in Sec. 19.

In the following we focus on the most challenging task of the PAX physics program: the measurement of the Drell–Yan reaction to access the transversity distribution h_1. A detector optimized for this task can be designed to be suitable to achieve also the other goals of the PAX experimental program.

In the detector concept, presented below, the following criteria have been pursued:

- optimize the acceptance at large angles. The double spin asymmetry of the $q\bar{q} \to \ell^+\ell^-$ QED elementary process,

$$\hat{a}_{TT} = \frac{\sin^2\theta}{1+\cos^2\theta}\,\cos 2\phi\,, \tag{41}$$

  maximizes the sensitivity of the measured asymmetry A_{TT} for the transversity distribution h_1 for 90–degree scattering in the center–of–mass of the partonic system, where $\sin^2\theta \sim 1$ (see Eq. (1). We note that also the $\overline{p}p$ elastic scattering at 90° c.m. and the form–factor measurements benefit from a large angle detector;

- trigger efficiently on the rare Drell–Yan events. At the PAX energy the few nb Drell–Yan cross section should be clearly identified from a total $\overline{p}p$ cross–section of about 50 mb;

- cope with the overwhelming background. The lepton identification should provide a rejection factor of the order of 10^4 to 10^5 against hadrons. Secondary leptons, produced in meson decays and in secondary interactions in the detector material, should be vetoed as well;

- provide of the order of 1 % resolution for the invariant mass of the lepton pairs, in order to efficiently distinguish the contribution of the resonances (J/Ψ and ψ) from the continuum;

- (if the collider option would be pursued) be compatible with the asymmetric collider lattice. In particular any effect of the spectrometer magnet should be perfectly compensated in order to not degrade the beam polarization;

- provide a unique facility as complete as possible and flexible to allow the study of auxiliary processes and additional physical channels which might become interesting during the next 10 years.

In order to best match the above requirements, the PAX detector is designed to measured electron–positron pairs of large invariant mass.

15.1 Physical Channels

To reveal rare reactions like the Drell–Yan process and the $\overline{p}p \to e^+e^-$ annihilation, the PAX detector has to be conceived as a large acceptance apparatus capable of unambiguously identifying electron–positron pairs of large invariant mass and precisely measuring their momenta. The detector has to be able to measure electron pairs with large opening angle, in a wide kinematic range with good angular and energy resolution. A clear particle identification is required to separate the electrons of the wanted processes from the large pion background.

Reactions characterized by two–body hadronic final states like elastic scattering, present a higher cross–section and put less stringent constraints on the detector design. They can be identified by measuring scattering angles and momenta of the hadronic particles by employing coplanarity and total momentum conservation. Finally, the PAX detector can measure the energy of gammas from radiative processes and π^0 and η decays.

15.2 Particle Identification

The Drell–Yan production rate is of the order of 10^{-7} of the total $\overline{p}p$ reaction rate and results in a low yield of the e^+e^- signal per interaction. In order to maximize the dilepton detection efficiency, the PAX spectrometer must provide a large geometrical acceptance. At the same time, the high interaction rate (of the order of 1 MHz) together with the hadron multiplicity represents a serious challenge to the trigger system which has to select the events containing the lepton tracks. An accurate lepton identification can only be achieved by detectors which are highly insensitive to the large flux of hadrons. In order to minimize the background from lepton misidentification at a typical prevailing e/π ratio of 10^{-4}, redundant recognition of lepton tracks is essential. For the considered range of momenta (between 0.5 and 10 GeV/c) electrons offer the advantage with respect to muons of that they can be identified in a hadron blind gas threshold Čerenkov detector. This device can be operated on a fast time scale to meet the stringent trigger requirements in the high–rate high–multiplicity environment. Additional discrimination against pions can be provided both by the cluster lateral profile in the electromagnetic calorimeter (CAL) and by the E/p ratio between the energy E measured in the CAL and the momentum p measured in the spectrometer. With these constraints, the required rejection factor of the order of 10^{10} against hadronic events (corresponding to 10^5 for single track events) is achievable, as demonstrated in other experiments [172, 173].

15.3 Magnetic Field Configuration

The spectrometer magnet has to be compatible with the Čerenkov detector which needs to work in a field free region. A toroid configuration satisfies this requirement resulting in a negligible fringe field both along the beam line and external external volume where the Čerenkov detector is located. A toroid field is always orthogonal to the particle momentum, hence the bending effect is optimized regardless of the scattering angle. An eight–coil configuration can be designed to give excellent coverage over the azimuthal angles, facilitating the detection of the $\cos(2\phi)$ modulation of the transverse asymmetry, covering the region around $2\phi = n\pi$, where the sensitivity is largest (see Fig. 26). The azimuthal acceptance is optimized by placing service and support structures of the various detectors in the shadow of the toroid coils. The detectors are arranged in an azimuthally eight–fold segmented, frustum–like geometry. For compactness, the inner tracking close to the interaction point is provided by silicon strip detectors. The outer tracking, behind the magnet, is provided by two sets of conventional drift–chambers. The Čerenkov detector is placed outside the magnet, in between the two sets of drift–chamber, fitting the $0.6 - 0.8$ m tracking arm required to obtain the ~ 1 % momentum resolution with a typical spatial resolution of ~ 200 μm.

15.4 Mass Resolution

A lepton pair invariant mass resolution close to 1 % is required to isolate the charmed resonance signals from the continuum. This value necessitates that the momentum resolution is of the same order of magnitude for lepton tracks with a momentum range between 0.5 and 10 GeV/c. This large momentum range leads to a non–focusing geometry with a transverse momentum kick up to $\Delta p \sim 0.3$ GeV/c. The maximum value of Δp is required in the forward region where the particle momenta are larger and is provided by an integrated field along the particle trajectory of $Bl \sim 1$ Tm. In order to limit the cost of the external electromagnetic calorimeter, the detector should be compact: by assuming a value of $l = 0.7$ m in the forward direction, the required magnetic field is of the order of 1.5 T. A transverse momentum kick of $\Delta p \sim 0.3$ GeV/c puts constraints on the position resolution of the tracking detectors to achieve the required momentum resolution. At a momentum of 10 GeV/c, the deflection angle equals about 2°. A model calculation shows that an uncertainty in the position lower than 30 μm (200 μm) in the inner (outer) tracking region is needed to obtain a relative momentum resolution of about 1 %. This resolution can be provided by conventional silicon strip detectors (SiD) close to the target and drift–chamber modules (DCH) outside the magnet. The high spatial resolution provided by the silicon detector will help to identify the background leptons from secondary vertex (like $D^{\pm}$ decays). The required momentum resolution can only be achieved by keeping multiple scattering in the magnetic field region small. If only multiple scattering is taken into account, the momentum resolution of ~ 1 % at the smallest accepted momenta of 0.5 GeV/c requires an effective thickness less than 0.05 X_0. The amount of material in the tracking region should be minimized also to reduce the gamma conversion probability and energy loss by

radiation. The first active tracking layers placed inside the target vacuum chamber can be used to veto gamma conversions as close as possible to the interaction point.

15.5 General Remarks

The present conceptual detector design is based on existing experiments which have been proven to perform well measuring final–state particles and energies similar to the ones anticipated at PAX.

Once the PAX experiment is approved, each of the detector componentss will be further optimized depending on the chosen beam configuration. The performance of the detectors will finally depend (and benefit) from the development in technology over the course of the next ten years. Additional detectors can also be implemented to enhance the flexibility of the PAX instrument. As an example, hadron identification at forward scattering angles could be considerably improved by adding an internally–reflecting ring–imaging Čerenkov detector [174].

The PAX detector will be mounted on a platform which can be moved on rails in and out of the beam line. For simplicity, in the following we will refer only to Drell–Yan processes, the argument holds for J/Ψ decays and time–like electromagnetic form factors as well.

16 Overview of the PAX Spectrometer

The PAX large–acceptance spectrometer (LAS) (Fig. 25) is optimized to detect electromagnetic final states with two charged tracks of high invariant mass. A clear identification of electrons is required to separate scattered electrons of the Drell–Yan mechanism from the large π background. The detector is designed to also detect two–body hadron reactions using kinematical constraints, i.e. coplanarity and total momentum conservation. Moreover it can measure the energy of gammas from radiative processes and π^0 and η decays.

The very inner part of the detector is devoted to triggering and tracking of charged particles. The scattering angles as well as the initial trajectory for the determination of the particle's momentum are measured by a vertex tracking system consisting of three layers of double–sided silicon strip detectors (SiD). The momentum measurement is completed by two sets of drift chambers behind the magnet (DC). A possible additional set of drift chambers inside the magnet (MC) would improve the matching between the inner and outer tracks and help to resolve multiple tracks and to identify gamma conversions. This will allow us to detect low–momentum tracks which do not reach the external section of the spectrometer.

A threshold Čerenkov counter (CER) provides trigger capability for electrons and positrons produced in Drell–Yan processes. Electron and photon energies and directions are measured by the CAL. Both the CER and the CAL provide fast response and can be employed in the selection of electromagnetic particles to obtain a π/e rejection factor

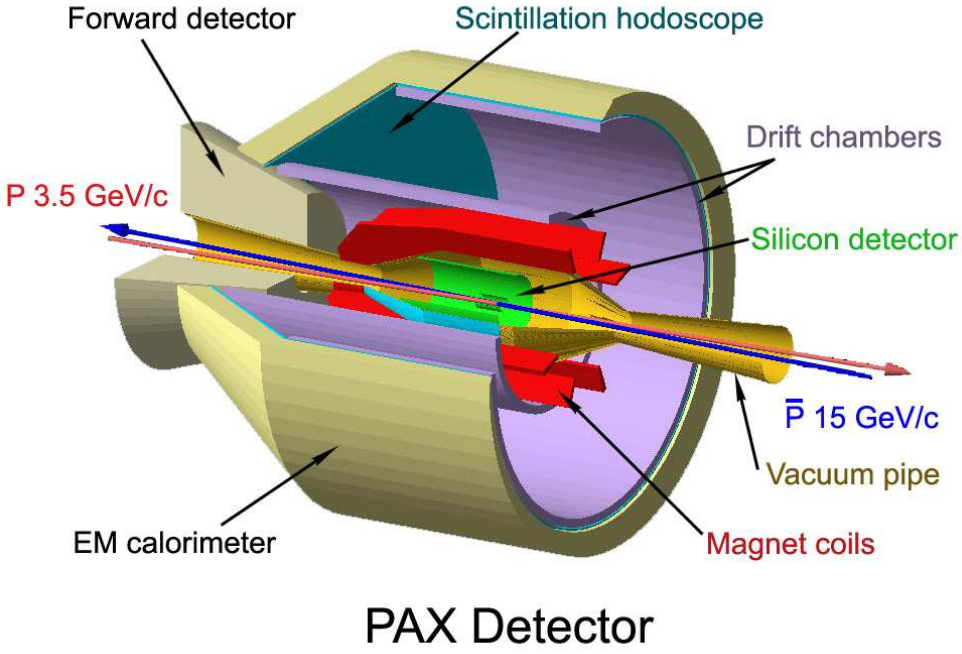

Figure 25: Artists view of the PAX spectrometer.

$\lesssim 100$ at trigger level and larger than 10^4 in the off–line analysis for a single track. A pre–shower detector (PS) can possibly be added in front of the calorimeter to improve the pion rejection and the resolution on the impact point of photons. The outermost set of drift chambers can be filled with Xe–methane gas and can be complemented by a radiator to provide an additional π rejection through transition radiation detection.

The central detector is designed to assure full acceptance between $\pm 20^0$ and $\pm 130^0$ for polar angles in the laboratory frame. It is not active in the small sectors of azimuthal angles in correspondence of the toroid coils. In these sectors the service systems for the detectors and the support structure of the system can be mounted. In the present design, no real limit exists for the maximum acceptable polar angle: the above values can be taken as indicative for the collider option and can be easily adapted to match different beam configurations. The detectors point toward the central part of the interaction region in a projective geometry.

An internal reflecting ring–imaging Čerenkov counter (DIRC) can be employed to identify charged hadrons (pions, kaons and protons). This provides flavor separation in single–spin asymmetry investigations, as well as in the analysis of other semi–inclusive and exclusive channels. The CAL allows the reconstruction of neutral pions in the hadronic final state. CER and CAL are included in the trigger together with a first hodoscope placed in front of the magnet and a second one before the calorimeter.

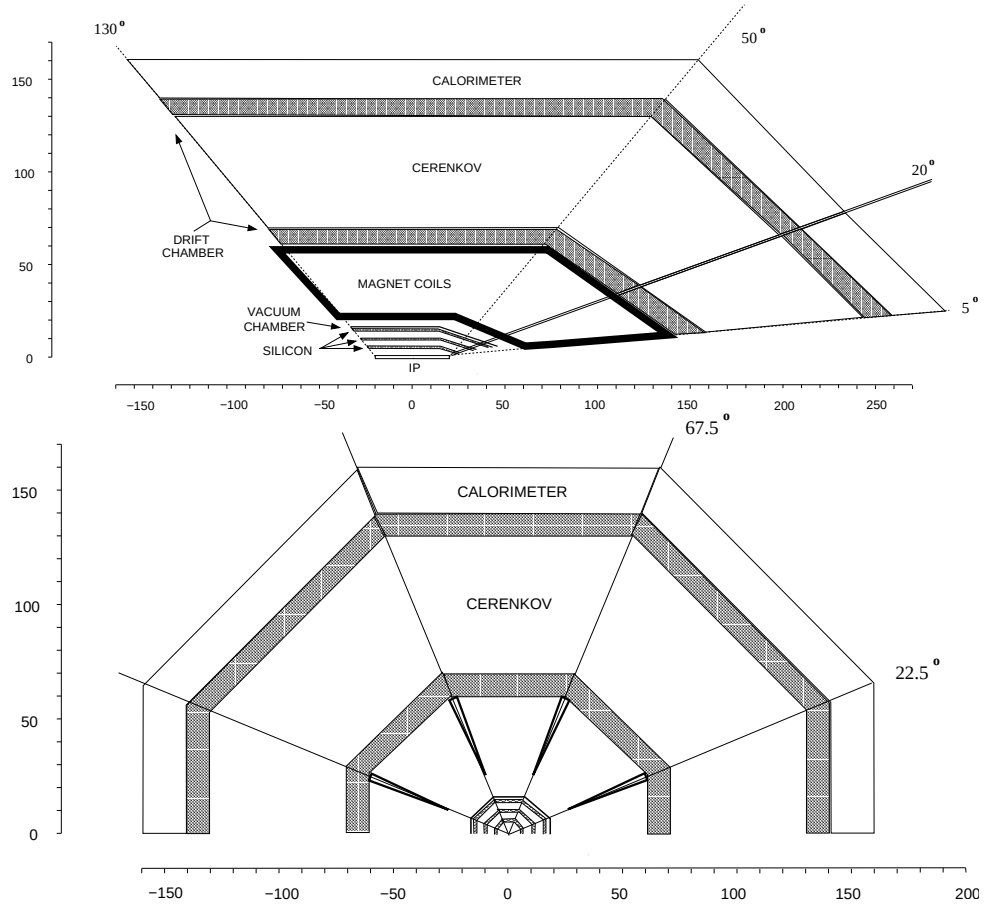

Figure 26: Sketch of the PAX detector, showing a side view ($[z, y]$, top) and a view in beam direction ($[x, y]$, bottom). The optional forward detector, sensitive at laboratory polar angles between 5° and 20°, is also indicated.

16.1 Toroid Magnet

The toroid magnet consists of 8 coils symmetrically placed around the beam axis. A support ring upstream of the target hosts the supply lines for electric power and for liquid helium. At the downstream end, an hexagonal plate compensates the magnetic forces to hold the coils in place. The field lines of an ideal toroid magnet are always perpendicular to the path of the particles originating from the beam line. Since the field intensity increases inversely proportional to the radial distance: greater bending power is available for particles scattered at smaller angles, which have higher momenta. These properties help to design a compact spectrometer that keeps the investment costs for the detector tolerable. The production of such a field requires the insertion of the coils into the tracking volume shadowing part of the azimuthal acceptance. Preliminary studies show that the use of superconducting coils, made by a Nb_3Sn–Copper core surrounded by a winding of Aluminum for support and cooling, allows one to reach an azimuthal detector acceptance in excess of 80%, while the radius of the inner tracking volume can be kept below 0.7 m.

16.2 Silicon Detector

Three layers of double–sided silicon strip detector provide a precise vertex reconstruction and tracking of the particles before they reach the magnet. The design is based on the vertex detector of BABAR [174], with a smaller number of silicon layers to minimize the radiation length of the tracking material. The read–out electronic can be mounted in the front and back parts of the detector, outside the acceptance of the spectrometer. With a pitch of $50-100$ μm it is possible to reach an intrinsic spatial resolution of $10-20$ μm. Such a spatial resolution should allow one to partially resolve and reject the secondary decays of $D^{\pm}$ mesons into leptons. Due to the associated production of charmed mesons, this kind of background can not be completely eliminated by subtracting the dilepton events with the same charge. The number of channels required to cover the 40 cm long interaction point is of the order of $2 \cdot 10^5$, comparable with the BABAR experiment [174].

16.3 Drift Chambers

The required position resolution of 200 μm after passage through the magnetic field can be achieved using conventional drift chambers [175, 176]. On the basis of an existing set–up [175], the chambers are assembled as modules consisting of four pairs of tracking planes with wires at $-30°$, $0°$, $0°, +30°$ with respect to the direction transverse to the plane of the coil, i.e. parallel to the magnetic field lines. The wires of the planes oriented at $0°$ are staggered in order to resolve left–right ambiguities. Uniform arrays of cathode wires separate the different cell layers. The tilted angles are optimized to provide a two–dimensional hit–point with emphasis on the polar (bending) coordinate. The support structure of the wires, together with the feedthroughs and the circuit boards for sector pairs, can fit within the shadow of the coils [176]. With a cell size of 0.5 cm, the total number of channels is about 32000. The expected momentum resolution is of the order of 1 % over the kinematic range of the experiment.

16.4 Čerenkov Detector

A threshold gas Čerenkov counter is used to trigger and select electrons in the presence of a large hadronic background. The required background event reduction at trigger level is of the order of 10^3, and is achieved with a π/e rejection factor of $\lesssim 100$ on the single charged particle. The counter occupies a $60-80$ cm thick shell around the inner tracking detector and is divided into eight identical azimuthal sectors. Each sector can be further subdivided into s small number of gas cells. In this way the gas filling of each cell can be optimized cover the momentum range of interest by exploiting the correlation between scattering angle and particle momentum [177]. Freon–12 and CO_2 are suitable gases for the energies involved in the PAX experiment [177, 178]. Čerenkov photons are reflected by aluminized carbon–fiber mirrors towards photomultipliers that can be located outside of the spectrometer acceptance within the shadow of the toroid coils [179]. The spatial resolution in the polar angle can be enhanced by segmenting the mirror and focalizing

the light onto a row of photomultipliers [179]. A solution with multi-wire proportional chambers as photon detector with a solid CsI cathode pad is under study to obtain a higher spatial resolution [180].

16.5 Calorimeter

The calorimeter consists of radiation–resistant lead tungstate ($PbWO_4$) crystals which have been selected for their high density, short radiation length and small Moliere radius. Unlike the CMS [181] and ALICE [182] experiments, the PAX calorimeter is not immersed inside a high magnetic field. This makes the use of photomultiplier tubes possible, to provide less noise and better resolution at low energies. The crystals are arranged in a barrel and in a conically–shaped endcap of the experiment in a quasi–projective geometry. They are supported from outside to minimize the material preceding the active region. The blocks have an area of $4 \times 4\,\mathrm{cm}^2$ and a variable length matching the mean momentum of the impinging particles. The expected energy resolution can be parameterized as $\sigma(E)/E[\%] = 1.8/\sqrt{(E[\mathrm{GeV}])} + 0.4$ [183]. For the conditions at PAX this translates into an energy resolution of $2-3$ %. The calorimeter is used to trigger on Drell–Yan electrons by selecting the events with energy deposited in two clusters, both with a corresponding positive Čerenkov signal, which have large invariant mass. A back–to–back topology and a total deposited energy equal to the center–of–mass energy can be required to trigger on $\overline{p}p \to e^+e^-$ annihilation events. Assuming an electron identification efficiency of 90 %, a hadron rejection factor of several hundreds can be achieved by using the lateral profile of the deposited energy and the E/p ratio between energy E deposited in the calorimeter and the momentum p measured in the spectrometer. The estimated number of crystals in the calorimeter is about 15000.

16.6 Hodoscopes

Two hodoscope planes are used for triggering together with CAL and CER detectors. A front trigger scintillator is placed directly upstream of the vacuum chamber. It consists of eight–fold segmented foils of standard plastic scintillator, 3.2 mm thick (0.7 % radiation length), read–out by phototubes. A second scintillator hodoscope is placed in front of the calorimeter. The counter is composed of modules of fast scintillators with a large attenuation length (300–400 cm). The modules are longitudinally oriented providing a barrel geometry. The scintillation light is detected by photomultiplier tubes. To provide additional particle identification, a passive Pb radiator (2 radiation lengths) can be placed in front of the external hodoscope to initiate electromagnetic showers that deposit typically much more energy in the scintillator than minimum–ionizing particles.

16.7 Forward Spectrometer

A forward spectrometer (FS) covering scattering angles below 20°, is envisaged to complement the LAS during data–taking at high energy. The tracking system of the forward

spectrometer has the same design as the central one, and will benefit from the large field integral of the toroidal magnet at small angles (where the coils are closer each other).

The particle identification of the forward spectrometer has to be adapted to the chosen beam configuration. The sensitivity on the transverse distribution h_1 in the forward direction is poor, because $\hat{a}_{TT}$ is small there. In the asymmetric collider mode, Drell–Yan events with scattering angles below 20° in the laboratory frame basically do not improve the statistical precision of the h_1 measurement. The forward region will be crucial for the SSA measurements at high energy and large values of x_F, so that the forward particle identification has to be optimized for hadrons. One promising option is to make use of a RICH detector [184]. For a fixed–target experiment with 22 GeV/c beam momentum, the lower limit of the useful scattering angle reduces to 5° due to the relativistic boost. The PID of the FS has to be optimized for electron detection like the LAS.

16.8 Recoil Detector

A silicon recoil detector system is needed for the low–t antiproton–proton elastic scattering program and will only be installed for these measurements, so that radiation damage will be a minor issue.

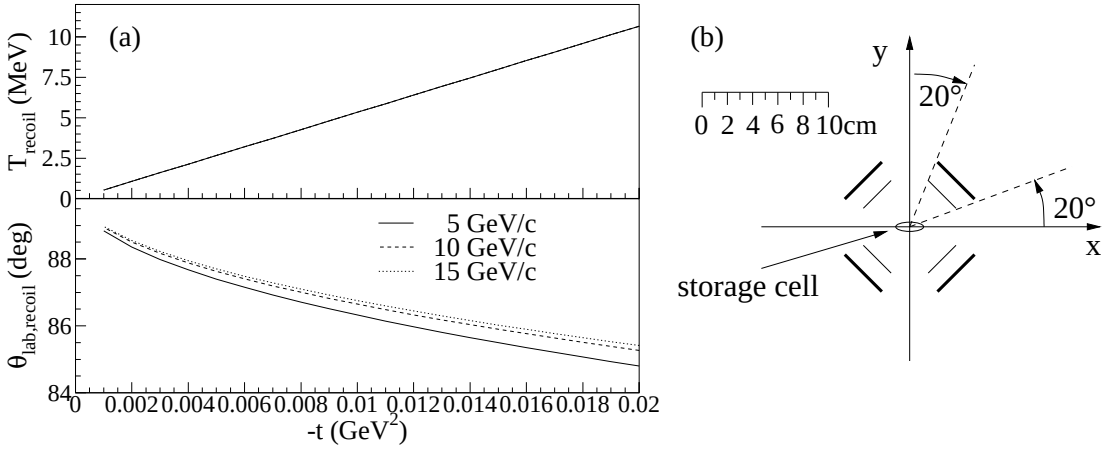

Figure 27: (a) Laboratory kinetic energy (top) and scattering angles (bottom) of the recoil proton for three different beam momenta. (b) Cross sectional view of the recoil detector.

At very low momentum transfer ($|t| = 0.002 \ldots 0.02$ GeV^2) the recoil protons are detected by silicon strip detectors close to 90° laboratory angle. At these angles (cf. Fig. 27a) the protons of interest have energies between 1 and 10 MeV and are stopped in a telescope comprised of a 65 μm thin surface barrier detector and a 1 mm thick microstrip detector. Such a telescope [171] has already been successfully operated in a similar environment at the ANKE experiment at COSY/Jülich. In view of the comparably large cross section ($d\sigma/dt > 150$ mb/GeV^2) a precise measurement of the recoil *energy* is sufficient both to

determine t and to cleanly identify elastically scattered protons as in the E760 experiment at FNAL [185].

Four of these detectors cover azimuthal angle intervals of $\Delta\phi \approx 50^\circ$ in four quadrants, sketched in Fig. 27 (b). The acceptance is matched to the central part of the interaction region (collider mode) or of the storage cell (fixed–target mode). For the fixed–target Phase–I at moderately high energies, dedicated cell walls can be made as thin as 5 μm Teflon – as demonstrated by the PINTEX–experiment at IUCF [186] – and allow the detection of recoil protons down to about 500 keV kinetic energy. However, the low recoil momenta prohibit the use of a strong target guide field, such that measurements must be taken with a single pure hyperfine state and a weak (some mT) guide field to avoid strong bending of the recoils at very low t. The toroid magnet of the spectrometer provides a field free region around the interaction point and does not disturb the recoil trajectory.

The spin–dependent cross section $\frac{\mathrm{d}\sigma}{\mathrm{d}t}$ for vertical beam polarization P_y and a transverse target polarization Q_x, or Q_y is given by

$$\begin{aligned}\tfrac{\mathrm{d}\sigma}{\mathrm{d}\Omega}(\vec{P},\vec{Q},\theta,\phi) = \tfrac{\mathrm{d}\sigma}{\mathrm{d}\Omega}\big|_{\mathrm{unpol.}}\,(1 \quad &+ \quad [(P_y+Q_y)\cos\phi + Q_x\sin\phi]\,A_{\mathrm{N}} \\ &+ \quad P_yQ_y\left[A_{\mathrm{NN}}\cos^2\phi + A_{\mathrm{SS}}\sin^2\phi\right] \\ &+ \quad P_yQ_x\left[A_{\mathrm{SS}} - A_{\mathrm{NN}}\right]\sin\phi\cos\phi)\end{aligned} \tag{42}$$

which relates by integration over ϕ and change of variables to the differential cross section difference

$$\frac{\mathrm{d}\Delta\sigma_T}{\mathrm{d}t} = -\frac{\mathrm{d}\sigma}{\mathrm{d}t}\left(A_{\mathrm{NN}}(t) + A_{\mathrm{SS}}(t)\right) \tag{43}$$

with $\Delta\sigma_T = \sigma\left(\uparrow\downarrow\right) - \sigma\left(\uparrow\uparrow\right)$. With this experiment spin correlation parameter A_{NN}, A_{SS} as well as the analyzing power A_N of $\bar{p}p$ elastic scattering are accessible.

16.9 Trigger and Data Acquisition

The actual interaction rate achievable by the PAX experiment will be precisely estimated only after the final beam configuration is known. However, an upper limit is anticipated to be of the order of a few MHz. A reduction factor of 10^3 at trigger level is then required to keep the rate of read–out events below a few kHz.

For the different physics issues to be studied, dedicated trigger schemes have to be employed. The detection of Drell–Yan electron pairs will be accomplished by using coincidences comprising multiplicity information from the hodoscopes, silicon detectors, CAL and segments of the Čerenkov counter in the LAS. For single–spin asymmetries a single–prong trigger, derived from the forward scintillator hodoscopes and the calorimeter, can be used in a similar way as in the HERMES experiment [187]. For the low–t elastic antiproton–proton scattering the recoil–detector hodoscope provides self–triggering capability for low energy hadrons, as demonstrated at ANKE [171].

High luminosity (above $10^{32}\,\mathrm{cm}^{-2}\mathrm{s}^{-1}$ in the case of unpolarized antiproton beam) and wide solid angle acceptance lead to high counting rates of the detectors. Under these condition the architecture of the trigger and the data acquisition systems are essential in defining the capability of the setup to collect data without large dead time losses.

The trigger system has to be flexible enough to cover different physics issues which demand different trigger selection criteria. It is planned to use a multi–level trigger composed of a fast first level trigger and hardware and software processors at higher levels. The experience obtained in running of HERMES [187], ANKE [188] and other experiments [189] will be employed to a considerable extent. Due to the diversity of the various detectors, sufficient capability for event–selection at the trigger level is available, i.e. multiplicity information, energy loss and total energy, particle identification, tracking and hit–map correlations.

Pipelines and de–randomizing buffers will be used to store the events during the processing at the low–level trigger stages. The event builder will collect information from all the detector readout branches. The event builder protocol has still to be selected in view of fast developing network and computing technologies.

17 Detector Phases

17.1 Detector Phase–I

The fixed–target program of Phase–I in the CSR ring (see Sec. 13) concentrates on the time–like proton form factors and elastic scattering measurements. The simple and over-constraint kinematics of these events puts less stringent requirements on the detector performance. The momentum resolution, for instance, is not a crucial issue, as demonstrated by the E835 experiment [172]. The measurements can start even before the detector is completed and can be used to test and optimize each of the sub–systems, i.e. tracking system and Čerenkov PID. The trigger is provided by two back–to–back tracks. The Čerenkov signals above threshold and the total energy deposited in the calorimeter equal to the center–of–mass energy, can be employed to trigger the rare electron events. At the CSR energies, the outgoing particles have an almost isotropic distribution and a momentum between 0.5 and 1.5 GeV/c. Hadron identification is provided by time–of–flight measurement using the hodoscopes, [175, 176].

17.1.1 The gaseous Fixed-Target

In Phase–I, a storage cell gas target is inserted downstream of the detector. The atomic beam source (ABS) and the injection tube of the cell are placed in the empty solid angle in front of the detector. The conventional design of a storage cell target is described in details elsewhere (Sec. 8.2.1). The polarized gas atoms leave the target cell through the open ends and are differentially pumped by two stages along the beam pipe. This minimizes the degradation of the vacuum and thus its effect on the stored beam. The transition from the cell to the beam pipe could be made smooth using perforated tubes, to avoid the possible generation of wake fields that could cause heating and increase the emittance of the beam. Given the importance of the acceptance in the forward direction, the first pumping system at the cell position is located upstream, like the ABS. The vacuum region extends inside the conic–shaped internal space of the detector and reaches the second pumping system

located just behind the CAL. Particles scattered into the detector exit the vacuum region through a 0.3 mm stainless–steel foil (corresponding to 0.5 % of radiation length) stretched by the toroid coil supports.

17.1.2 The Target Magnet

In order to minimize the material inside the detector acceptance, the magnet is composed of two superconducting coils surrounding the target in the horizontal plane and providing a vertical field up to 0.3 T in the cell volume. The coils can be shaped or correcting coils can be added to improve the homogeneity of the field (if it is required to avoid depolarization effects from the beam current structure). The coils run inside a cooling tube where the liquid He is continuously flowing. The magnet is inside the vacuum region to provide thermal insulation. Four correcting dipoles are added to the beam line to compensate the effect of the PAX magnets on the orbits of the protons and/or antiprotons. For the case where longitudinal target polarization is required, the transverse field will be ramped down. If only one hyperfine state is injected, a longitudinal holding field of some mT is sufficient and can be provided by conventional Helmholtz coils. (When only one hyperfine state is injected in the target, spin–relaxation processes like spin–exchange collisions are practically absent and the condition for a strong holding field is consequently relaxed.)

17.2 Detector Phase–II

The asymmetric–collider program of Phase–II concentrates on the h_1 measurement. The inclusive $\overline{p}p \to e^+e^-X$ Drell–Yan process has poor kinematic constraints. The intrinsic transverse momentum of the quarks, for instance, breaks the coplanarity of the e^+e^- pair. A rejection factor of 10^3 against background events is required to reduce the rate from a few MHz to kHz levels. The trigger asks for two tracks in opposite hemispheres above the Čerenkov threshold. To reduce low–energetic combinatorial background, a cut on the dilepton invariant mass is applied using the deposited energy and the impact point at the calorimeter. The first layer of silicon is used to veto gamma conversions.

18 Performance Summary

The major sources of background to the Drell–Yan process are the π^0 (and η) Dalitz–decays, the gamma conversions and the charmed–meson decays. Dileptons coming from one single light meson decay or gamma conversion can be identified by the low invariant mass. Only multiple decays or conversions may generate a dilepton with invariant mass larger than 2 GeV/c^2. An additional electromagnetic particle in the event can be used to identify the parent π^0 or photon and to reject the candidate. The residual background can be finally subtracted by identification of a leptons pair with the same charge. Due to large mass and associated production, charmed–mesons tend to produce dangerous unlike–sign candidates at high invariant mass. This kind of background can be reduced by reconstructing the

secondary vertex of the decay with the silicon detector: the D^+, D^- mesons have a lifetime comparable to the one of B–mesons whose decay length is routinely measured at the B–factories. In the collider mode, after subtraction of the combinatorial background, a 10^{-1} contamination from charmed–meson decays is left (see Fig. 28). In the fixed–target mode the center–of–mass energy is too low to generate a significant contamination from charmed mesons.

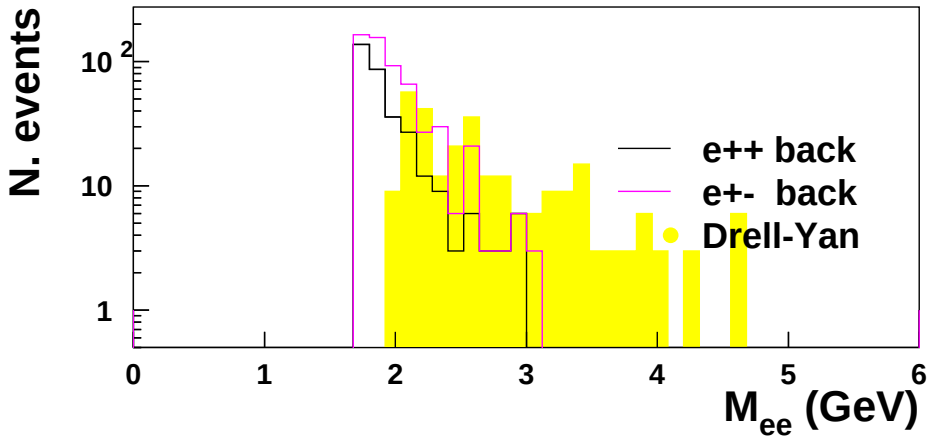

Figure 28: Background estimation for the collider mode. The Drell–Yan signal is generated with a minimum invariant mass of 2 GeV/c^2. The background below 1.5 GeV/c^2 is not shown since it is vetoed by the trigger. Only the gamma conversions taking place before the second tracking layer are taken into account. A perfect performance of the PID and tracking system is supposed here. The generated statistics is $4 \cdot 10^9$ $\overline{p}p$ interactions, corresponding to about 4 hours of data taking at a luminosity of $5 \cdot 10^{30}$ cm^{-2}s^{-1}.

For the count rate estimates, we will focus on the Drell–Yan process, the reaction with the highest demand on luminosity. Other reaction channels of interest have larger cross–sections or, like single–spin asymmetries, may use an unpolarized antiproton beam.

The experimental uncertainty for double–spin asymmetries depends on the number of observed events N as well as on the degree of polarization of the two beams. A value of ($P \gtrsim 0.80$) can be assumed for the proton beam polarization, whereas values of $Q \approx 0.30$ are anticipated for the antiproton beam polarization [123], see Sec. 8. The error is then roughly given by $(PQ\sqrt{N})^{-1} = 4/\sqrt{N}$. It should be noted that an extensive study is foreseen to optimize the spin–filtering process: any beam polarization acquired in addition by the antiproton beam will reduce experimental uncertainties linearly.

For every event, the Bjorken x of the proton and $\overline{x}$ of the antiproton can be extracted from the measured invariant mass ($M^2 = Q^2$) and from the longitudinal momentum ($p_L = s/2 \cdot x_F$) of the lepton pair. In the u dominance hypothesis the $A_{TT}(x, \overline{x})$ asymmetry is

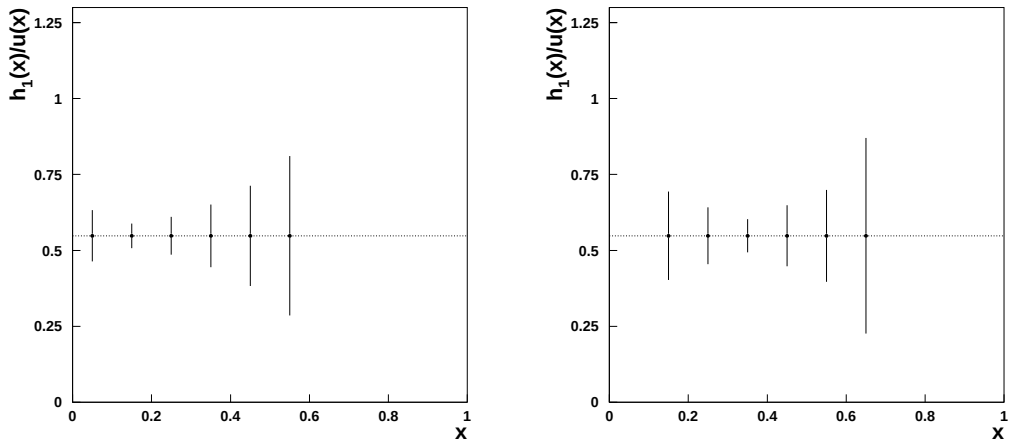

Figure 29: Expected precision of the h_1 measurement for one year of data taking at 50 % efficiency (180 days). An indicative $A_{TT}/\hat{a}_{TT} = 0.3$ has been considered in the simulation. For the collider mode a luminosity of $5 \cdot 10^{30}$ cm^{-2}s^{-1} and a polar angle acceptance between 20° and 130° was assumed (left). For the fixed–target mode at 22 GeV/c beam momentum a luminosity of $2.7 \cdot 10^{31}$ cm^{-2}s^{-1} and a polar angle acceptance between 5° and 50° was assumed (right).

related to the convolution of the transversity distributions $h_1(x) \cdot h_1(\overline{x})$ by the relation

$$A_{TT}(x, \overline{x}) = \hat{a}_{TT} \, \frac{h_1(x)}{u(x)} \frac{h_1(\overline{x})}{u(\overline{x})} \, .$$

During one year of data taking, $h_1(x)$ can be measured in a wide x range, from 0.7 down to 0.05, covering the most interesting valence region and extending to low values of x where theoretical predictions show the largest deviations. The precision achievable in 180 days (one year of data taking with 50 % of efficiency) is shown in Fig. 29. These numbers entail only the non–resonant contribution to the Drell–Yan process: the J/Ψ will enhance the number of events in the $M^2 = 6$–16 GeV^2 range considerably.

For low–t proton–antiproton elastic scattering, recoil–detectors, with a typical area of 5×4 cm^2 each, will be mounted with an angular acceptance matched to the center of the storage cell. Count rates of $6{\times}10^6$/week per t–bin of 0.0005 GeV^2 width are expected to be achieved with a polarized antiproton beam of $P = 30\%$ polarization. Assuming a target polarization of $Q = 90\%$ spin correlation parameters can be measured to a precision of 0.01 within a week, so this program can be finished within a few weeks of beam time.

19 Alternative Scenarios

Two alternative scenarios were considered for the detector design. The first is to select Drell–Yan events with muons. The second is to use a conventional solenoid magnet as spectrometer magnet for the collider mode.

19.1 Drell–Yan with Muons

The design of a detector for Drell–Yan with muons at the PAX energies presents a host of difficulties, which make this a challenging task. The only known way of separating muons from hadrons is to use their low interaction probability and consequent high capability of penetrating large amounts of heavy absorbing material. The hadronic background can originate from decays of charged pions and kaons before reaching the absorber and from hadrons penetrating the material (punch–through). At PAX energies, a typical detector with about 1 m of space before the absorber for charged particle tracking, particle identification and electron/photon detection, cannot guarantee a π/μ rejection factor of 10^2 [190] due to the high probability of meson decays. These decays could be only reduced by moving the absorber closer to the interaction region at the expense of completely losing all the flexibility of the experimental facility. In any case, empty space has to be foreseen for the vacuum chamber as a housing for the vertex detector, so that the secondary–muon rejection factor can hardly exceed 10^3. The absorber puts also severe limitations on the achievable resolution of the dilepton invariant mass. This approach was extensively adopted in the past for Drell–Yan measurements, but at a much higher energy where the decay probability reduces and the absorber filtering is more effective. To keep the background at an acceptable level and not being able to isolate the charmed resonances from the continuum due to the poor resolution, those experiments are limited to a kinematic range of dilepton invariant masses larger than 4 GeV [191]. Such a constraint would limit both the achievable statistics and the covered range in Bjorken x at PAX. Even a large number of heavily instrumented material segments do not suppress hadrons faking muons entirely. Refined studies at the B–meson e^+e^- facilities show that the maximum rejection factors against hadron punch–through achievable with active absorbers are of the order of 10^3 [192, 102]. The above values of pion rejection factors are well below the 10^4 to 10^5 threshold required for an efficient Drell–Yan measurement.

Since there are several powerful well–established techniques to distinguish electrons from pions in the energy range of the PAX experiment, and since these are compatible with a precise measurement of the particle momenta, the Drell–Yan electron channel was selected to be a much more effective solution for PAX.

19.2 Solenoid Magnet

A solenoid field is a natural option for a collider detector since it provides an almost homogeneous field in a large empty volume suitable for tracking. This choice presents some drawbacks for the PAX physics case. Since the spin of the beam particles undergoes

precession inside the longitudinal field of the spectrometer, a set of counteracting–solenoids inside the interaction region is required such that the longitudinal field integral that protons and antiprotons experience before a collision vanishes. Although it is in principle feasible, this solution would complicate the design of the collider IP. The correction has to work for any beam momentum employed in order to vary the center–of–mass energy of the collisions and explore different kinematic regimes. Moreover, the correction can not be exact over the about 30 cm long IP bunch–length and the unavoidable spin precession will be energy dependent. The solenoid is not compatible with a transverse polarized target, hence is not suitable for Phase–I or Phase–II (b) of the PAX physics program (see Sec. 13 and 14).

Because the threshold Čerenkov detector can not be efficiently operated in the strong field of a solenoid magnet, a possible alternative is to employ a transition radiation detector (TRD). The transition radiation, being proportional to the relativistic γ factor of the particle, is effective at high momenta and the required 10^3 pion rejection factor might represent a challenge at PAX energies [193, 194]. Additionally, TRDs typically add ten times more material than a Čerenkov detector (more than 0.1 radiation length), thus enhancing gamma conversions and energy losses by radiation of the Drell–Yan electrons. Triggering on rare di–electron events in the high–multiplicity PAX environment is not trivial. A pattern recognition, required to link the electromagnetic signatures to the helicoidal trajectory of the particle, is possible only with massive use of computing power.

It is desirable to match the bending power of the spectrometer to the momenta of the emerging particles. In the forward region, where the angle between the particle path and the beam direction is small, the rigidity increases and it is more difficult to provide the necessary bending power. A solenoid centered on the beam provides the maximum bending at large angles in the laboratory frame. Since there is no transverse force on a particle traveling along a magnet field line and the solenoid field lines are parallel to the beam axis, bending is reduced eventually to zero, as the scattering angle is decreased to zero.

The torus has none of the above drawbacks. It neither disturbs the beams nor the operation of the Čerenkov detector since the generated field is limited to a well defined region with negligible fringe fields. The field lines of a toroid field centered on the beam line are always perpendicular to the paths of particles originating from the axis. Its field intensity increases inversely with radius from the beam, such that larger bending power becomes available at small angles. The drawbacks of the toroid could be a not homogeneous field and the presence of the coil material inside the tracking volume. The first issue simply requires to use a detailed field map for tracking. As a conservative approach, it is planned to exploit the over–constraint kinematics of the physical channels of PAX during Phase–I to test and optimize the spectrometer performance before starting the more challenging measurements of PAX Phase–II. The second issue causes a reduction of the azimuthal acceptance; the loss in acceptance can be minimized by using superconducting technology to save material and by placing the support structures and utility lines of the detector in the blind region of the toroid coils. The approach of PHENIX to use Helmholtz coils together with large field–driving magnet yokes would have an even more severe impact on the azimuthal acceptance [195]. Due to the arguments mentioned above a toroidal field approach has been taken to be more suitable for the PAX program than a solenoid field.

A feasibility study about the possibilty to use the PANDA detector in the collider–mode must necessarily be started on the basis of the arguments discussed above.

Part V
Organization

20 Logistics of the Experiment

20.1 Floor Space

As mentioned in chapter 7, all rings of the HESR complex should be in one plane. It is assumed that a hall for the CSR is provided, similar in space as the COSY hall. The APR is located inside the CSR. Furthermore we assume that PAX is the only user of CSR, allowing for a permanent installation of the PAX detector in one of the straight sections. For the experiment, a total space of about 300 m^2 is required. If the experiment has to be moved in and out, this space has to be enlarged to about 450 m^2.

Concerning the required height of the experimental hall, we assume a beam 3 m above the platform and 5 m above the floor. The upper edge of the detector frames is assumed at 7.5 m above floor, resulting in a maximum height of the crane hook of 10.5 m above the floor. With 1.5 m for the crane structure itself, an inner hall volume for the fixed experiment of about 3600 m^3 and for the movable experiment of about 5400 m^3 is estimated (Tab. 10).

Height of the experimental hall	12 m
Crane hook	10.5 m above floor
Assumed beam height	5 m above floor
Volume of the hall (exp. fixed)	$300\ m^2 \times 12\,m = 3600\ m^3$
Volume of the hall (exp. movable)	$450\ m^2 \times 12\,m = 5400\ m^3$

Table 10: Requirements of the experimental hall for PAX.

In addition laboratory space and a control room attached to the experimental hall are required.

20.2 Radiation Environment

The PAX experiment will operate with long beam lifetimes and thus slow antiproton consumption. Requirements for radiation safety at the target location will not be enhanced with respect to other areas along the HESR.

20.3 Responsibilities and Manpower

Although the APR needs institutional responsibilities, we assume that after demonstration and testing the APR will become part of the FAIR facility and is operated and maintained by the laboratory, i.e. GSI.

20.3.1 Institutional Responsibilities (preliminary list)

- **Antiproton Polarizer Ring**
  Ferrara, Jülich
- **Targets (APR, CSR/HESR)**
  Ferrara, Erlangen, Jülich, Gatchina, Madison
  - Target Magnet
    Ferrara, Gatchina
- **Large–Acceptance Spectrometer**
  - Toroid Magnet
    Ansaldo (Italy)
  - Vertex Detector
    Jülich
  - Electromagnetic Calorimeter
    Frascati, Protvino, Yerevan
  - Drift Chambers
    Gatchina, Dubna
  - Threshold Cherenkov
    Dubna, Gent
- **Forward Spectrometer (optional)**
  Partially recuperated from the HERMES experiment.
  - Particle Identification
    Dubna
- **Data Acquisition and Trigger**
  Dubna, Protvino, Gatchina, Jülich
- **Computing, Technical Software, Simulations**
  Ferrara, Tbilisi, Dubna, Beijing, Hefei

20.3.2 Manpower

The present status of manpower available for the experiment can be inferred from the Collaboration list (see p. 5ff). The list comprises about 170 participants from 13 countries and 35 institutions. Based on inquiries and discussions, we expect a very significant further growth of the collaboration in the next couple of years.

20.4 Schedule

20.4.1 Milestones

#	Date	Milestone
1	12/2006	Technical Design Reports finished; overall design of all PAX components
2	12/2008	Fabrication of APR components finished
3	12/2010	Spin filtering with protons in the APR tested
4	12/2010	Fabrication of detector components finished
5	12/2011	CSR operational with protons at FAIR
6	12/2012	Installation of PAX detector (Phase–I) finished
7	12/2013	Commissioning of PAX detector (Phase–I) with protons/antiprotons done
8	12/2013	Phase–I polarized antiproton facility (CSR & APR) ready for experiments
9	> 2015	Commissioning of HESR in the (Phase–II) double–polarized collider mode

Table 11: Milestones of the PAX experiment.

20.4.2 Timelines

The timelines of the PAX experiment depend on the FAIR schedule, the availability of recuperated equipment, like components of the HERMES experiment, and on manpower and funding. A first scenario is presented in Fig. 30. It is based on the assumption that the Phase–I polarized antiproton facility is available in 2013, ready to accept antiprotons from the new antiproton source.

A central part of PAX is the antiproton polarizer ring (APR) which is required to be operational in 2010 for proton tests. Because of the availability of a polarized proton injector at Jülich, we prefer to set up the APR at COSY for proton tests as soon as possible. Installation and running–in at FAIR is scheduled for 2011/12. Furthermore, we assume that the CSR is fully operational at FAIR in 2011, and that the full CSR antiproton facility including the Phase–I PAX detector is available for proton tests in 2012, including acceleration of polarized beams.

The PAX detector is located permanently in the CSR straight section. It consists of the Large–Angle Spectrometer (LAS) and an optional Forward Spectrometer (FS). The FS is largely based on components recuperated from the HERMES detector. Commissioning of the full Phase–I detector is scheduled for 2013.

Two polarized internal gas targets (PIT) exist which can be utilized after improvements and modifications. PIT–I is the present HERMES target which is available in 2006, after

the double–spin program is terminated. This target has been in operation since 1996. After a suitable upgrade, it can be installed at the APR in 2009 for proton tests. In addition, a development program at INFN Ferrara is conducted in order to study possible improvements by using superconductive sextupole magnets for a higher source intensity. PIT–II is the present ANKE target which will be available only after 2009 or later. It is foreseen for installation into the PAX detector at CSR.

20.5 Cost Estimates

The cost estimate for the fixed energy APR, listed in Table 12, is based on a ring built from permanent magnet material, which is a very economic solution, since there are no power supplies needed. For the same reason, the cost of operation is substantially reduced compared to a ring built from electromagnets.

The cost estimate for the PAX detector is divided into four main cathegories, which are briefly discussed below. The resulting figures, listed in Tab. 13, are based on the 1993 figures of the HERMES TDR [184], and were increased by 30% for inflation.

1. Large–Acceptance Spectrometer: Here the structure of the E835 detector has been assumed with the addition of a toroidal spectrometer magnet, calculated using HERMES figures (Cherenkov and Calorimeter), and the price of the HERMES recoil detector for the tracking part.

2. Forward Spectrometer: Here the cost is extrapolated from the one estimated for the Large–Acceptance Spectrometer, with the additional cost for hadron identification (from HERMES RICH).

3. The polarized target is needed for the fixed–target mode only. Here parts of the HERMES and/or ANKE targets can be recuperated, which should result in a reduction of the order of 40%.

4. Infrastructure: These costs are also based on HERMES figures for platform and support structures, cabling, cooling water lines, gas supply lines and a gas house, cold gases supply lines, electronic trailer with air conditioning etc.

Polarized target (HERMES)	1.0 MEU
Machine (permanent magnet version & vacuum)	6.0 MEU
Electron cooler	1.5 MEU
Injection/beam lines	0.5 MEU
Snake	0.2 MEU
Polarimeter	0.2 MEU
Total	9.4 MEU

Table 12: Cost estimate for the Antiproton Polarizer Ring (APR)

Toroid magnet	3.0 MEU
Polarized target (required only for fixed–target mode)	1.0 MEU
Large–Acceptance Spectrometer (LAS)	12.0 MEU
Forward Spectrometer (FS) (optional)	(5.0) MEU
Infrastructure (cabling, cooling, shielding)	3.0 MEU
Total, without (with) FS	19.0 (24.0) MEU

Table 13: Cost estimate for the PAX detector.

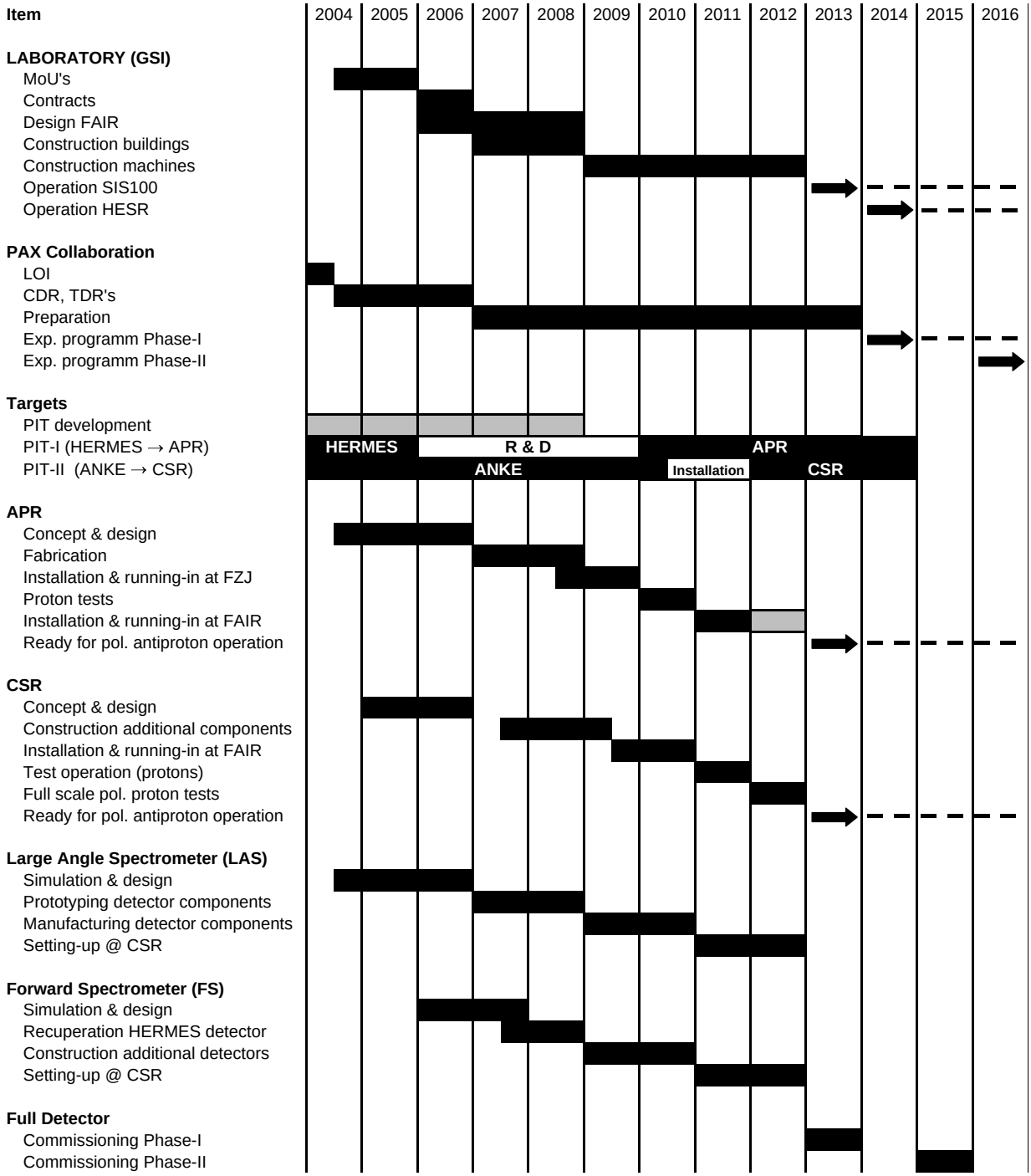

Figure 30: Time Schedule for the PAX experiment.

References

[1] A comprehensive review paper on the transverse spin structure of the proton can be found in: V. Barone, A. Drago and P. Ratcliffe, Phys. Rep. **359** (2002) 1.

[2] M. Anselmino, V. Barone, A. Drago and N.N. Nikolaev, Phys. Lett. **B594** (2004) 97.

[3] A. Efremov, K. Goeke and P. Schweitzer, Eur. Phys. **J.C35** (2004) 207.

[4] D. Sivers, Phys. Rev. **D41** (1990) 83; Phys. Rev. **D43** (1991) 261.

[5] J.C. Collins, Nucl. Phys. **B396** (1993) 161.

[6] HERMES Collaboration, A. Airapetian et al., Phys. Rev. Lett. **84** (2000) 4047; Phys. Rev. Lett. **90** (2003) 092002; Phys. Rev. **D64** (2001) 097101; K. Rith, Progress in Part. and Nucl. Phys. **49** (2002) 245.

[7] A. Airapetian et al., [HERMES Collaboration], Phys. Rev. Lett. **94** (2005) 012002.

[8] J.C. Collins, Phys. Lett. **B536** (2002) 43.

[9] M. K. Jones et al., [Jefferson Lab Hall A Collaboration], Phys. Rev. Lett. **84** (2000) 1398. O. Gayou et al., [Jefferson Lab Hall A Collaboration], Phys. Rev. Lett. **88** (2002) 092301; Phys. Rev. C **64** (2001) 038202.

[10] A. Z. Dubnickova, S. Dubnicka, and M. P. Rekalo, Nuovo. Cim. **A 109** (1966) 241.

[11] S. J. Brodsky, C. E. Carlson, J. R. Hiller and D. S. Hwang, Phys. Rev. D **69** (2004) 054022.

[12] For a discussion on the validity of continuing space–like form factors to the time–like region, see, B. V. Geshkenbein, B. L. Ioffe, and M. A. Shifman, Sov. J. Nucl. Phys. **20** (1975) 66 [Yad. Fiz. **20** (1974) 128].

[13] H.–W. Hammer, U.–G. Meißner and D. Drechsel, Phys. Lett. **B385** (1996) 343; H.–W. Hammer and U.–G. Meißner, arXiv: hep–ph/0312081.

[14] E. Tomasi–Gustafsson and M.P. Rekalo, Phys. Lett. **B504** (2001) 291.

[15] V. Matveev et al., Lett. Nuovo Cimento **7** (1972) 719.

[16] S. Brodsky and G. Farrar, Phys. Rev. Lett. **31** (1973) 1153 and Phys. Rev. **D11** (1973) 1309.

[17] M. Diehl, T. Feldmann, R. Jakob and P. Kroll, Phys. Lett. **B460** (1999) 204.

[18] P. Landshoff, Phys. Rev. **D10** (1974) 1024; P. Landshoff and D. Pritchard, Z. Phys. **C6** (1980) 69.

[19] J.P. Ralston and B. Pire, Phys. Rev. Lett. **61** (1988) 1823; ibid. **49** (1982) 1605; Phys. Lett. **B117** (1982) 233.

[20] G. P. Ramsey and D. W. Sivers, Phys. Rev. **D52** (1995) 116; Phys. Rev. **D47** (1993) 93; Phys. Rev. **D45** (1992) 79.

[21] D. Dutta and H. Gao, arXiv:hep-ph/0411267.

[22] P. Kroll and W. Schweiger, Nucl. Phys. **A503** (1989) 865.

[23] T.A. Amstrong et al., Phys. Lett. **B385** (1996) 479.

[24] K. Krueger et al., Phys. Lett. **B459** (1999) 412.

[25] D.L. Adams et al., Phys. Lett. **B264** (1991) 462; A. Bravar et al., Phys. Rev. Lett. **77** (1996) 2626.

[26] J. Adams *et al.* [STAR Collaboration], Phys. Rev. Lett. **92** (2004) 171801

[27] M. Anselmino, M. Boglione, U. D'Alesio, E. Leader and F. Murgia, Phys. Rev. **D71** (2005) 014002.

[28] W. Vogelsang, "QCD spin physics: Status, and prospects for RHIC," Pramana **63** (2004) 1251 [arXiv:hep-ph/0405069].

[29] V. Barone, T. Calarco and A. Drago, Phys. Rev. **D56** (1997) 527.

[30] O. Martin, A. Schäfer, M. Stratmann and W. Vogelsang, Phys. Rev. **D57** (1998) 3084; Phys. Rev. **D60** (1999) 117502.

[31] A. Bianconi and M. Radici, e-Print Archive: hep-ph/0412368.

[32] M.J. Corden *et al.*, Phys. Lett. **B98** (1981) 220.

[33] E. Anassontzis et al., Phys. Rev. **D38** (1988) 1377.

[34] P.L. McGaughey, J.M. Moss and J.C. Peng, Ann. Rev. Nucl. Part. Sci. **45** (1999) 217.

[35] A. Mukherjee, M. Stratmann and W. Vogelsang, Phys. Rev. D **67** (2003) 114006.

[36] V. Barone, C. Corianò, M. Guzzi and P. Ratcliffe, in preparation.

[37] U. D'Alesio, private communication

[38] M. Anselmino, M. Boglione, U. D'Alesio, E. Leader and F. Murgia, Phys. Rev. **D70** (2004) 074025.

[39] A.V. Efremov and O.V. Teryaev, Phys. Lett. **B150** (1985) 383.

[40] J.W. Qiu and G. Sterman, Phys. Rev. Lett. **67** (1991) 2264.

[41] S.J. Brodsky, D.S. Hwang and I. Schmidt, Phys. Lett. **B530** (2002) 99.

[42] M. Burkardt, Phys. Rev. **D66** (2002) 114005.

[43] N. Hammon, O. Teryaev and A. Schäfer, Phys. Lett. **B390** (1997) 409.

[44] D. Boer, P.J. Mulders and O. Teryaev, Phys. Rev. **D57** (1998) 3057.

[45] D. Boer and P.J. Mulders, Nucl. Phys. **B569** (2000) 505.

[46] D. Boer and J. Qiu, Phys. Rev. **D65** (2002) 034008.

[47] M. Anselmino, U. D'Alesio and F. Murgia, Phys. Rev. **D67** (2003) 074010.

[48] A.V. Efremov, K. Goeke, S. Menzel, A. Metz and P. Schweitzer, hep-ph/0412353.

[49] R. Baldini, S. Dubnicka, P. Gauzzi, S. Pacetti, E. Pasqualucci, and Y. Srivastava, Eur. Phys. J. **C11** (1999) 709; R. Baldini et al., *Proc. of the e^+e^- Physics at Intermediate Energies Conference* ed. Diego Bettoni, eConf **C010430**, T20 (2001) [hep–ph/0106006].

[50] See also R. Calabrese, in *Proc. of the e^+e^- Physics at Intermediate Energies Conference* ed. Diego Bettoni, eConf **C010430**, W07 (2001); H. W. Hammer, *ibid.*, W08 (2001) [arXiv:hep–ph/0105337]; Carl E. Carlson, *ibid.*, W09 (2001) [arXiv:hep–ph/0106290]; M. Karliner, *ibid.*, W10 (2001) [arXiv:hep–ph/0108106].

[51] M. Andreotti et al., Phys. Lett. **B559** (2003) 20.

[52] A. V. Belitsky, X. Ji, and F. Yuan, Phys. Rev. Lett. **91** (2003) 092003.

[53] S. J. Brodsky, J. R. Hiller, D. S. Hwang and V. A. Karmanov, Phys. Rev. D **69** (2004) 076001

[54] F. Iachello, A. D. Jackson, and A. Lande, Phys. Lett. **B43** (1973) 191.

[55] A. Kaidalov, L. Kondratyuk and D. Tchekin, Phys. Atom. Nucl. **63** (2000) 1395.

[56] S. Dubnicka and A.-Z. Dubnichkova, Fizika B **13** (2004) 287 [e–Print Archive: hep-ph/0401081].

[57] R. Bijker and F. Iachello, Phys. Rev. C **69** (2004) 068291; F. Iachello, Eur. Phys. J A **19** (2004) 29, and e–print Archive: nucl-th/031207.

[58] S. Rock, *Proc. of the e^+e^- Physics at Intermediate Energies Conference* ed. Diego Bettoni, eConf **C010430**, W14 (2001) [hep–ex/0106084].

[59] J. P. Ralston and P. Jain, hep–ph/0302043; J. P. Ralston, P. Jain, and R. V. Buniy, AIP Conf. Proc. **549** (2000) 302 [hep–ph/0206074].

[60] G. A. Miller and M. R. Frank, Phys. Rev. **c65** (2002) 065205; M. R. Frank, B. K. Jennings, and G. A. Miller, Phys. Rev. **C54** (1996) 920.

[61] A. Z. Dubnickova, S. Dubnicka, and M. P. Rekalo, Z. Phys. C **70** (1996) 473.

[62] M. Ambrogiani et al., Phys. Rev. **D60** (1999) 032002.

[63] Z. Bai et al., Phys. Rev. Lett. **91** (2003) 022001.

[64] K. Abe et al., Phys. Rev. Lett. **88** (2002) 181803.

[65] K. Abe et al., Phys. Rev. Lett. **89** (2002) 151802.

[66] A. Sibirtsev, J. Haidenbauer, S. Krewald, Ulf-G. Meissner and A.W. Thomas, e–print arXiv: hep-ph/0411386.

[67] T.A.Armstrong et al., Phys. Rev. Lett. **70** (1992) 1212.

[68] E. Tomasi–Gustaffson and M.P. Rekalo, e–print arXive:nucl-th/0307065.

[69] S. J. Brodsky, in Exclusive Processes at High Momentum Transfer, Workshop Proceedings, May 15–18, 2002. Jefferson Lab, Newport News, Virginia, editors A. Radyushkin and P. Stoler, World Scientific, pp. 1–33; S. J. Brodsky and G.P. Lepage, in Advanced Series on Directions in High Energy Physics, v. 5 : Perturbative Quantum Chromodynamics, editor A.H. Mueller, World Scientific (1989), pp. 93–240.

[70] X. D. Ji, Phys. Rev. Lett. **78** (1997) 610. X. D. Ji, Phys. Rev. **D55** (1997) 7114.

[71] A. V. Radyushkin, Phys. Lett. **B380** (1996) 417.

[72] THE QCD STRUCTURE OF THE NUCLEON (*QCD–N'02*): Proceedings. Edited by E. De Sanctis, W.–D. Nowak, M. Contalbrigo, V. Muccifora. Amsterdam, Netherlands, North–Holland, 2002. Nucl. Phys. **A711** (2002).

[73] S. L. Brodsky and J. R. Hiller, Phys. Rev. **C 28** (1983) 475; for a review see C.E. Carlson, J.H. Hiller and R.J. Holt, Annu. Rev. Nucl. Part. Sci. **47** (1997) 395.

[74] A. V. Efremov and A. V. Radyushkin, Phys. Lett. **B94** (1980) 245.

[75] G.P. Lepage and S.J. Brodsky, Phys. Rev. **D22** (1980) 2157.

[76] V. L. Chernyak, A. R. Zhitnitsky and V. G. Serbo, JETP Lett. **26** (1977) 594 [Pisma Zh. Eksp. Teor. Fiz. **26** (1977) 760]; V. L. Chernyak and A. R. Zhitnitsky, Phys. Rept. **112** (1984) 173.

[77] L. Y. Zhu *et al.* [Jefferson Lab Hall A Collaboration], Phys. Rev. Lett. **91** (2003) 022003; H. Gao and L. Zhu, arXiv:nucl-ex/0411014.

[78] P. Rossi *et al.* [CLAS Collaboration], Phys. Rev. Lett. **94** (2005) 012301

[79] M. Mirazita *et al.* [CLAS Collaboration], Phys. Rev. C **70** (2004) 014005

[80] C. G. White *et al.*, Phys. Rev. D **49** (1994) 58.

[81] M. Diehl, T. Feldmann, R. Jakob and P. Kroll, Eur. Phys. J. **C8** (1999) 409.

[82] V. Barone, M. Genovese, N. N. Nikolaev, E. Predazzi and B. G. Zakharov, Z. Phys. **C58** (1993) 541.

[83] J. L. S. Aclander *et al.*, Phys. Rev. C **70** (2004) 015208.

[84] H.A. Neal and H.B.Nielsen, Pys. Lett. B **51** (1974) 79.

[85] B. Z. Kopeliovich and B. G. Zakharov, Z. Phys. C **43** (1989) 241.

[86] G. C. Rossi and G. Veneziano, Nucl. Phys. B **123** (1977) 507; L. Montanet, G. C. Rossi and G. Veneziano, Phys. Rept. **63** (1980) 149.

[87] S.E. Vance, M. Gyulassy and X.N. Wang, Phys. Lett. B (**1998** 45; V. T. Pop, M. Gyulassy, J. Barrette, C. Gale, X. N. Wang and N. Xu, arXiv:nucl-th/0407095; K. Itakura, Y. V. Kovchegov, L. McLerran and D. Teaney, Nucl. Phys. A **730** (2004) 160; A. Capella, Phys. Lett. B **542** (2002) 65;

[88] K. Wijesooriya *et al.* [Jefferson Lab Hall A Collaboration], Phys. Rev. Lett. **86** (2001) 2975.

[89] P. R. Cameron et al., Phys. Rev. **D32** (1985) 3070. G. R. Court et al., Phys. Rev. Lett. **57** (1986) 507. D. G. Crabb et al., Phys. Rev. Lett. **60** (1988) 2351. F. Z. Khiari et al., Phys. Rev. **D39** (1989) 45.

[90] H.A. Neal, J.B. Kuah and H.B. Nielsen, Phys. Lett. B **439** (1998) 407.

[91] J. P. Ralston and B. Pire, Phys. Rev. Lett. **57** (1986) 2330.

[92] J. L. Cortes, B. Pire and J. P. Ralston, Z. Phys. C **55** (1992) 409; J. P. Ralston and B. Pire, AIP Conf. Proc. **223** (1991) 228.

[93] S. J. Brodsky and G. F. de Teramond, Phys. Rev. Lett. **60** (1988) 1924; G. F. de Teramond, R. Espinoza and M. Ortega-Rodriguez, Phys. Rev. D **58** (1998) 034012.

[94] C. Lechanoine–LeLuc and F. Lehar, Rev. Mod. Phys. **65** (1993) 47.

[95] C. Quigg, Nucl. Phys. **B34** (1971) 77.

[96] D. P. Roy, J. Phys. G **30** (2004) R113

[97] A. Mukherjee, I. V. Musatov, H. C. Pauli and A. V. Radyushkin, Phys. Rev. **D67** (2003) 073014.

[98] M. Diehl, T. Feldmann, R. Jakob and P. Kroll, arXiv:hep-ph/0408173.

[99] L. Elouadrhiri, Nucl. Phys. **A711** (2002) 154. S. Stepanyan et al. [CLAS Collaboration], Phys. Rev. Lett. **87** (2001) 182002.

[100] V. A. Korotkov and W. D. Nowak, Eur. Phys. J. **C23** (2002) 455.

[101] M. Diehl, P. Kroll and C. Vogt, Eur. Phys. J. **C26** (2003) 567. M. Diehl, P. Kroll and C. Vogt, Phys. Lett. **B532** (2002) 99.

[102] M. Artuso et al. [CLEO Collaboration], Phys. Rev. **D50** (1994) 5484.

[103] H. Hamasaki et al. [VENUS Collaboration], Phys. Lett. **B407** (1997) 185.

[104] P. Kroll, private communication.

[105] B. Pire and L. Szymanowski, arXiv:hep-ph/0411387.

[106] B. Pire and L. Szymanowski, private communication.

[107] A. Donnachie and P.V. Landshoff, Phys. Lett. **B296** (1992) 227; J. R. Cudell et al., Phys. Rev. **D65** (2002) 074024.

[108] R. Jakob and P. Kroll, Z. Phys. **A344** (1992) 87.

[109] L.N. Bogdanova, O.D. Dalkarov and I.S. Shapiro, Ann. Phys. **84** (1974) 261.

[110] I.S. Shapiro, Phys. Rept. **35** (1978) 129.

[111] G.C. Rossi and G. Veneziano, Phys. Rep. **63** (1980) 153.

[112] C.B. Dover, T. Gutsche and A. Faessler, Phys. Rev. **C43** (1991) 379.

[113] W. Grein, Nucl. Phys. **B131** (1977) 255.

[114] H. Kaseno et al., Phys. Lett. **B61** (1976) 203.

[115] C. Bourrely, J. Soffer and D. Wray, Nucl. Phys. **B77** (1974) 386.

[116] P. Jenni et al., Nucl. Phys. **B94** (1975) 1.

[117] R. Jakob and P. Kroll, Z. Phys. **A344** (1992) 87.

[118] J. Bystricky, F. Lehar, and P. Winternitz, J. Phys. **39** (1978) 1.

[119] D. P. Grosnick et al. [E581/704 Collaboration], Phys. Rev. **D55** (1997) 1159.

[120] A. Gade "The HERMES unpolarized gas feed system, Version 4.0" HERMES internal report (2003).

[121] F. Rathmann et al., Phys. Rev. Lett. **71** (1993) 1379.

[122] E. Klempt, F. Bradamante, A. Martin, and J.–M. Richard, Phys. Rep. **368** (2002) 119.

[123] F. Rathmann et al., Phys. Rev. Lett. **94** (2005) 014801.

[124] H.O. Meyer, Phys. Rev. **E50** (1994) 1485.

[125] C.J. Horowitz and H.O. Meyer, Phys. Rev. Lett. **72** (1994) 3981.

[126] R. Madey *et al.*, *Phys. Rev. Lett.* **91**, 122002 (2003); S. Strauch *et al.*, *Phys. Rev. Lett.* **91**, 052301 (2003); O. Gayou *et al.*, *Phys. Rev. Lett.* **88**, 092301 (2002).

[127] For a list of PAX collaboration meetings, conference presentations, QCD–PAC and STI reports, please visit the PAX web–site at http://www.fz-juelich.de/ikp/pax

[128] ASSIA Letter–of–Intent, spokesperson: R. Bertini, http://www.gsi.de/documents/DOC-2004-Jan-152-1.ps

[129] *Proc. of the Workshop on Polarized Antiprotons*, Bodega Bay, CA, 1985, Eds. A. D. Krisch, A. M. T. Lin, and O. Chamberlain, AIP Conf. Proc. **145** (AIP, New York, 1986).

[130] D.P. Grosnick *et al.*, Nucl. Instrum. Methods **A290** (1990) 269.

[131] H. Spinka *et al.*, *Proc. of the 8th Int. Symp. on Polarization Phenomena in Nuclear Physics*, Bloomington, Indiana, 1994, Eds. E.J. Stephenson and S.E. Vigdor, AIP Conf. Proc. **339** (AIP, Woodbury, NY, 1995), p. 713.

[132] T.O. Niinikoski and R. Rossmanith, Nucl. Instrum. Methods **A255** (1987) 460.

[133] P. Cameron *et al.*, *Proc. of the 15th Int. Spin Physics Symp.*, Upton, New York, 2002, Eds. Y.I. Makdisi, A.U. Luccio, and W.W. MacKay, AIP Conf. Proc. **675** (AIP, Melville, NY, 2003), p. 781.

[134] K. Zapfe et al., Rev. Sci. Instrum. **66** (1995) 28.

[135] K. Zapfe et al., Nucl. Instrum. Methods **A368** (1996) 627.

[136] V. Mull and K. Holinde, Phys. Rev. **C 51**, 2360 (1995).

[137] Preservation of beam polarization is routinely accomplished at COSY–Jülich [196], and at higher energies at the AGS of BNL [157, 158, 159].

[138] Ya. S. Derbenev *et al.*, Part. Accel. **8**, 115 (1978); A. Lehrach and R. Maier, *Proc. of the 2001 Particle Accelerator Conference*, Chicago, Illinois, 2001, Eds. P. Lucas and S. Webber, (IEEE, Piscataway, NJ, 2001), p. 2566.

[139] W. Haeberli, Ann. Rev. Nucl. Sci. **17** (1967) 373.

[140] A. Zelenski *et al.*, Nucl. Instrum. Methods **A**, in press, available from http://www.sciencedirect.com/science/article/B6TJM-4D97J59-3/2/fa659e20fd61ea04fb72e77b82fa99ed.

[141] E. Steffens and W. Haeberli, Rep. Prog. Phys. **66** (2003) 1887.

[142] Particle Data Group, available from http://pdg.lbl.gov/2002.

[143] G.G. Ohlsen and P.W. Keaton, Nucl. Instrum. Methods **109** (1973) 41.

[144] C. Bovet *et al.*, A Selection of Formulae and Data Useful for the Design of A.G. Synchrotrons, CERN/MPS-SI/Int. DL/70/4, 23 April (1970).

[145] J.H. Malmberg *et al.*, *Non–neutral Plasma Physics*, Eds. C.W. Roberson and C.F. Driscoll, (AIP, New York, 1988), p. 28.

[146] J. Grames *et al.*, see p. 1047 of ref [133].

[147] S. Nagaitsev, private communication, EPAC 2004.

[148] P.J. Bryant, AC Division, CERN, CH-1211, Geneva 23.

[149] UGS Gerlinde Schultheis & Partner, Agency for Technology Transfer, Langenbernsdorf, Germany.

[150] Maier R.,Nucl. Inst. and Meth. **A 390** (1997) 1.

[151] Gebel R., private communication.

[152] COSY-SCL Design Update, Internal Report, FZ Jlich, March 2002, edited by H. Jungwirth.

[153] Schwarz V. et al., "EDDA as Internal High-Energy Polarimeter", Proc. International Spin Physics Symposium SPIN 1998, Protvino, (published in World Scientific Singapore (1999)).

[154] V. Derenchuk and A.S. Belov, "Recent Improvements in CIPIOS Intensity and Operation", Proc. of the 9$^{\text{th}}$ International Workshop on Polarized Sources and Targets, 2001, Nashville, IN, USA, eds. V.P. Derenchuk and B. von Przewoski, p. 210 (World Scientific Singapore, 2002).

[155] L. Äystö et al., An International Accelerator Facility for Beams of Ions and Antiprotons, Conceptual Design Report, GSI (2001).

[156] L.H. Thomas, *Phil. Mag.* **3**, 1 (1927); V. Bargman, L. Michel, V.L. Telegdi, *Phys. Rev. Letters* **2** (1959) 43.

[157] F.Z. Khiari et al., Phys. Rev. **D39** (1989) 45.

[158] H. Huang et al., Phys. Rev. Lett. **73** (1994) 2982.

[159] M. Bai et al., Phys. Rev. Lett. **80** (1998) 4673.

[160] see http://www.agsrhichome.bnl.gov/RHIC/Spin.

[161] B.B. Blinov et al., Phys. Rev. Lett. **81** (1998) 2906; B.B. Blinov et al., Phys. Rev. ST Accel. Beams **3** (2000) 104001. V.S. Morozov et al., Phys. Rev. Accel. Beams **4** (2001) 104002. B.B. Blinov et al., Phys. Rev. Lett. **88** (2002) 014801.

[162] For the web–site of the SPIN@COSY collaboration, see http://www.fz-juelich.de/ikp/spin@cosy.

[163] V. S. Morozov et al., Phys. Rev. ST Accel. Beams **7** (2004) 024002; M.A. Leonova et al., Phys. Rev. Lett. **93** (2004) 224801.

[164] A. Piwinski, "Touschek Effect and Intrabeam Scattering", in: A. W. Chao, M. Tigner (eds.), Handbook of Accelerator Physics and Engineering, World Scientific, Singapore, 1999.

[165] C. Baumgarten et al., Nucl. Instrum. Methods **A482** (2002) 606.

[166] R. Engels et al., Rev. Sci. Instr. **74** (2003) 4607.

[167] R.A. Kunne et al. Phys. Lett. **B206** (1988) 557; R.A. Kunne et al. Nucl. Phys. **B323** (1989) 1.

[168] M. G. Albrow et al., Nucl. Phys. **B37** (1972) 349.

[169] R.E. Pollock, Phys. Rev. **E55** (1997) 7606.

[170] A.I Akhiezer and Y.B. Berestetskii, "Quantum Electrdynamics", Monographs and Texts in Physics and Astronomy, Vol. XI, p. 504, ed. R.E. Marshak, Interscience Publishers, 1965.

[171] R. Schleichert et al., IEEE Trans. Nucl. Sci. **50** (2003) 301.

[172] M. Ambrogiani et al., (E835 Collaboration) Phys. Rev. **D60** (1999) 032002.

[173] G. Bardin et al., (PS170 Collaboration), Nucl. Instrum. Methods **A259** (1987) 376.

[174] Aubert et al., (Babar Collaboration), Nucl. Instrum. Methods **A479** (2002) 1.

[175] C. Garabatos et al., Nucl. Instrum. Methods **A412** (1998) 38.

[176] M. D. Mestayer et al., Nucl. Instrum. Methods **A449** (2000) 81.

[177] S. Bagnasco et al., Nucl. Instrum. Methods **A424** (1999) 304.

[178] M. Aizawa et al., Nucl. Instrum. Methods **A499** (2003) 508.

[179] G. Adams et al., Nucl. Instrum. Methods **A465** (2001) 414.

[180] L. Fabbietti et al., Nucl. Instrum. Methods **A502** (2003) 256.

[181] CMS Technical Design Report, CERN/LHCC 97-33, CMS TDR 4 (1997).

[182] ALICE Technical Design Report, CERN/LHCC 99-4, ALICE TDR 2 (1999).

[183] V. A. Batarin et al., Nucl. Instrum. Meth. **A510** (2003) 248.

[184] HERMES Collaboration: Techn. Design Report (1993) DESY-PRC 93/06.

[185] T. A. Armstrong et al. Phys. Lett. **B385** (1996) 479.

[186] T. Rinckel et al., Nucl. Instrum. Methods **A439** (2000) 117.

[187] K. Ackerstaff et al., (HERMES Collaboration) Nucl. Instrum. Methods **A417** (1998) 230.

[188] S. Barsov et al., Nucl. Instrum. Methods **A 462** (2001) 364.

[189] L. Afanasyev et al., Nucl. Instrum. Methods **A491** (2002) 376.

[190] Y. Inoue et al., Eur. Phys. Journ. **C18** (2000) 273 Methods **A734** (2004) 78.

[191] E. Anassontzis et al., Phys. Rev. **D38** (1988) 1377, A. Baldit et al., Phys. Lett. **B 332** (1994) 244, E. A. Hawker et al., Phys. Rev. Lett. **80** (1998) 3715.

[192] M. Artuso et al., PSI-PR-89-05.

[193] T. Akesson et al., Nucl. Instrum. Methods **A 512** (1998) 200.

[194] O. Busch, Nucl. Instrum. Methods **A 525** (2004) 153.

[195] S. H. Aronson et al., Nucl. Instrum. Methods **A 499** (2003) 480.

[196] A. Lehrach *et al.*, see p. 153 of ref [133].